

Study on angle-resolved sensitivity of SOI photodiode with surface plasmon antenna

メタデータ	言語: en 出版者: Shizuoka University 公開日: 2020-11-30 キーワード (Ja): キーワード (En): 作成者: Nagarajan, Anitharaj メールアドレス: 所属:
URL	https://doi.org/10.14945/00027797

Doctor Thesis

Study on angle-resolved sensitivity of SOI
photodiode with surface plasmon antenna

June 2020

Shizuoka University

Graduate School of Science and Technology,

Department of Nanovision Technology

NAGARAJAN ANITHARAJ

Doctor Thesis

Study on angle-resolved sensitivity of SOI
photodiode with surface plasmon antenna

表面プラズモンアンテナ付きフォトダイオードに
おける角度分解受光感度の研究

2020年6月

静岡大学

大学院自然科学系教育部

ナノビジョン工学専攻

ナガラジャン アニタラジ

Abstract

Recently, there has been a trend in the imaging technology to capture the plenoptic information. This is enabled by a so-called plenoptic camera or light field camera, which detects the direction of the incident light as well as its intensity, in contrast to the traditional camera which forms images only by the intensity information. Such kind of advanced camera realizes interesting applications such as three-dimensional (3D) image reconstruction, depth-of-focus extension, lensless imaging, etc. The plenoptic cameras were previously built in the form of the camera array, moving optical component, mirror array, mask-based image sensors, microlens array in front of an image sensor. The existing cameras suffer from large size, complexity in fabrication, long-term stability, high cost, etc. The conventional techniques also have issues in the trade-off between the angular and spatial resolution. To increase the angular resolution, substantial amount pixels need to be employed at the expense of the spatial resolution. Due to these drawbacks, the need for developing angle sensitive pixels (ASPs) emerges.

It has been proposed to make ASP compatible with cost-effective standard complementary metal-oxide-semiconductor (CMOS) fabrication process without the need for process customization, miniaturization of its size makes the camera portable with less cost, it could be arrayed in a plane to detect the incident angle without relying on microlens and could be combined with techniques developed for conventional imaging, it suffers less from the tradeoff between the spatial and angular resolutions and makes the data processing simple by directly capturing the direction of light by each pixel. The conventional ASPs based on Talbot pixels with two diffraction gratings stacked over the photodiode successfully realized the angle sensing for application such as range finding, a polarization filter stacked with quadrature pixel cluster (QPC) to reduce the count of sub-pixels were developed, an angle sensing detector consists of a pair of Si nanowire enabled angle detection with a minimum resolution of 0.32° . However, these existing ASPs suffer from the reduced light sensitivity. The quantum efficiency of Talbot pixel is low in general and could not be increased above 45% even after the structural modification which requires the process customization. Thus, CMOS compatibility, ease of fabrication, high angle resolution, and high quantum efficiency need to be considered in the development of ASP.

The objective of this thesis is firstly to propose a pixel level CMOS photodetector with angle sensing capability and should offer high quantum efficiency. Secondly, mathematical equations to predict the azimuth-elevation peak incident angle of our device is formulated by considering the physical mechanism of angle detection. Then, the predicted peaks in the form

of spatial pattern for azimuth-elevation angular representation are plotted for data analysis. Next, the optimized photodiode is designed based on electromagnetic simulation of 3D finite-difference time-domain (FDTD) method, and absorption efficiency in the same form is evaluated to represent the peaks as spatial pattern. Then, an automated experimental setup to measure the photocurrent of our detector in azimuth-elevation angle is constructed and the spatial pattern is plotted to represent the directivity of our proposed pixel. Finally, effects of the grating type and the grating period, and dependence of polarization angle and the potential of the SOI PD with SP antenna as an ASP are discussed.

We propose the ASP based on silicon-on-insulator (SOI) photodiode (PD) stacked with surface plasmon (SP) antenna of one-dimensional (1D) line and space grating and two-dimensional (2D) hole array grating. When an SP antenna is integrated over the photodiode, sensitivity enhancement occurs. The enhancement has selectivity of wavelength, incident angle and polarization. When the phase matching condition is satisfied, the diffracted light from the antenna couples efficiently with the propagating mode of the SOI layer. The azimuth-elevation incident angle (θ, ϕ) sensitivity of the proposed device is evaluated in this study. Based on the phase matching condition, theoretical prediction for the azimuth and elevation angular detection in pixel level is explained. Experimentally, the SP antenna is patterned over the SOI PD by electron beam lithography. The azimuth-elevation angle dependence of the quantum efficiency of the fabricated device is measured to verify the theoretical and FDTD predictions. Understanding in the incident-angle-dependent characteristics of the proposed PD among theory, simulation and experiment is attained. Due to the ease in fabrication, the compatibility with CMOS integrated circuit technology, the ability to sense both parameters of incident angle, i.e. azimuth and elevation angles, and the high quantum efficiency, present results may open up a new field of ASPs integrated in a image sensor for applications such as 3D image reconstruction, depth-of-focus extension and lensless imaging.

Acknowledgement

First and foremost, I would like to thank God Almighty for strengthening, guiding, giving knowledge, ability and opportunity to undertake this research study and complete it satisfactorily. Without his grace it is difficult for me face the challenges of my life.

I would like to express my sincere gratitude to my supervisor Prof. Hiroshi Inokawa, for providing the opportunity to join his well-established laboratory, continuous effort in supervising, patience, support, and valuable feedbacks in research. I would also like to express my deep gratitude to Assistant Prof. Hiroaki Satoh for guiding me practically, continuous encouragement, feedbacks, and support. The contribution of both of your efforts in reviewing our research and manuscripts is a great support and gives high motivation. I thank both of you sincerely for making my PhD journey more interesting, enjoying and remarkable. I would like to deeply thank my co-supervisor Prof. Aruna Priya Panchanathan, for her supervision, believing me, encouraging to do great things and continuous support.

Besides my mentors, I would like to thank Mr. Shusuke Hara, for his efforts in research by designing, fabricating and measuring the devices. I thank our lab Secretary, Mrs. Akiko Mizoguchi for her kind support. I thank all my lab mates for their kind cooperation. I thank Mr. Shuu Takeuchi for his help and support in installing softwares in my PC.

I thank Hamamatsu Photonics K.K. for providing SOI-CMOS photodiodes. I thank to my Prof. Hiroshi Inokawa, Shizuoka University and Japan Govt. for providing me the MEXT (Ministry of Education, Culture, Sports, Science and Technology) scholarship to pursue my PhD. I would like to deeply thank my host University, SRMIST, India for this opportunity.

I would like to thank my family: my father, Mr. M. Nagarajan, who, although no longer with us, continues to inspire me by his teachings on believing only in making continuous efforts and hard work and not to believe in luck, my mother, Mrs. M. Malarvizhi for her support to step out of my home country and my beloved brother, Mr. N. Vivekananth. I also thank all my friends for their caring and support and my well-wishers for their encouragement.

Hamamatsu, June 2020

Nagarajan Anitharaj

Table of Contents

<i>Abstract</i>	<i>i</i>
<i>Acknowledgement</i>	<i>iv</i>
<i>Chapter 1</i>	<i>1</i>
INTRODUCTION	
1.1 Plenoptic Imaging	3
1.1.1 Plenoptic Function	3
1.1.2 Angle Sensing Imaging	5
1.1.3 Applications of Angle Sensitive Imaging	7
1.2 Plenoptic Camera	8
1.2.1 Conventional Plenoptic Cameras	9
1.2.2 Need for Angle Sensitive Pixel (ASP)	11
1.2.3 Advantages and Limitation of ASP	12
1.3 Review of the State-of-the-Art	
1.3.1 Working principle of microlens	
1.3.2 Working principle of conventional ASP	
1.3.3 Hitachi Lensless Camera	
1.4 Proposed Photodetector	15
1.4.1 SOI PD	15
1.4.2 SP Antenna	16
1.4.3 SOI PD with SP Antenna	20
1.5 Motivation of Proposed Work	21
1.6 Objectives	24
1.7 Synopsis of the book chapters	25
<i>Chapter 2</i>	<i>28</i>

DEVICE STRUCTURE AND FABRICATION PROCESS

2.1	Proposed Device Structure	28
2.2	Types of SP Antenna	30
2.3	Fabrication of SOI PD with SP antenna	31
	2.3.1 Adjustment of Gate Oxide Thickness (t_{GOX})	32
	2.3.2 Formation of Au SP Antenna	33
	2.3.3 Formation of Gate Pad	35
	2.3.4 Device Packaging	38
2.4	Measurement Setup for the Device	39
	Chapter 3	41

THEORETICAL PRINCIPLE OF ANGLE SENSING

3.1	SOI Waveguide Modes	41
3.2	Dispersion Relation for SOI Waveguide	41
3.3	Characteristics of the Device	43
	3.3.1 Wavelength Selectivity	43
	3.3.2 Role as gate electrode	48
	3.3.2 Polarization Selectivity	49
	3.3.3 Material Dependence of SP Antenna	49
	3.3.4 Incident Angle Selectivity	51
3.4	Theoretical Modelling of Peak Angle	56
	3.4.1 Elevation Angular Dependence (θ)	59
	3.4.2 Azimuth-Elevation Angular Sensitivity (θ and ϕ)	60
	3.4.3 Effect of Propagation Modes	64
	3.4.4 Effect of Grating Period	66
3.5	Conclusion	67

	Chapter 4	68
--	------------------	-----------

	SIMULATION AND MEASUREMENT RESULTS	68
--	---	-----------

4.1	Simulation Method and Conditions	68
4.1.1	Introduction of FDTD Method	68
4.1.2	Designing of Device	69
4.1.2.1	Computational Domain	70
4.1.2.2	Boundary Condition	70
4.1.2.3	Spatial Grid	72
4.1.2.4	Incident source	74
4.1.2.5	Temporal Domain Settings	74
4.1.2.6	Material Definition	74
4.1.2.7	Absorption Efficiency	75
4.1.3	Optimization of Device	76
4.1.4	Simulation Conditions for Angle Detection	81
4.2	Measurement Setup	83
4.3	Results of 1D L/S Antenna	86
4.3.1	Elevation (θ) angle dependence	86
4.3.2	Azimuth-Elevation (ϕ and θ) angle dependence	91
4.3.3	Polarization (ϕ_{pol}) angle dependence	95
4.4	Results of 2D hole array antenna	99
4.4.1	Elevation (θ) angle dependence	99
4.4.2	Azimuth-Elevation (ϕ and θ) angle dependence	99
4.4.3	Polarization (ϕ_{pol}) angle dependence	103
4.4.4	Comparison of peak angle and quantum efficiency (1D and 2D SP antenna)	107
4.5	Conclusion	114
	Chapter 5	115

SUMMARY AND CONCLUSION

5.1 Summary	115
5.2 Current Issues	118
5.3 Future Work	119
References	120

Chapter 1

INTRODUCTION

Light plays an important role in our lives while communicating with the world. The world is made of objects and there is no direct communication between the properties of an object and the observer; the space around them is filled with the light radiation patterns, that is captured and interpreted by the human eye. These patterns of light radiations are the representation of the object seen by the observer. Such light patterns could be captured and processed to yield ubiquitous images and videos. Light information plays a vital role in our human visual system and in camera technology[1].

In the research, development and production of camera, a great evolution has been achieved in the way users record, interpret, code, store, distribute, display, and produces images and video. This accelerated the innovation and usage of image and video in various sectors, applications, products, and services providing the consumers more exciting experience. Towards the possibility of these experience, the light patterns that constitute the objects in the world must be acquired and represented according to some format and model[2]. This process is sophisticated by the sensors, transmission and storage devices and displays. Therefore, specific set of functions can be delivered by each component in the system to offer in an efficient, immersive, and less complex war which targets the best consumer experience.

Over the years, the light pattern of the object for the formation of images and video have been traditionally acquired, interpreted, and displayed using a rather simple model corresponding to 2D intensity distribution of the light. In

the recent years, 3D experiences become trending, acknowledging that an efficient and immersive representation of the world requires more than 2D video. Currently, new sensors and display devices have been emerged which exhibits its potential beyond the traditional model and yields a rich collection of light information to provide a better, powerful, and innovative experience, e.g. Light and Lytro cameras and Holographic displays. Lytro camera is the first generation, world's first light-field, pocket-sized camera, which provides a image refocusing after the photo is shoot[3].

But these developments are unconventional leading to revisit the basics of the visual process and focusing the structure of the light information impinging on the observer of a scene, to develop more powerful and complete light representation models. It is natural to consider the plenoptic function in this context, which is the representation of the intensity of light emanating from any point or 3D spatial position, direction, time, and wavelength. The plenoptic function provides a powerful and rich, model of light in which the conventional and new representation models fit depending on the assumed constraints. The emerging camera records the new and denser samplings of the plenoptic function and focuses on providing a richer light representation and thus imply more visual information for addition user capability. The plenoptic imaging requires appropriate representation models associated with efficient optical system. Therefore, an optical image sensor which is thin, small, cost-effective, highly robust with ease of fabrication is required which efficiently completes the plenoptic function. Research in such kind of optical sensors are highly increasing due to the emerging need in the market for the advanced cameras associated with this optical sensor. In addition, the richer representation of the

incident light along with the sensor with above mentioned advantages is challenging for designing efficiently. In the camera with these technologies have started to emerge in the global companies like Hitachi that developed Japan's first lensless camera in 2016 and SONY that produces innovative polarization image sensor[4,5]. Lensless camera records images and videos without utilizing lens. It incorporates a thin film, instead of lens, to capture the light pattern with rich plenoptic function and reconstructs the images through computational algorithm. Lensless camera could be used in IoT as a sensor for collecting data from various places under different conditions. SONY's polarization sensor consists of a polarizer embedded on a photodiode of the image sensor. This sensor used in the industry, such as for inspecting that requires high visibility and sensing. Such kind of pixel scale sensor with some more addition plenoptic function is required in the for the development of a highly functional plenoptic camera. We propose a highly functional pixel scale sensor which collects more richer plenoptic function than the conventional sensor in this thesis.

1.1 Plenoptic Imaging

1.1.1 Plenoptic function

Everything we see in this world is illuminated by light incident from a light source (e.g. LED lamp or sun), passing through space and incident on surface of the objects. At each object, light is partially absorbed, partially reflected to another object, where it bounces once again to finally reach our human eyes. What our eyes picture depends on the precise location of the light field and by moving around that location, a part of the light field can be perceived and used

to obtain the idea of relative location of objects in the world. The beam of light rays passing through any point in space is called as “pencil”.

When a pinhole camera is positioned at a point in space, the image formed is revealed by selecting the pencil of rays at that point. This process of image formation is similar to that happens with a human eye, where the image is formed by the collection of the pencil of light at pupil’s location.

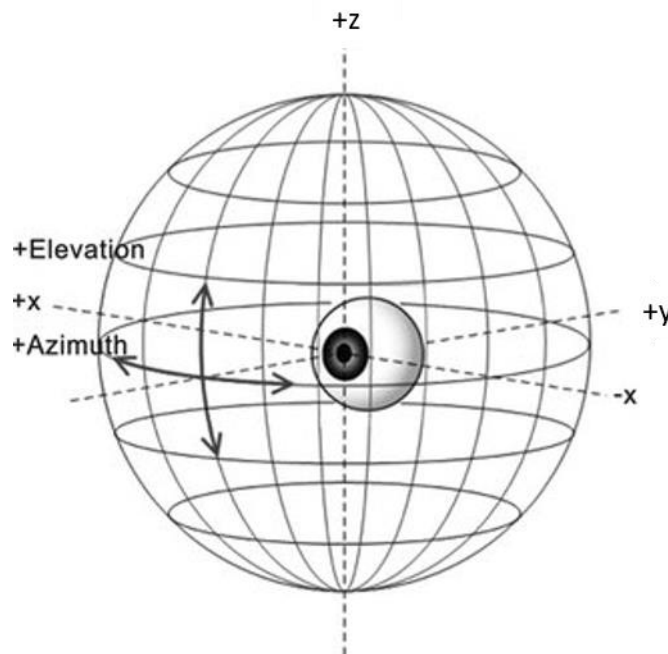


Fig.1.1 Spherical coordinate system representing the azimuth (ϕ) and elevation (θ) angular direction of light impinging from multiple viewpoints in space within the display of pupil view [9].

The light field is the infinite collection of light rays in space, flowing through every location and in every point, i.e. light field represents the incident angle of all the rays at a point. Michael Faraday first proposed the interpretation of light as a field[6]. Andrey Gershun, coined the phrase “light field” by expanding theory of light in 3D space[7]. Each ray is described by the

mathematical function called “plenoptic function (plenus means complete and optic)” in order to quantify them and use them for computation. The plenoptic function covers the complete information communicated to our retina. The distribution of the plenoptic function which involves capturing of the light at different angular directions could be parametrized by the spherical coordinates as, $P(\theta, \phi)$ [1,8]. In Fig.1.1 the schematic of the angle approach which represent the full sphere of light information impinging on multiple points from azimuth (ϕ) and elevation (θ) angle in space is shown[9].

1.1.2 Angle Sensing Imaging

The traditional imaging technique captures the intensity of the light information striking the imaging chips. Imaging based on color filters, detects incident light with different wavelengths. But the new imaging devices which involve capturing the incident angle of light are intensively in research [10–14]. Leonardo da Vinci painted tanks and mechanical calculators even before the first examples were constructed and further another imagination has also been realized by modelling a new camera capable of capturing every light aspect of the scene in front of it. He wrote in his manuscript, that the air is filled infinite number of pencils caused by the objects located in it. The new device involves describing the incident light by the map of angular distribution of light at each location in addition with the intensity. The next generation of the optical wizardry guarantees most-accurate facial-reignition devices, 3D televisions, and imaging devices that provides the user a remarkable indistinguishable window view[1,3]. Fig.1.2 shows the schematic configuration of how the angular information allows extraction of the depth information about the

objects[15]. The in-focus images have high spatial information but consist of less angular information, the out-of-focus images have poor spatial resolution, but possess rich collection of local angular distribution. By recovering the angular distribution of the incident photons which are failed to capture by the traditional cameras, the blurred, out-of-focus objects are recovered[16–25]. The traditional imaging technique captures the intensity of the light information striking the imaging chips. Imaging based on color filters, detects incident light with different wavelengths. But the new imaging devices which involves capturing the incident angle of light is of intensive research. The new device involves describing the incident light by the map of angular distribution of light at each location in addition with the intensity. Fig.1.2 shows the schematic configuration of how the angular information allows extraction of the depth

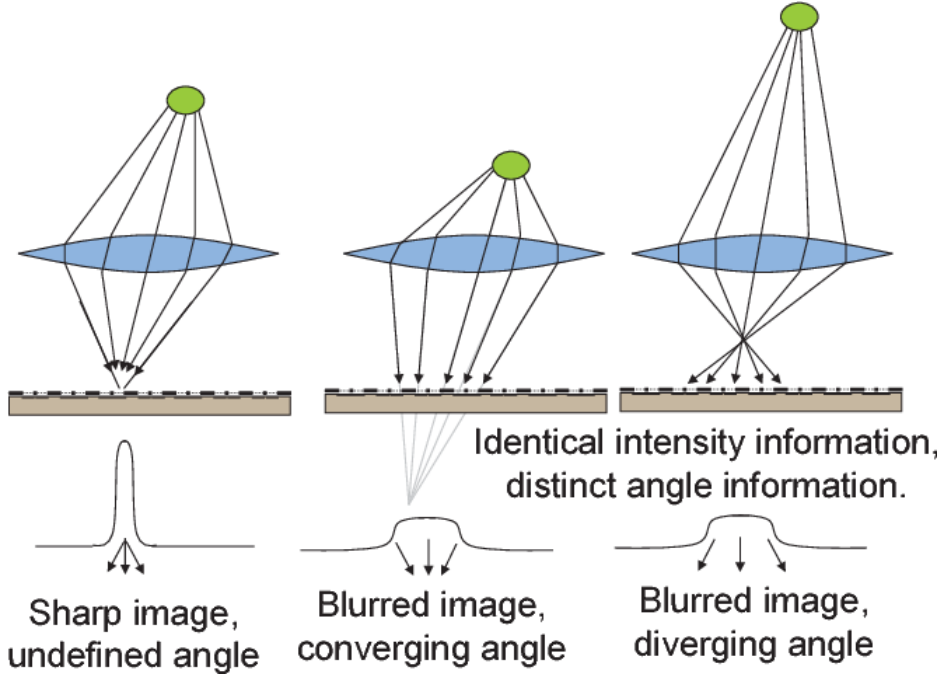


Fig.1.2 Schematic of determination of depth of object by extracting information from incidence angle [15]

images have high spatial information but consist of less angular information, the out-of-focus images have poor spatial resolution, but possess rich collection information about the objects[15]. The in-focus of local angular distribution. By recovering the angular distribution of the incident photons which is failed to capture by the traditional cameras, the blurred, out-of-focus objects are recovered[26–29].

1.1.3 Applications of Angle Sensitive Imaging

The capturing of images at different arrival direction of light allows interesting application in computational imaging such as, image refocusing, 3D imaging, depth mapping, lensless microscopy or lensless imaging, etc.[12,16,34–42,17,24,25,28,30–33]. The angular data from different depths allows the user to shoot a picture and then to refocus the image at any depth during post-capture. Fig.1.3 shows the example of a refocusing of images in

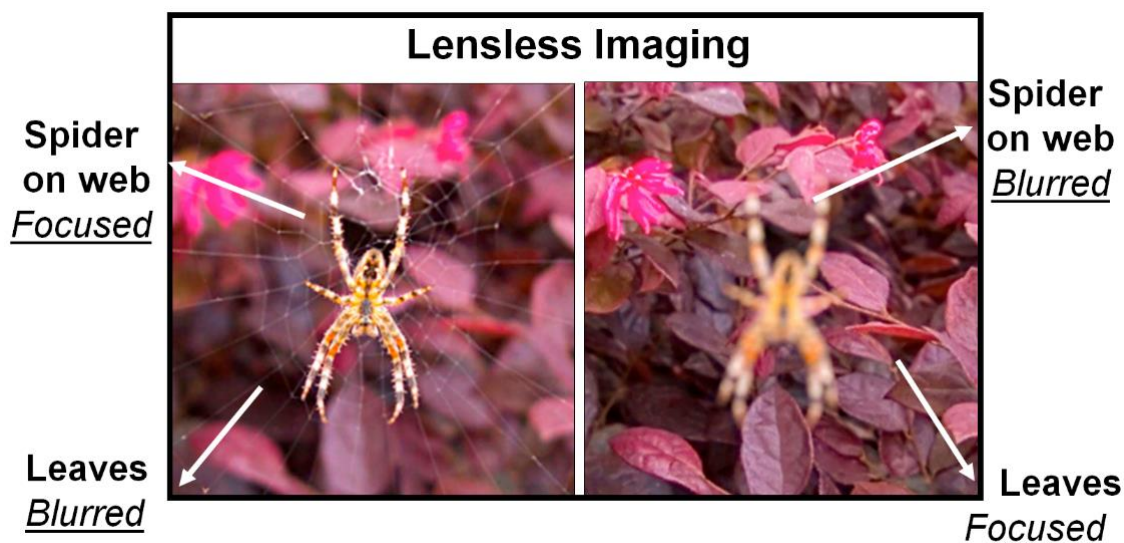


Fig.1.3 Image refocusing after the photo is captured [45].

which the spider is blurred and background leaves are focused in left image whereas the spider is focused sharply and leaves are blurred in the right side image[43]. In the field of Informatics, numerous applications have been developed in computer vision, computer graphics, and security areas. These applications are highly advantageous than the traditional methods. In computer vision, the angle information allows, more accuracy in scene flow estimation for motion analysis, benefitted saliency detection in image boundaries and recognition of material. In computer graphics, angle distribution is significant in rendering, stitching, and segmentation. In security areas, significant role in seeing through occlusion. In the field of medicine and biology, light field cameras are applicable for recording the moving or light-sensitive biological samples in as single shot. In light field microscopy, the lens based eyepiece is replaced by microlens array and image sensor[28].

1.2 Plenoptic camera

Camera is an optical instrument for recording or capturing images. The traditional camera captures the intensity map of a scene and construct the image. Capturing light field information of a scene describes more completely about the scene than a conventional photography and useful in computational imaging for a number of interesting applications. For example, it allows the user to refocus an image to the desired area, after it has been captured, 3D imaging and video processing, depth mapping and LiDAR imaging. The conventional method of capturing the incident of light includes several techniques such as rotating arc of camera, large array of cameras or camera modules and array of pinhole cameras.

1.2.1 Conventional Plenoptic Cameras

i. Moving camera

A simple, easy and straightforward scheme to capture the light field is to utilize a camera in motion along a 2D path to sample the 4D light field. Although this method is convenient to implement, it is only suitable for obtaining static scenes. A simple, easy and straightforward scheme to capture the light field is to utilize a camera in motion along a 2D path to sample the 4D light field. Although this method is convenient to implement, it is only suitable for obtaining static scenes[44-47].

ii. Large camera array

A two-dimensional array of firewire cameras were developed for video processing. MIT also developed a light field camera array to synthesize real-time dynamic DOF effects. These systems suffer from issues based on spatial aliasing. And other limitations are time consuming and requires a lot of effort in engineering[27,46,47].

iii. Pinhole array camera

Researchers have also developed light field camera based on the pinhole array placed between the main camera lens and sensor array in the camera body, to acquire light field at multiple focal planes. The limitations of this system are bulky and reduction in the optical resolution[48,49].

iv. Microlens array

Towards the step for miniaturization leads to the development of arrangement of microlens array in front of the image sensor to capture the

direction of the light rays arriving at the sensor[28,50]. The commercial plenoptic cameras based on this system are Lytro light field camera and Raytrix camera[3,26,51,52].

v. Mask Based Light Field Camera

In this system a patterned planar mask in front of a lens based camera instead of the microlens array is used to discriminate the light arriving from different directions. The mask attenuates the incident light instead of bending, recovering the attenuation enables encoding the ray on the sensor. The limitation of this system is that it suffers from reduction in the light efficiency as the mask partially blocks out the incident light[53].

vi. Mirror Based Light Field Camera

The light field could also be acquired by using a catadioptric mirror array. This system consists of an array of spherical mirrors to capture the incident light field combined with the tele-lens camera. The disadvantage of this systems are the light field samples are nonuniform and suffers from reduction in light efficiency[54,55].

Several techniques have been developed for light field acquiring, but still more sophistication for the camera construction is required as all these techniques involve parallel or moveable optical components for light recording.

Based on the technique employed, the recorded image data typically consists of an image which contains many sub-images, in the case of a microlens array and in the case of multiple cameras, image data consists of many images. The most common feature of both the cases is the all the sub-

images or all the individual images vary slightly from each other because they captured light field from slightly different locations in space (Fig. 1.4a).

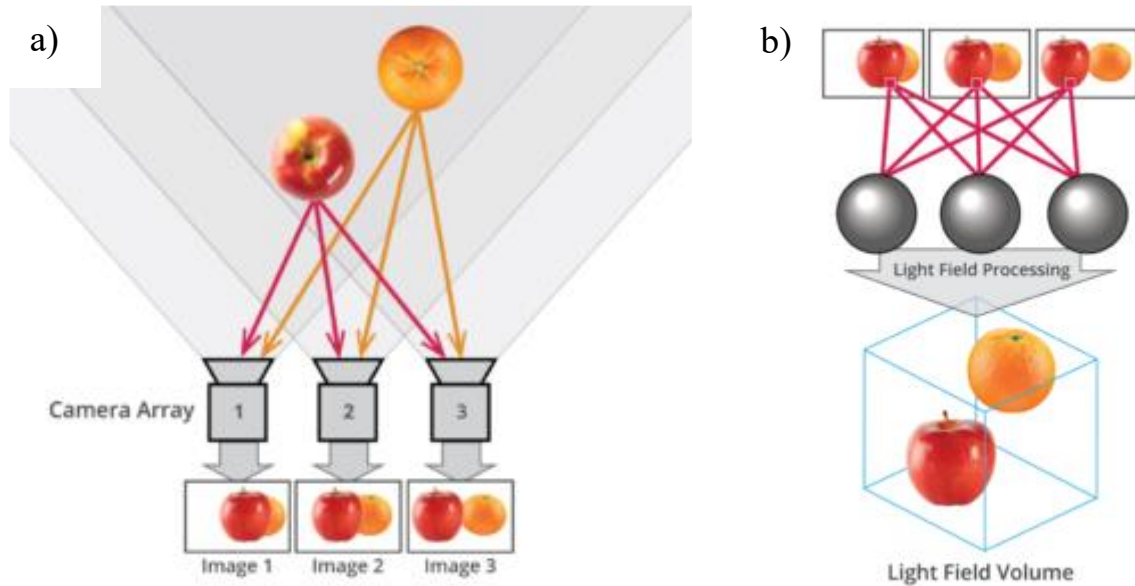


Fig.1.4 a) Images obtained at different incident angles slightly differs from each other and b) reconstructed 3D model of the recorded scene from the different recorded images [83].

The difference between pixels in the sub-images or images is used for computation of the angular information of the captured light field, making it possible to find out each object's position in space and its depth from the camera or lens. This information is further processed using a computation algorithm to construct a light field volume, which represents the 3D model of the scene (Fig. 1.4b). The pictorial representation of the history of the light field camera is shown in Fig.1.5.

1.2.2 Need for Angle Sensitive Pixel (ASP)

These light field cameras demands a high computing power, challenges arises on resolution and affects the image quality, need to be simplified by avoiding the movement of optics and reducing the size, and forcing the camera manufacturers to reconsider the modelling. And the strong coupling between the spatial resolution and angular resolution in the previous techniques, i.e., the sacrificing of spatial resolution for angular resolution is one of the major issues[56]. The state-of-the-art in the light field acquiring shifted to angle sensitive pixels (ASP). An angle-sensitive pixel (ASP) is a CMOS light sensor which is sensitive to the incident angle of the light and having several advantages such as monolithic, does not need multiple lens or moving optics and easy to fabricate by the lithography method makes it attracting for the researchers to further development of this device. And the relaxation in the trade off between the spatial information and angular resolution makes it more interesting for researchers. Without using lens, images could be generated by computational algorithm[30–32,57,58]. When utilized along with a lens in a camera, the angular data allows for formation of 3D imaging from a single image sensor. The Talbot pixel composed of a photodiode under two layers of diffraction grating with the shift in the alignment with the other were successfully developed as an ASP and applied to the applications such as post-capture, image refocusing, range findings, etc. A tiny polarization filter was utilized with the quadrature pixel cluster (QPC) to reduce the usage of sub-pixels which lies under the main pixel [21,23,41,59–62]. Another approach of biologically inspired structure consists of a pair of silicon nanowires were successfully applied as an ASP and yields angular sensitivity as small as 0.32° [63].

1.2.3 Advantages and Limitation of ASP

Advantages

- i. **Manufacture:** The manufacturing of the system like microlens array in front of image sensor requires specialized fabrication process and increases the camera cost. But ASP could be fabricated by cost-effective CMOS fabrication process and requires no post processing.
- ii. **Portable:** The existing conventional models such as camera arrays, moving camera, mask based, mirror-based cameras and micro lens array with image sensor, were bulk in size and complex for construction. The miniaturization of the ASP makes the camera portable with less cost.
- iii. **Programmable:** The ASP could be arrayed in a plane without any microlens and could be combined with any techniques developed for conventional imaging.
- iv. **Scalable:** The conventional techniques suffer from the trading of spatial resolution for angular resolution. In microlens array, the spatial resolution can be increased by employing multiple number of pixels but the angular resolution is reduced. To increase the angular resolution, substantial amount pixels should be employed but the spatial resolution is reduced. ASP does not suffer from such trade off.
- v. **Simple processing:** The conventional light field techniques involves data processing from number of image samples. It consumes a lot of time and effort in image processing. ASP makes the data processing simple by directly capturing the direction of light by each pixel and process quickly the depth estimation or image refocusing.

Limitations

Because of shadow casting, low photographic resolution was obtained and utilization of grating with multiple layer with precise alignment is required. The other limitation of this ASP is the detection of 1D angular information i.e. only θ . It could not discriminate which side of normal the incident light is captured, and angle of arrival could be detected within a short range of 10 degrees.

The main issue to be addressed in the current ASP is the light absorption efficiency. In the Talbot pixel technique, a light efficiency of 12 % is only absorbed and the improvement of 45% in the post processing is still not enough. Therefore, development of ASP with high quantum efficiency, angular resolution and manufacturability is required[21].

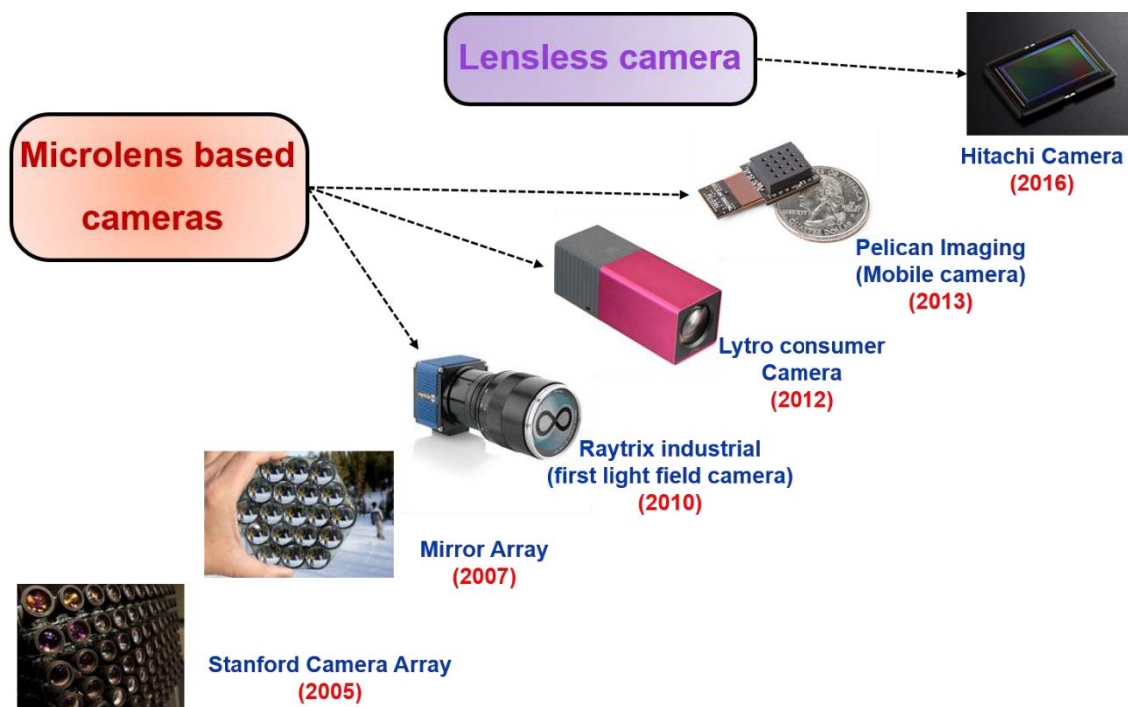


Fig.1.5 History of light field camera

1.3 Review of the State-of-the-Art

1.3.1 Working Principle of Microlens

The plenoptic camera based on microlens, consists of two sets of lenses to form image onto a sensor[3,54]. The first lens is the main lens which is similar to the traditional camera. The second lens is the array of microlens placed at the focal plane of the main lens. Each microlens consists of set of sub-pixels underneath it. The spatial resolution is determined by the number of microlenses and the angular resolution is determined by the sub-pixels underneath each microlens. Fig.1 shows the schematic of the microlens.

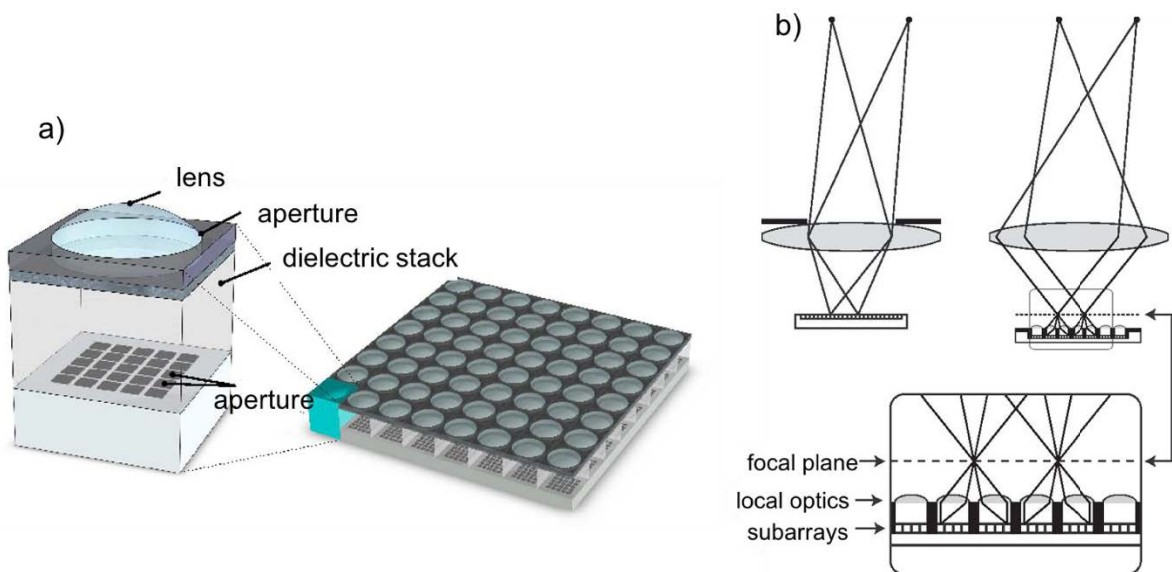


Fig.1.6 Microlens array in a multiaperture image sensor[3,54]

The object of interest is focused onto the microlens plane which sorts the light rays onto the sub-pixels. Each sub-pixel records light from main lens passing through its parent microlens. Sub-images from each sub-pixels underneath each microlens is integrated for image reconstruction.

1.3.2 Working Principle of Conventional ASP

ASP consists of a photodiode stacked with two diffraction grating layers (Fig. 1.7 a))[17]. When the light is incident over the top diffraction grating, a periodic arrangement of interference pattern is generated which is known as Talbot effect. Talbot effect is a optical phenomenon that produces self-image of the periodic grating at a certain depth called Talbot depth. This Talbot pattern laterally shifts as the incident light is tilted which is depicted in the Fig. 1.7 b) and c). The diffraction grating layer placed underneath it is called as analyzer grating which blocks or pass the light based on its arrangement. When aligned exactly below the first diffraction grating it blocks the light and passes the light when shifted from its position. The output of this ASP exhibits a sinusoidal periodic wave as a function of incident angle (Fig. 1.7 d)).

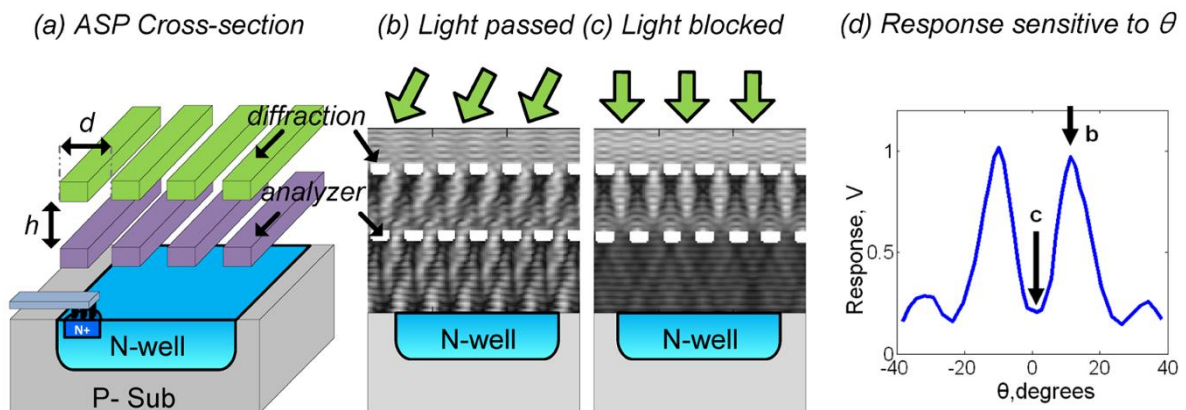


Fig.1.7 ASP based on Talbot pixel a) schematic of the device b) and c) Talbot pattern for different incident angle by the two diffraction grating layer and d) output response of the ASP as a function of incident angle

single incident angle and Fig. 1.8b) shows the output of the bare photodiode which clearly shows that the signal is not responsive to incident angle and shows

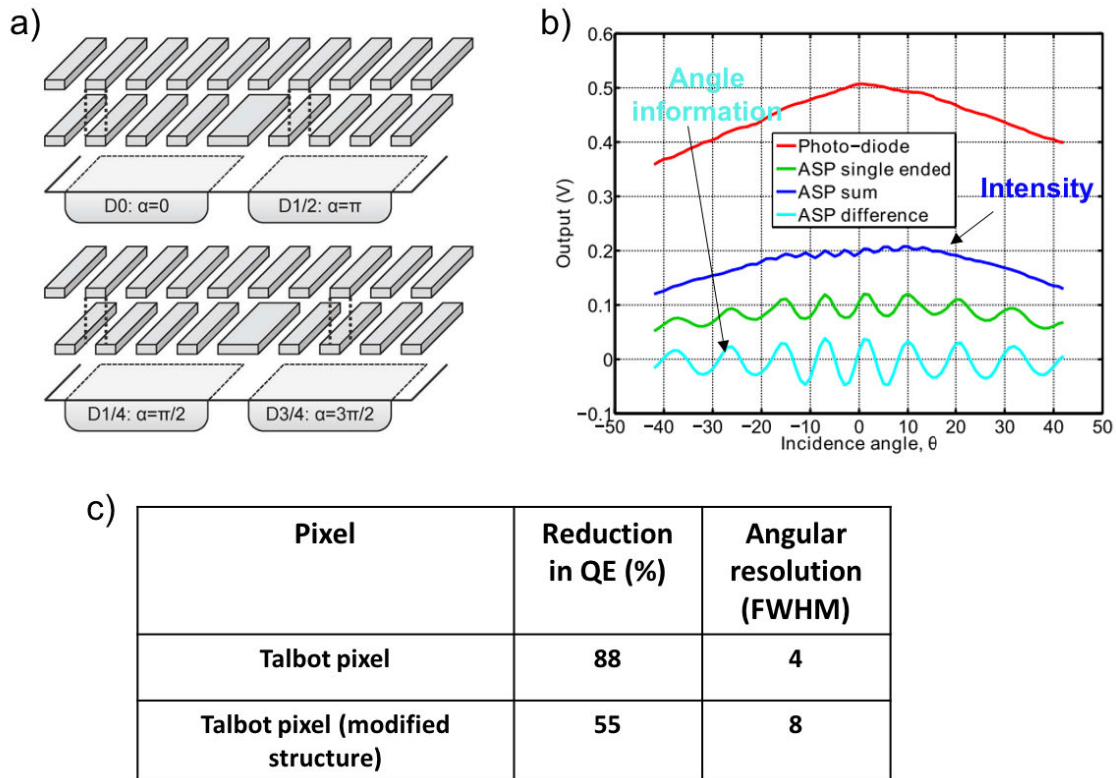


Fig.1.8 a) different arrangement of analyzer grating b) output response of bare photodiode and ASP and c) table for QE and angular resolution for different Talbot pixels [17]

a wide peak. An ASP (green colour) provides a sinusoidal signal which is decaying as the incident angle increases. When a complementary pair of ASP is summed or subtracted, intensity (dark blue line) information could be retrieved or angular information (light blue line) could be obtained, respectively. Fig. 1.8c shows a table by comparing different Talbot pixels. The conventional Talbot pixel suffers from reduction of light efficiency by 88% due to the light blocking by the two diffraction layers. To improve the light efficiency, modification in the structure of ASP was done by post CMOS

process and light reduction was reduced to 55%. But while comparing the angular resolution, it increased to 8° from 4°.

1.3.3 Hitachi Lensless Camera

Hitachi developed the Japan’s first lensless camera in 2016 on based on principle of Moire fringes and performs the function for image refocusing and features, thin, light weight camera without lens (Fig. 1.9)[4]. The two important features of the developed camera technology are described as,

Thin permeable concentric circles are printed in front of the image sensor. During image processing, another concentric circle pattern is superimposed on the shadow and More fringes with spacing dependent on the incident angle of a light beam are produced. The image processing method called, Fourier transform is used to reconstruct the image.

The image refocusing could be realized by incorporating concentric

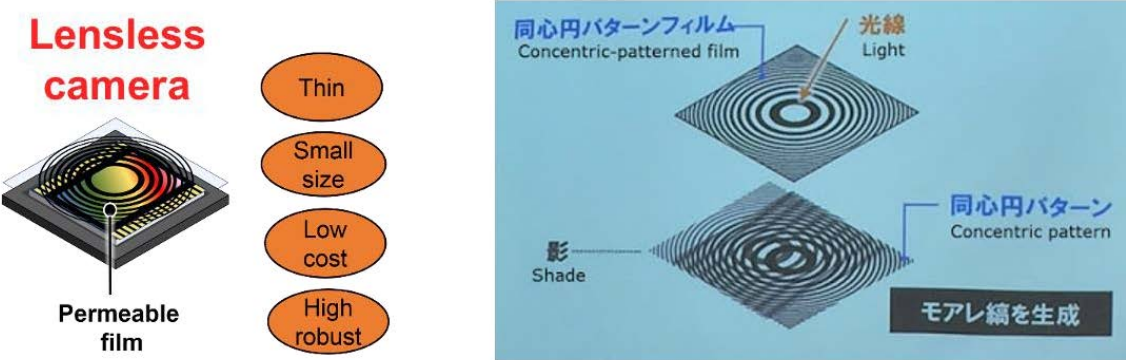


Fig.1.9 Hitachi’s lensless camera [4]

circle with different size. The focus could be changed by the size of the circle pattern superimposed on the shadow. The focal position could be adjusted freely by superposing the pattern by image processing after image capturing.

Devices	Advantage	Limitations
<ul style="list-style-type: none"> ❖ Pinhole array camera ❖ Moving camera ❖ Large camera arrays ❖ Mask based camera ❖ Mirror array camera 	Captures azimuth and elevation (φ, θ) angle of light	<ul style="list-style-type: none"> ➤ Complex construction ➤ Bulk in size and costs high
Microlens array	<ul style="list-style-type: none"> ➤ CMOS compatible ➤ Miniaturized thickness <1mm (often ~10μm) 	Aligning microlens array in front of image sensor is difficult
Angle sensitive pixel (ASP)	<ul style="list-style-type: none"> ➤ Image with or without lens is possible. ➤ CMOS compatible 	<ol style="list-style-type: none"> 1. Suffers from reduction in QE 2. No. of pixels per angle is large (4 ASPs) 3. Trade-off b/w angle sensitivity and detectable angle range

Fig.1.10 Device Scaling of light field camera

1.4 Proposed Photodetector

1.4.1 SOI PD

The cameras based on charge coupled devices are replaced by the highly potential CMOS image sensors. Image sensors built on CMOS chips would be an inevitable optical component for the highly advanced intelligent systems in future and are intensively researched due to their enormous requirement for the commercialization. The development of image sensors field focuses on investigating and developing image sensors on CMOS chips based on the silicon-on-insulator (SOI) technology. Through this technology, electronic devices can be built on a thin silicon and can be isolated electrically from the thick semiconductor substrate by utilizing a buried insulating layer. The other advantages are its high-speed operation and reduced parasitic capacitances

which results in large voltage gain per electric charge. Thus, SOI technology is considered to be the most promising technology for enhancing the performance of CMOS devices especially for integrated circuits for servers and gaming applications. For the application to image sensors, photodetectors are fabricated over the SOI layer. The thin absorption layer offers a faster response but results in the light sensitivity of the photodetector low due to its thin size. To overcome this trade-off an optical near-field is utilized to efficiently absorb the light in the thin absorber layer. SP antenna is employed in the SOI PD to generate the optical-near field[64–66]. A brief introduction on the optical property of SP antenna is given in the next section. The optical property of SP antenna is discussed in the next section.

1.4.2 SP Antenna

A surface plasmon polariton (SPP) is an electromagnetic wave that propagate along the interface of a metal and a dielectric, practically in the visible or infrared wavelength region. The surface plasmon polariton involves the surface plasmons in metal as charge density wave and polariton as electromagnetic waves in the dielectric. SPPs are optical surface waves, guided along the metal-dielectric interface in a similar way that light guided by an optical fiber. The wavelength of this surface waves is shorter than the incident photons. Thus, SPPs have spatial confinement more tightly and with a large local electric field intensity. In the perpendicular direction to the interface, SPPs have subwavelength-scale confinement. The propagation of SPP along the interface occurs until the energy is vanished either to absorption in the metal or scattering into the free space.

Surface plasmon based photodetectors are of intensive current research. Such photodetectors combine a metallic structure that support surface plasmonic effect with a photodetection structure which operates based on internal electron-hole pair creation. The architecture of the photodetectors is highly distinct, involving surface plasmons on metallic gratings, on planar metal waveguides, on nano-antenna, island, or particles, plasmon-assisted transmission through a single or sub-wavelength metallic hole array. The inherent properties of surface plasmons, such as subwavelength confinement and resonance on metal structures could be exploited to achieve interesting characteristics such as high-speed detection with low-noise, single-plasmonic sensing, photovoltaic applications, biosensing and imaging[49].

Metal-dielectric interface

The SPPs propagation is supported by a simple structure consists of optically semi-infinite dielectric and an optically semi-infinite metal along its interface. To implement the SPP supporting structures, good dielectric materials and highly conductive metals are required. Silver is the preferred materials as it possesses low optical loss than the other noble metals over a wide wavelength range. But practically, gold is chosen for fabrication as silver is more reactive due to the oxidation when exposed to air, i.e. gold has a good optical performance and high chemical stability. The metal should satisfy $\epsilon_R \gg \epsilon_I$ to support SPPs. At optical wavelengths, metals are dispersive. The Drude model for the permittivity predicts the dispersive character of metals, way from interband transitions,

$$\varepsilon_{r,m} = -\varepsilon_R - j\varepsilon_1 = 1 - \frac{\omega_p^2}{\omega^2 + 1/\tau^2} - j \frac{\omega_p^2/\tau}{\omega(\omega^2 + 1/\tau^2)} \quad (1)$$

where, ω_p is plasma frequency, and

τ is relaxation time.

This equation holds the ‘‘Drude region’’ corresponds to that part of the electromagnetic spectrum, when applied to find the measured relative permittivity of metals. For most of the metals, Drude region spans the wavelength from visible to infra-red range. When wavelength approaches infra-red and beyond it, the metal becomes a perfect electric conductor. The single-interface allows the propagation of one non-radiative (purely bound), transverse magnetic (TM) mode at any angle in the positive z-direction (x-z plane). The electric fields, E_y and E_z and magnetic fields, H_x represents the SPP fields are confined along the y-direction and peaks at the interface and decays into both the media exponentially. The SPP is confined at the interface as the $\text{Re}\{\varepsilon_r\}$ of metal and dielectric have opposite sign at the operating wavelength. The depth of field penetration in metal is much smaller than the dielectric.

For the single-interface SPP, the wavenumber is given as,

$$k_{SPP} = k_0 \left(\frac{\varepsilon_{r,m}\varepsilon_{r,d}}{\varepsilon_{r,m} + \varepsilon_{r,d}} \right)^{1/2} \quad (2)$$

The dielectric medium with lossless dielectric constant ($\text{Im}\{\varepsilon_{r,d}\} = 0$), the above simplifies to the following approximation for real and imaginary parts as follows,

$$k'_{SPP} \cong k_0 \left(\frac{\epsilon_R \epsilon_{r,d}}{\epsilon_R - \epsilon_{r,d}} \right)^{1/2} \quad (3)$$

and

$$k''_{SPP} \cong k_0 \frac{\epsilon_1}{2\epsilon_R^2} \left(\frac{\epsilon_R \epsilon_{r,d}}{\epsilon_R - \epsilon_{r,d}} \right)^{3/2} \quad (4)$$

As the wavelength increases, the metal approaches as a perfect electric conductor (PEC), the SPP confinement decreases and the dispersion curve moves along with the light line (an interface between the PEC and a dielectric does not support SPPs). As the wavelength decreases, SPP approach energy asymptote where the wavevector becomes large. The optical density-of-states increases and the group velocity decreases in the asymptote. The SPP links the non-radiative for frequency greater than the asymptote. The SPP could not be directly excited by the incident light. Therefore, by using an additional structure such as prism or rough surfaced or corrugated grating is commonly used to match the momentum of the incident light with that of the SPP[68].

After the Ebbesen's discovery, extraordinary light transmission through the subwavelength aperture system in a metallic layer has attracted great interest. According to the theoretical and experimental studies it is shown that the SPs play the main role in confining light in the sub-wavelength aperture[69–71]. This concept is demonstrated in earlier researches by utilizing SP antenna to enhance the optical near-field on photodiode with small active area of silicon (Si) mesa structure[72]. When light is incident on the surface of the SP antenna, the incident light excites the SPs along the surface and resonance occurs along

the periodically arranged metallic surface. This excited SPs which is in resonance with the incident light enhance the optical near-field on the aperture. The enhanced optical near-field generates the carriers within the Si mesa structure. We have proposed and developed a device by fabricating surface plasmon (SP) antenna on top of the SOI PD to enhance the light sensitivity efficiently.

1.4.3 SOI PD with SP Antenna

In this thesis our novel device composed of pn junction photodiode (PD) inscribed over the thin silicon layer with an underlying buried oxide layer (BOX) supported by the silicon substrate and the SP antenna is mounted as the top layer over the PD is investigated for the application of angle selective image sensing. We initially propose and mounted a SP antenna over the conventional SOI PD as a solution for enhancing the light absorption in the photodiode. SP antenna is composed of periodically arranged metallic structures such as Ag, Al and Au. It has the property of enhancing the optical-near field around it, when light is incident on the surface of SP antenna. The contribution of this property plays a supplementary role in enhancing the light absorption in photodetector. The main contribution of SP antenna is to efficiently couple the incident light with the propagating light in the SOI layer. The enhancement in the optical-near field denotes the increase in the diffraction efficiency around the antenna surface. The SOI PD is similar to the structure of the SOI waveguide, thus consists of propagation modes in SOI layer. The enhancement of the light occurs due to the strong coupling of the diffracted light from the SP antenna with the propagation mode in the SP antenna. Our previous research on SOI PD

with SP antenna of metallic line and space (L/S) grating demonstrate that quantum efficiency is enhanced by the incorporation of SP antenna by 37% for 100 nm SOI thickness at the wavelength of 550 nm. In addition to the light enhancement by coupling effects, the SP antenna has several characteristics such as wavelength tuning. The SP antenna couples the incident light with wavelength selective nature to the SOI PD by fabricating devices with different grating period. We have also investigated the material property of SP antenna by varying the metals such as Au, Ag and Al. The investigation clearly shows that there is no influence of the material for enhancement. Any material can enhance the light because the peak quantum efficiency appeared only due to the coupling effect of antenna in which the the peak wavelength is highly tuned by the grating period[65,73,74]. The incident angle selective nature of the device has also been demonstrated for SOI PD with L/S SP antenna but the investigation is done only for the elevation angle[75]. The new feature of the SP antenna, azimuth-elevation incident angle sensing is focused in our current research. We reported the angular selective behaviour of the SOI PD with 1D L/S SP antenna by representing the azimuth-elevation angular distribution of the light absorption efficiency and explained its potential application for the image sensor application as an efficient ASP[76]. We proposed one more type of SP antenna in our current research, 2D hole array grating and investigated its angular distribution.

1.5 Motivation

The motivation of our proposal arises from the thought that constructing a camera that captures the incident angle using an array of tiny pixels. As

explained above, an ordinary traditional camera captures only the intensity of incident photons striking their image sensor chip. Capturing wavelength of the light provides second set of data, making the camera to produce color photographs. The new devices in the market have started to capture the third set of data: angle of light. This allows the camera to focus beyond a single plane for measuring image samples at different depths of a scene at a single capture. The image sensors that capture both the intensity and incident angle will allow the user to refocus the already-snapped photographs, lensless imaging, and the 3D image formation with a single camera is of recent trend in the field of image sensors.

The detection of the angle of light, however, is complex as it requires multiple optical components which leads to high cost, long processing time and also bulk in size. Steps towards miniaturization also leads to a complex system as it consists of multiple microlens. The commercial cameras have shifted from using CCD to CMOS based image sensors[77–79]. The CMOS based pixel scale image sensor which can be operated even without any lens is striving the research field of image sensor. The currently developed pixels for the detection of angle called angle sensitive pixels (ASPs) suffers from low light resolution and limited by the angular range of around 10° . It is also impossible to predict that light is arriving at left or right side of the normal of these ASP. To overcome these limitations, a CMOS based pixel scale tiny detector with rich collection of incident angle and high light absorption efficiency is required.

Our research group have been progressively researching the new features of the CMOS photodetector based on SOI technology. SOI, a unique material

consists of a thin silicon layer supported by the silicon substrate with a layer of silicon dioxide sandwiched in between them. Due to its advantages like low-parasitic capacitance, complete electrical isolation from devices and high-speed performance it is widely used in large-scale integrated circuits (LSIs). In addition to these characteristics, SOI possesses several interesting characteristics to photodetectors such as light confinement for enhanced light sensitivity, carrier confinement for sensitive photogenerated carrier detection and thermal isolation for the detection in wider wavelength range as a bolometer. The thin silicon layer offers a high performance of the device but suffers from low light absorption. To overcome this trade off we applied surface plasmon (SP) antenna over the silicon layer with an isolation layer of thin silicon dioxide as a solution. We have achieved the light enhancement after the incorporation of the antenna without reducing the size of the photodetector. We further motivated to study the new feature of this novel device, SOI PD with SP antenna. We thoroughly investigated the role of antenna in enhancing the light by varying the grating period of antenna and changing the material of the antenna under different polarization and incident angle conditions of incident light. We theoretically, numerically and experimentally demonstrated the light enhancement under different conditions to show that it happens due to the coupling effect between the diffracted light from the antenna and waveguide mode in the SOI PD. In this investigation the incident angle selective behaviour of the device motivated us more intensively to consider its potential role as an ASP which is striving the research field of image sensor. By having in mind the conventional ASPs's limitations such as the detection of elevation angle alone and that too within small angular range and less light resolution, we have developed a highly

advanced and functional ASP which in near future would be developed as a promising light field camera to overcome the current limitations of the conventional ASP.

1.6 Objectives

The scope of the thesis is to advance the state-of-the-art in plenoptic imaging by proposing devices for capturing the incident angle of light. The main objectives are:

- i. To characterize the SOI PD with SP antenna as an ASP.
- ii. Formalizing a mathematical equation for predicting the 2D peak incident angle of our device by considering the physical mechanism of angle detection. Plotting the predicted peaks in the form of spatial pattern for 2D angular representation of the devices.
- iii. Evaluating the absorption efficiency of the pixel scale devices for azimuth-elevation angle detection using the electromagnetic simulation software, 3D Finite-difference time-domain method for numerical prediction of 2D angular detection. To represent the numerically predicted peaks as spatial pattern.
- iv. Constructing an automatic experimental setup to measure the photocurrent of our detector in full azimuth-elevation angle and plotting the spatial pattern to represent the directivity of our proposed pixel.
- v. Understanding the difference among theoretical, simulated and experimental results in 2D plane.

1.10 Synopsis of Book Chapters

In **Chapter 1**, the fundamentals of the light field or plenoptic imaging with interesting applications are discussed briefly. The need for light field camera with angle sensitive pixels, ASP was explained by discussing the existing light field cameras and its limitations. The introduction of our novel device, SOI photodetector based on the CMOS technology is discussed with the current status of the research. The motivation, objective and synopsis of the book chapter is provided.

In **Chapter 2**, our novel device SOI PD with two types of grating, 1D L/S grating and 2D hole array grating SP antenna is proposed. The working principle of the device and the spectroscopic characteristics with wavelength, polarization and incidence angle selectivity is overviewed. The new feature of 2D incident angle detection is focused and discussed using theoretical estimation. A framework of mathematical equation is formalized for the theoretical prediction of the 2D angular distribution. Using Matlab coding spatial pattern for 2D data representation is calculated. Thus the theoretical modelling of the CMOS based pixel scale photodetector is done successfully and discussed in this chapter.

Chapter 3 involves the angle prediction based on the theoretical concept behind the principle of angle detection in the proposed device. The principle of operation of the lateral light wave propagating in the SOI slab along with different waveguide modes is explained well and exhibited graphically using the dispersion relations for symmetrical slab waveguide. The concept of angle detection involves efficient coupling between the diffracted light from the SP

antenna and the SOI waveguide mode. A mathematical equation is formalized based on this concept which relates the incident angle of the light with wavelength of incident light and propagating mode and the grating period of the antenna. The incident angle data for SOI PD with SP antenna of 1D or 2D hole array grating is represented in polar coordinates in the form of spatial pattern. The spatial pattern for various periods and different waveguide modes is also discussed in this chapter.

In **Chapter 4**, the FDTD simulation and measurement results of the devices are represented. An introduction on the simulation method, 3D Finite-Difference Time-Domain (FDTD) and designing of devices and optimization of device structure is discussed well. The incident light configuration two different analysis is shown, and the evaluation of azimuth-elevation angle dependence was carried out based on that. The results are measured from the experimental set-up and plotted in the form of spatial pattern to simultaneously represent the azimuth and elevation angle dependence. Using the simulation and measurement set-up different investigations are discussed. The spatial pattern for calculated quantum efficiency and theoretical estimation on the effect of grating period of both the type of SP antennas, 1D L/S grating and 2D hole array grating when the polarization of light is rotated along with the azimuth angle of light was represented and discussed with a fair comparison. The azimuth-elevation angle dependence of the fabricated devices of fixed period for 1D and 2D grating was measured by rotating and tilting the device such that the polarization component was rotated along with the azimuth angle. Although, the angles were limited, good reproduction of data was achieved. Further investigation on polarization dependence was investigated for both the devices,

1D and 2D grating. The polarization characteristics of 1D and 2D SP antenna exhibits different from each other. Thus, theoretical estimation, numerical prediction and experimental demonstration of angle dependence is investigated.

In **Chapter 5** the summary of the research is discussed. The theoretical concept of angle sensing, the formulation of mathematical equation for predicting the peak angles, followed by designing and optimizing by FDTD simulation method and evaluation of absorption efficiency in azimuth-elevation angle of the device for predicting the quantum efficiency and finally the experimental demonstration by the specially constructed measurement set-up. The data analysis shows the comparison of the theoretical and FDTD and experimental results for two different incident light configuration and capability of the incident angle detection in our proposed devices. The current issues of this study are identified and mentioned. The future prospect of the research is also proposed.

Chapter 2

DEVICE STRUCTURE AND FABRICATION PROCESS

This chapter involves the proposal of a pixel level CMOS photodetector which has the capability to detect the light with a rich collection of angles of the incident direction. The structure of the SOI PD with SP antenna of 1D L/S grating or 2D hole array grating is formed by different layers[80]. The fabrication process of the proposed structure is described in detail. The experimental setup for the measuring the output photocurrent of the device under various azimuth and elevation angle is also explained in brief.

2.1 Proposed Device Structure

Our current work focuses on proposing a novel device based on CMOS technology to meet the challenges in the research field of light field imaging. Our proposed device consists of pn-junction photodiode (PD) for light detection with an additional structure, surface plasmon (SP) antenna stacked over it. The photodiode is designed and fabricated based on the SOI (silicon-on-insulator) technology which is one of the strategies to extend the Moore's law by allowing continued miniaturization of microelectronic devices. The p-n junction is formed in a layered silicon-insulator-silicon substrate to reduce the parasitic capacitance, thereby providing high performance. The silicon layer in which the photodiode is formed is supported by the insulator, silicon dioxide. This layer is referred to as the buried oxide (BOX) layer. The structure of the conventional SOI PD is shown in Fig. 2.1. Over the gate region of the photodiode is a layer of silicon dioxide which is referred as the gate oxide (GOX). The surface

plasmon antenna is stacked over the photodiode with an electrical isolation formed by the gate oxide. A thin layer of Ti is inserted between the antenna and the gate oxide for adhesion. This isolation allows SP antenna to act as gate electrode and control the depletion layer and increase the photocurrent. Fig.2.2 shows the schematic of the proposed SOI PD with SP antenna.

The surface plasmon antenna is formed by using noble metals such as silver, gold, aluminium and copper as the real part of the permittivity in the

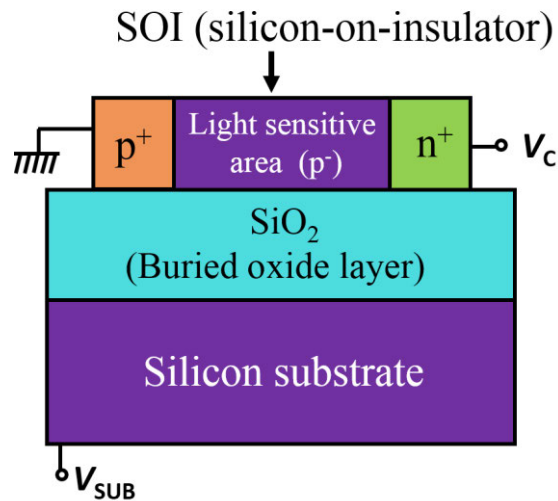


Fig.2. 1 Cross-sectional view of silicon-on-insulator (SOI) photodiode (PD)

visible and infrared wavelength range is negative. Silver is commonly utilized in the devices based on surface plasmonic effect because of its property of exhibiting low optical losses. However, we employ Au due to its durability to surface oxidation during fabrication. It is a well-known fact that when light is incident over the surface plasmon antenna, SPs are excited along the metallic surface. The optical near field is enhanced by the surface plasmonic effect of the antenna. The enhanced light penetrates through the gate oxide layer and

interacts with the silicon photodiode. Since the photodiode is fabricated over the SOI substrate, it is similar to the SOI waveguide and supports the propagation of lateral wave in silicon slab. The enhanced light from the SP surface couples strongly with the propagation light in the SOI waveguide and exhibits high enhancement of light absorption.

2.2 Types of SP Antenna

The surface plasmon antenna consists of periodically arranged metallic structure. In our research we consider two types of SP antenna: 1. 1D line and

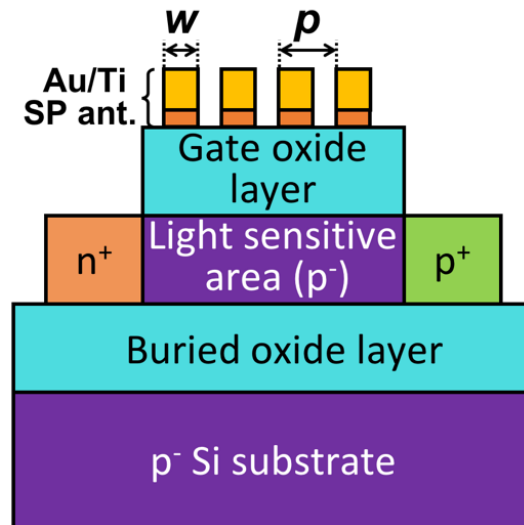


Fig.2. 2 Cross-sectional view of SOI PD stacked with surface plasmon antenna.

space (L/S) grating and 2. 2D hole array grating. As shown in Fig.2.2. the SP antenna consists of a) periodic arrangement of Au lines and space and b) square latticed hole array in Au layer. The main role of SP antenna in light enhancement is the efficient coupling of incident light with the propagating wave in SOI layer. It also features additional contribution in enhancing the light by increasing the optical near field due to its surface plasmonic effect and by

increasing the photocurrent by controlling the depletion region as it can act as a gate electrode. The role of SP antenna on angle selective light enhancement and its effect of grating period and type of grating on the peak angle and the quantum efficiency will be discussed in detail in the next chapters.

2.3 Fabrication of SOI PD with SP antenna

The device fabrication is carried out by the following major steps. 1) At first, a commercial p-type SOI layer is taken and the SOI thickness is adjusted by

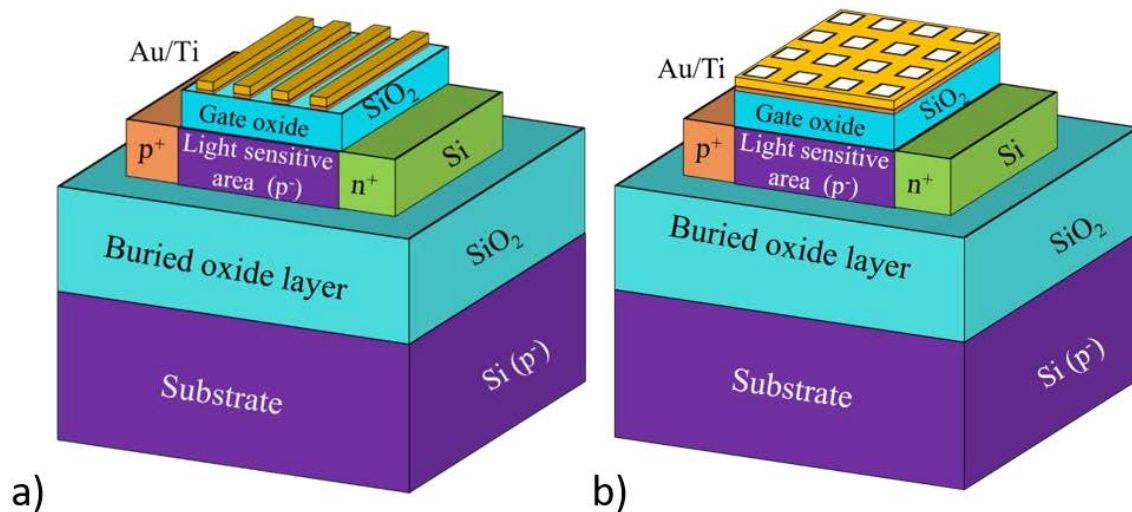


Fig.2.2 Bird's eye view of the SOI PD with SP antenna of a) 1D line and space grating and b) 2D hole array grating of grating period, p and width, w , respectively.

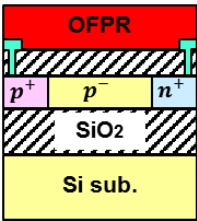
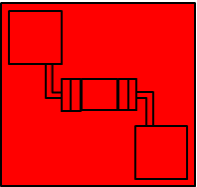
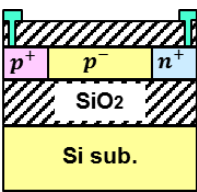
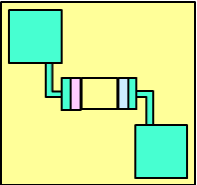
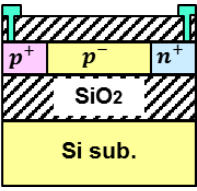
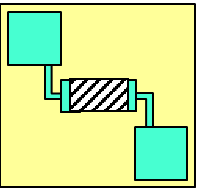
oxidation and etching of Si. The initial impurity of the ion (boron) concentrations in the SOI and the substrate are $1 \times 10^{15} \text{ cm}^{-3}$. 2) Next step is patterning of SOI to delineate Si with a width of W by photolithography and Si etching. 3) Ion implantation to the anode (BF_2^+) and cathode (As^+) regions of SOI. 4) Gate oxide layer formation by oxidation and chemical vapour

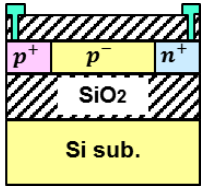
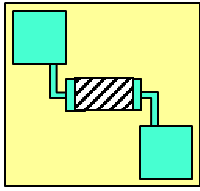
deposition (CVD) which is shown in detail in the Table 2.3.1.5) Patterning by electron-beam (EB) lithography, metal (Au and Ti) evaporations and liftoff to form SP antenna gate pads which is shown in detail in Table 2.3.2 and Table 2.3.3.

2.3.1 Adjustment of Gate Oxide Thickness (t_{GOX})

The thickness of the SOI PD of thickness $t_{SOI} = 100$ nm and $t_{BOX} = 400$ nm is adjusted by reactive ion etching (RIE) and measured by reflection spectrometer to a thickness of $t_{GOX} = 100$ nm and the process flow is displayed in Table 2.3.1.

Table.2.3.1 Substrate cutting and gate oxide (GOX) film thickness adjustment

Process	Content	Cross section	Surface
Dicing	[Scriber] Cut out to 21.4 mm × 21.4 mm SHSOI2012-2ndlot_01		
Resist removal	[Inorganic bench] acetone 3' × 3, ethanol 3', DIW 5', drying		
Process	Content	Cross section	Surface
Film thickness measurement	[Reflection spectrometer]		

Chamber cleaning	[Parallel Plate RIE System] Recipe#10(O ₂ 20 sccm, RF power 250 W, Pressure 50 Pa), Quartz tray, 30'		
SiO ₂ etching	[Parallel Plate RIE System] Recipe#1(CHF ₃ 20 sccm, RF power 250 W, Pressure 2 Pa), Carbon tray, (ER:about 1.0 ~ 1.2 nm/sec)		
Film thickness measurement	[Reflection spectrometer]		

2.3.2 Formation of Au SP Antenna

The antenna is formed by setting the different grating period, p in layout based on Virtuoso. The duty ratio (w/p) of the grating is designed as $w/p = 0.5$ and $(p-w)^2/p^2 = 0.5$ for 1D L/S grating and 2D hole array grating, respectively. Fig. 2.3 shows SP antenna layout for 1D and 2D grating represented as L/S and SQ, respectively. The formation of Au/Ti grating-type SP antenna of grating period, p , width w and thickness, $t_{Au/Ti} = 100/5$ nm by resist coating, patterning and developing by electron-beam (EB) lithography, metal (Au and Ti) evaporation and liftoff process which is described in detail in the process flow displayed in Table 2.3.2.

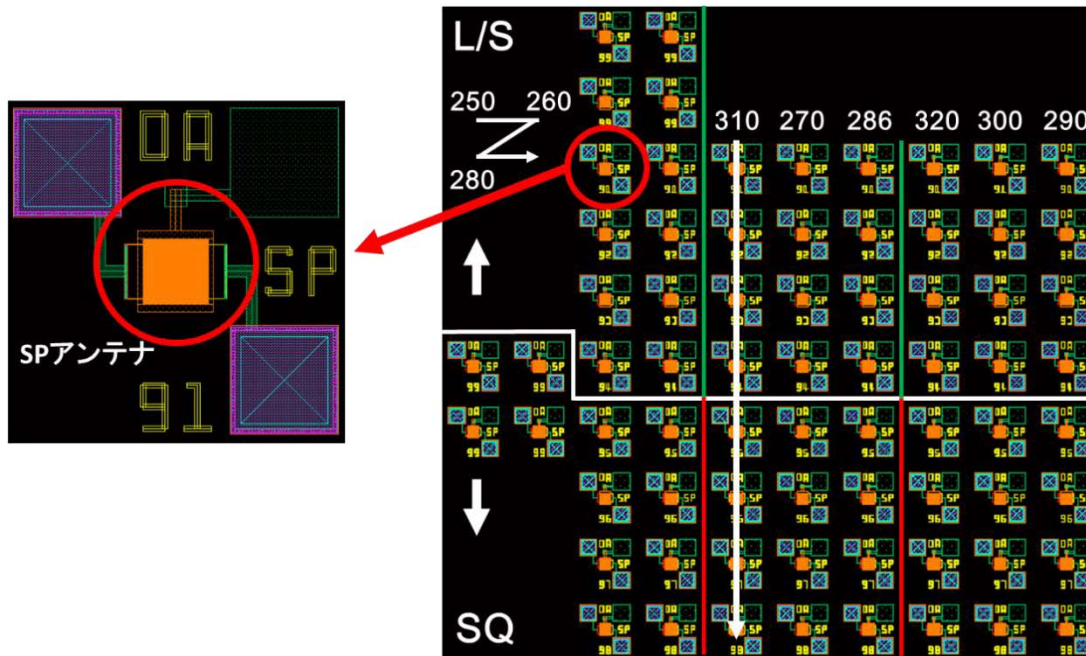
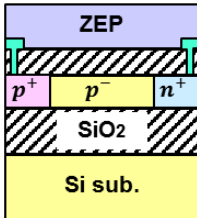
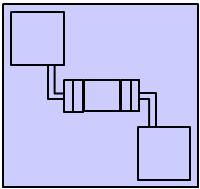
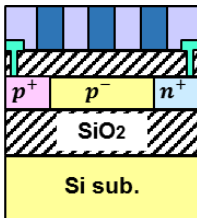
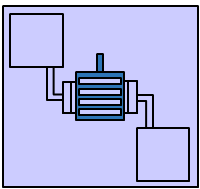
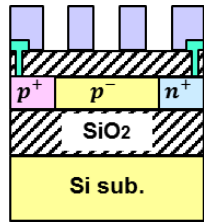
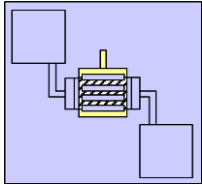
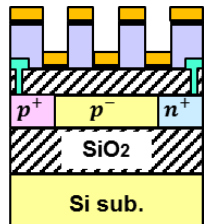
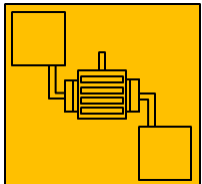
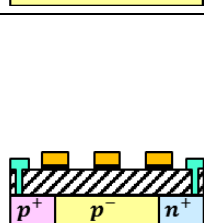
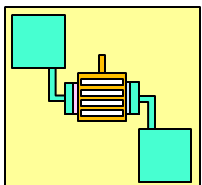
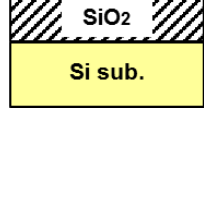
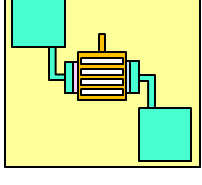


Fig.2.3 SP antenna layout for different grating periods, $p = 250 : 310$ and 286 nm for L/S (1D SP antenna) and SQ (2D SP antenna)

Table 2.3.2 Antenna formation

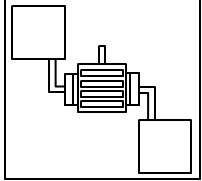
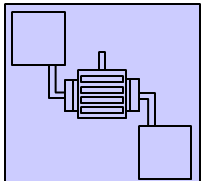
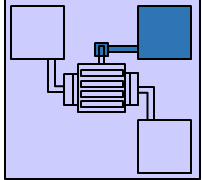
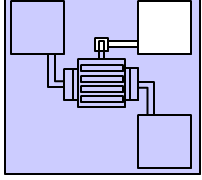
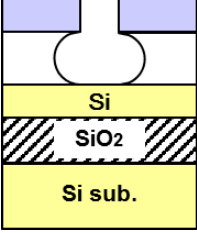
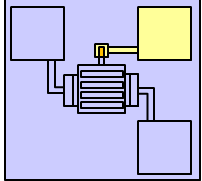
Process	Content	Cross section	Surface
Resist coating	[Spincoater] HMDS 3000 rpm 1', ZEP520A/ZEP-A=1:1 3000 rpm 1'10"		
Pre-bake	[Hot plate] 180 °C 2'		
EB drawing	[JEOL JBX-6300SP] Cell name: S_DASP_9, AccV: 100 kV, Lens Mode: 5th(high-resolution), BC: 100 pA, Dose: 160 $\mu\text{C}/\text{cm}^2$		

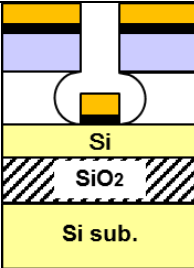
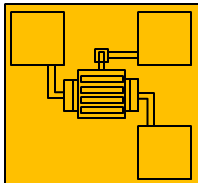
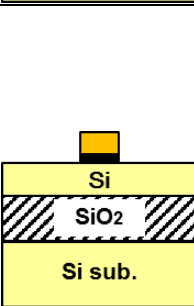
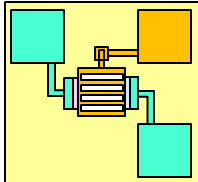
Developing	[Organic bench, thermostat] o-xylene 23 °C 2', IPA 40''		
Post bake	[Hot plate] 120 °C 5'		
Au evaporation	[EB evaporation system] Ti / Au = 5 nm / 50 nm		
Lift off	[Inorganic bench, ultrasonic cleaner] Remover1165 Left overnight, Ultrasonic cleaning 60 °C 1', Replace solution and ultrasonic cleaning 60 °C 40'		
Washing	[Inorganic bench] (ethanol 3', Ethanol wash bottle)×2, DIW 5'		

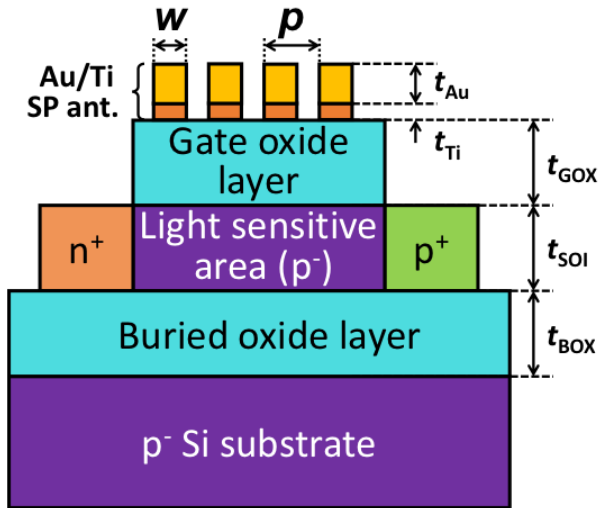
2.3.3 Formation of Gate Pad

The thickness of each layer of the fabricated device is shown in Fig. 2.4. The formation of gate pad involves deposition of resist in two layers over the SOI PD with SP antenna to achieve a proper production of metal pattern. The thickness of the two layered resists, PMGI and ZEP520A should be greater than the metal film thickness. The steps involved after resist deposition are EB drawing and development, Au deposition and finally the liftoff process. The detailed steps of gate pad formation is shown in Table 2.3.3.

Table 2.3.3 Gate pad formation

Process	Content	Cross section	Surface
Resist coating (lower layer) Pre-bake	[Spincoater] PMGI SF8S 15 drops in 300 rpm, 4500 rpm 1' [Hot plate] 190 °C 2'		
Resist coating (imaging) Pre-bake	[Spincoater] ZEP520A/ZEP-A=1:1 3000 rpm 1'10" [Hot plate] 180 °C 2'		
EB drawing	[JEOL JBX-6300SP] Cell name: S_DASP_9, AccV: 100 kV, Lens Mode: 4th(high-speed), BC: 10 nA, Dose: 205 uC/cm ²		
Development (imaging) Post bake	[Organic bench, thermostat] o-xylene 23 °C 2', IPA 40" [Hot plate] 120 °C 5'		
Development (lower layer) Post bake	[Organic bench, thermostat] NMD-3 23 °C 55", DIW 30" ×2 [Hot plate] 120 °C 5'		

Au evaporation	[EB evaporation system] Ti / Au = 20 nm / 300 nm		
Lift off	[Inorganic bench, ultrasonic cleaner] Remover1165 Left overnight, Ultrasonic cleaning 60 °C 1', Replace solution and ultrasonic cleaning 60 °C 40'		
Washing	[Inorganic bench] (ethanol 30'', Ethanol wash bottle)×2, DIW 5'		



Parameters	Dimensions (nm)
$t_{\text{Au/Ti}}$	100/5
t_{GOX}	100
t_{SOI}	100
t_{BOX}	400

Fig.2.4 Cross-sectional view of the SOI PD with SP antenna with the definition of the dimension corresponding to the thickness value of each layer in fabrication process shown in the table.

2.3.4 Device Packaging

After the fabrication of the SOI PD with SP antenna and gate pad formation for electrical contact, the device has to be packaged to carry out the measurement. The wiring is done for anode, cathode, gate and substrate connections of each PD. The package with many PDs is shown in Fig. 2.5. The detailed steps of process involved is shown in Table 2.3.4.

2.4 Measurement Setup for the Device

The packaged device is mounted over the experimental stage for measuring the output photocurrent. The photocurrent is measured to investigate the directivity of the device to the incoming light. For this purpose, we shed the laser light from the top of the device at a fixed position with the device varied at different incident angles, azimuth (ϕ) and elevation (θ) angle by using rotational and goniometer stages, respectively. Fig. 2.6 shows the configuration of the incident light with respect to the SP antenna to analyze the directivity of the device. The direction of the incident light is represented by azimuth (ϕ) and

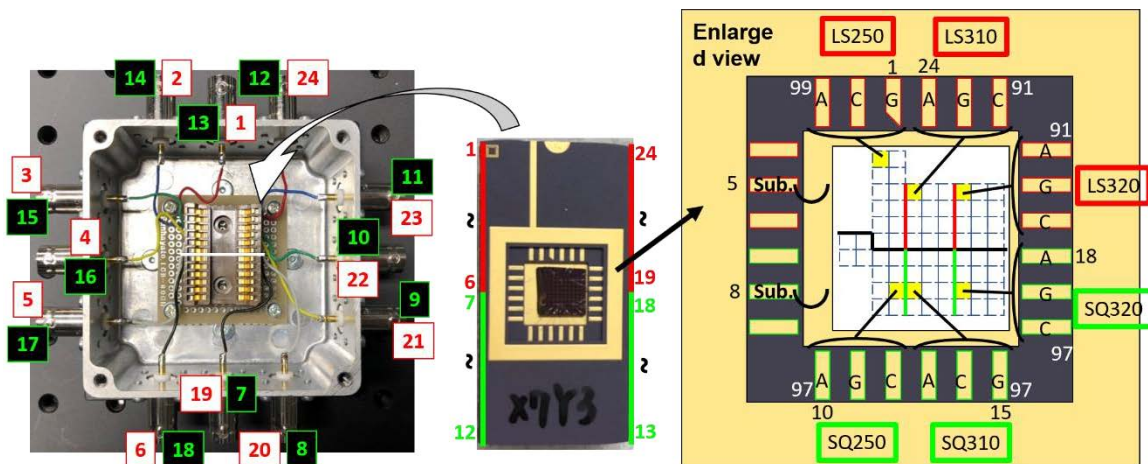


Fig.2.5 Packaged device with multiple SOI PD with SP antenna of 1D L/S (LS) and 2D hole array grating (SQ).

Table 2.3.4 Packaging

Process	Content
Resist coating	[Spincoater] HMDS 3000 rpm 1', OFPR 4000 rpm 16''
Pre-bake	[Hot plate] 110 °C 1'30''
Dicing	[Scriber] Cut out to 4.8 mm × 5.2 mm
Resist removal	[Inorganic bench, ultrasonic cleaner] acetone 3'(Ultrasonic) ×3, ethanol 3', DIW 5', drying
Paste silver paste	Adhere to package with silver paste D-362 100 °C 10'
Bonding	[Manual Wedge Wire Bonder] Use Al for the wire Bonding in the order of anode, cathode, substrate and gate

elevation (θ) angles. In the first investigation, the polarization of the incident light rotates along the azimuth angle of the light, i.e. the magnetic field component is rotated parallel to the equi- θ line and x-y plane. To achieve measurement in azimuth and elevation angle, rotational and goniometer stage with device is moved respectively while the polarization and incident angles of the light are in fixed position. Hence in this case the investigation is done only for a rotated polarization and not fixed polarization. To find the directivity of the device with the polarization dependence, we analyzed the azimuth-elevation angle dependence for a polarized light. The incident light configuration with the

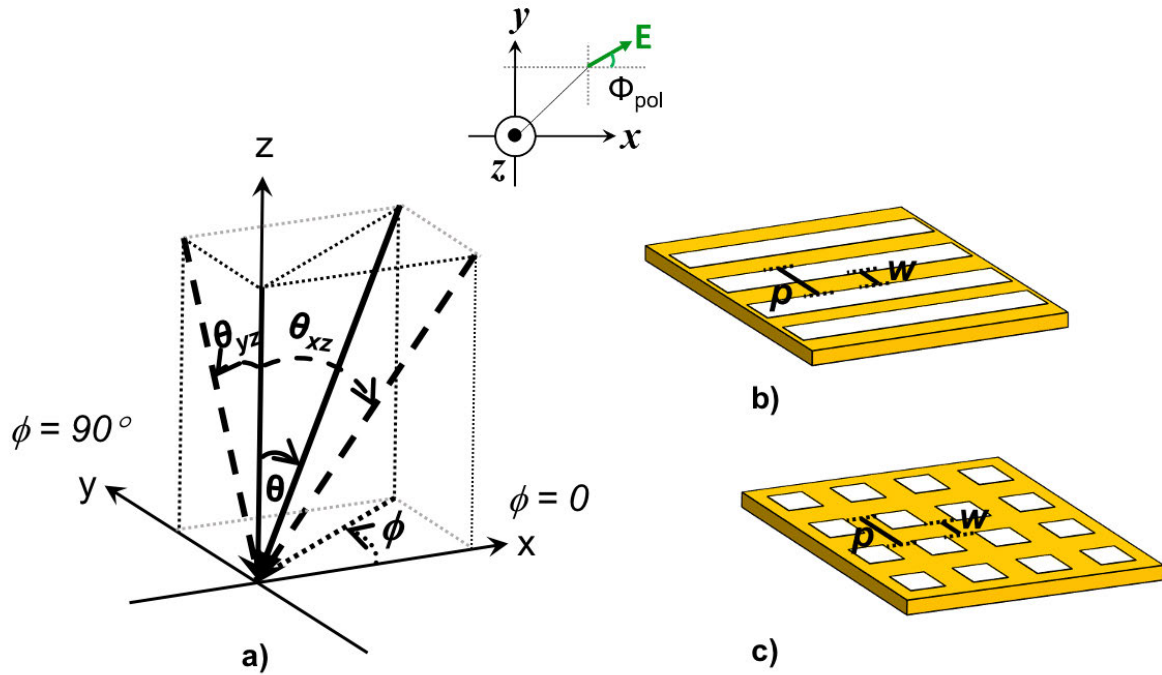


Fig.2.6 a) Azimuth (ϕ), elevation (θ) and polarization (ϕ_{pol}) angles of the incoming light, bird's view of the SP antenna, b) 1D L/S and c) 2D hole array grating.

definition of azimuth (ϕ), elevation (θ) and polarization (ϕ_{pol}) angles are shown in Fig. 2.6. θ_{xz} and θ_{yz} are the projections along the x-z and y-z plane, respectively. In order to achieve this configuration in the experimental demonstration, in which the incident laser light source is fixed, we employed one more gonio stage in this investigation. For the fixed polarized laser light source, the device is tilted along the x-z plane and y-z plane by alpha and beta gonio stage respectively and rotated along the azimuth angle by the rotational stage.

Chapter 3

THEORETICAL PRINCIPLE OF ANGLE SENSING

In this chapter the theoretical concept behind the angle sensing of our novel device, SOI PD with SP antenna of 1D L/S grating or 2D hole array grating is explained here[80]. Mathematical equation is formalized for predicting the angle detection of our device.

3.1 SOI Waveguide Modes

A basic planar optical waveguide structure consists of a high-index optical medium, called core or film sandwiched between the cladding layers (low-index optical media) in only one transverse direction, say z direction. The upper cladding layer can also be called as cover and the lower cladding layer can be called as substrate. The optical confinement is provided along one direction, i.e, z-direction. The propagation of the guided optical wave in the core is along the transverse direction. A planar waveguide supports both transverse electric and transverse magnetic modes. Our device structure consists of silicon photodiode sandwiched between a silicon dioxide layer (GOX and BOX). This SOI based structure offers excellent platform for Si/SiO₂ waveguide. A strong confinement is formed in the Si core layer, due to the large refractive index contrast between the core (Si) and the cladding (SiO₂) layer. The representation of the waveguide modes in the symmetrical slab waveguide is shown in Fig.3.1.

3.2 Dispersion Relation for SOI Waveguide

To understand the basic concept of light enhancement in our proposed device, it is important to understand the waveguide modes propagating in the

waveguide. The characteristics of the lateral light propagation in the SOI slab with respect to the incident light could be understood by estimating the dispersion relation for the symmetrical slab waveguide with 100-nm-thickness core layer and infinite-thickness upper and lower claddings by the following transcendental equations[81],

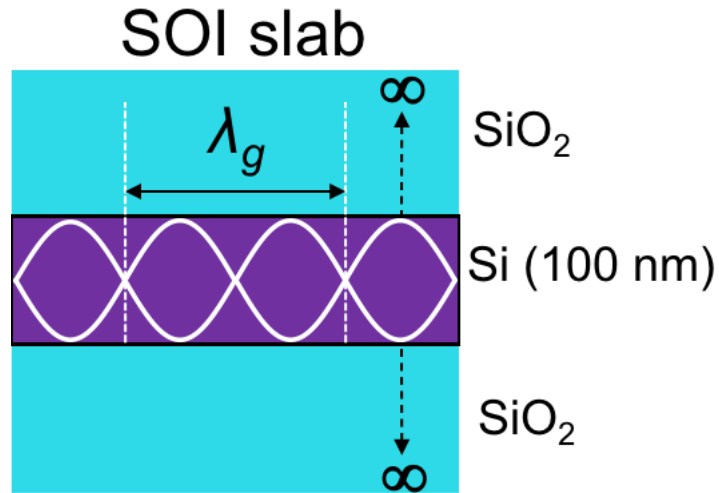


Fig.3.1 Symmetrical slab waveguide consists of Si core and SiO₂ claddings

For TE modes,

$$\tan\left(\frac{ht_{core}}{2} - m\frac{\pi}{2}\right) = \frac{\sqrt{V^2 - h^2 t_{core}^2}}{ht_{core}} \quad (m = 0, 1, 2, \dots)$$

(3)

For TM modes,

$$\tan\left(\frac{ht_{core}}{2} - m\frac{\pi}{2}\right) = \frac{n_{core}^2}{n_{clad}^2} \frac{\sqrt{V^2 - h^2 t_{core}^2}}{ht_{core}} \quad (m = 0, 1, 2, \dots)$$

(4)

where,

$$h = \sqrt{\left(\frac{2\pi n_{core}}{\lambda}\right)^2 - \left(\frac{2\pi}{\lambda_g}\right)^2},$$

$$V = \frac{2\pi}{\lambda} t_{core} \sqrt{n_{core}^2 - n_{clad}^2},$$

t_{core} is core (Si) thickness (100 nm in our design), n_{core} and n_{clad} are the refractive indices for core (Si) and claddings (SiO₂), respectively. λ and λ_g are the free space wavelength and the propagation wavelength, respectively. The wavelength dependence of the propagation wavelength in the Si layer with respect to the interaction of the incident wavelength could be plotted using the transcendental equations calculated. Fig.3.2 shows the propagation wavelength of the SOI waveguide for each waveguide mode vs. free space wavelength[74].

3.3 Characteristics of the Device

3.3.1 Wavelength Selectivity

The conventional SOI photodetector consists of pn-junction photodiode formed in the silicon layer supported by a SOI substrate as shown in Fig.3.3 a). Due to the thin size of the silicon layer which acts as the absorber layer, photodiode suffers from less light absorption efficiency. To solve this problem our research group incorporated an additional structure without increasing the size of the absorber. A single layered thin structure (around 100 nm), Au surface plasmon antenna is mounted over the lateral pn-junction photodiode as shown in Fig.3.3 b). The surface plasmon antenna enhances the optical near field and efficiently couples the incident light with the waveguiding modes in the SOI

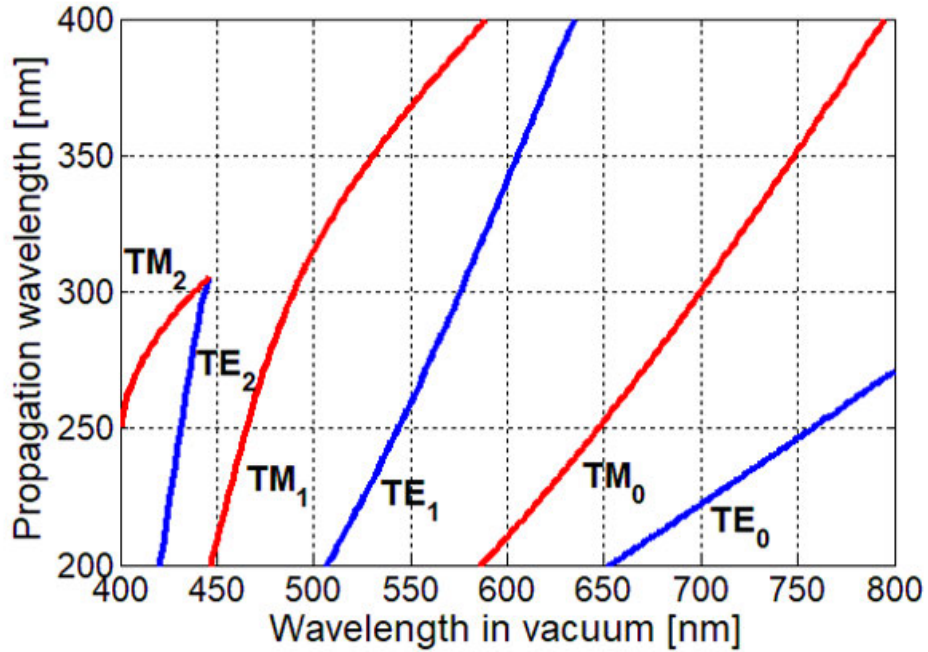


Fig.3.2 Propagation wavelengths of the lateral waveguide modes in SOI layer vs. free-space wavelength. Propagation wavelengths are obtained by solving the Eq.(1)&(2) for symmetrical slab waveguide composed of 100-nm-thick Si core and infinite-thick SiO₂ claddings [75].

layer. Due to this strong coupling of waves, the light absorption is enhanced efficiently.

The spectroscopic quantum efficiency has been measured for the SOI PD with and without Au L/S grating for different grating period, p when a TM polarized light with normal incidence angle, $\theta = 0$ is illuminated over it (Fig.3.4). The grating period dependence is investigated in conjunction with the waveguide modes in the SOI. The duty ratio of L/S grating is chosen as $w/p = 0.5$. Fig 3.5 shows the measured spectroscopic quantum efficiencies for SOI PD

with and without grating[75]. For SOI PD without grating, the peak at which maximum efficiency occurs appears at the wavelength of 445 nm due to the

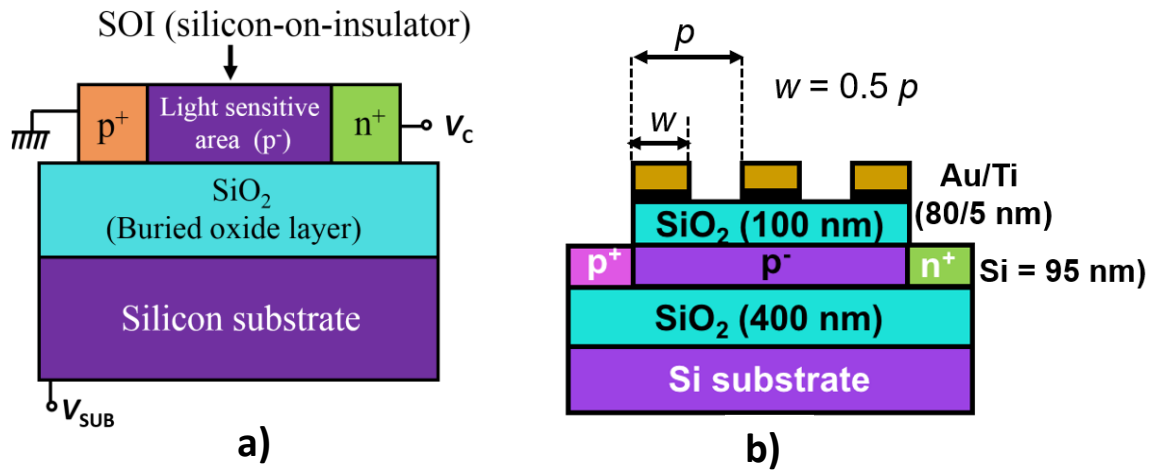


Fig.3.3 a) Conventional SOI photodiode b) SOI photodiode with SP antenna.

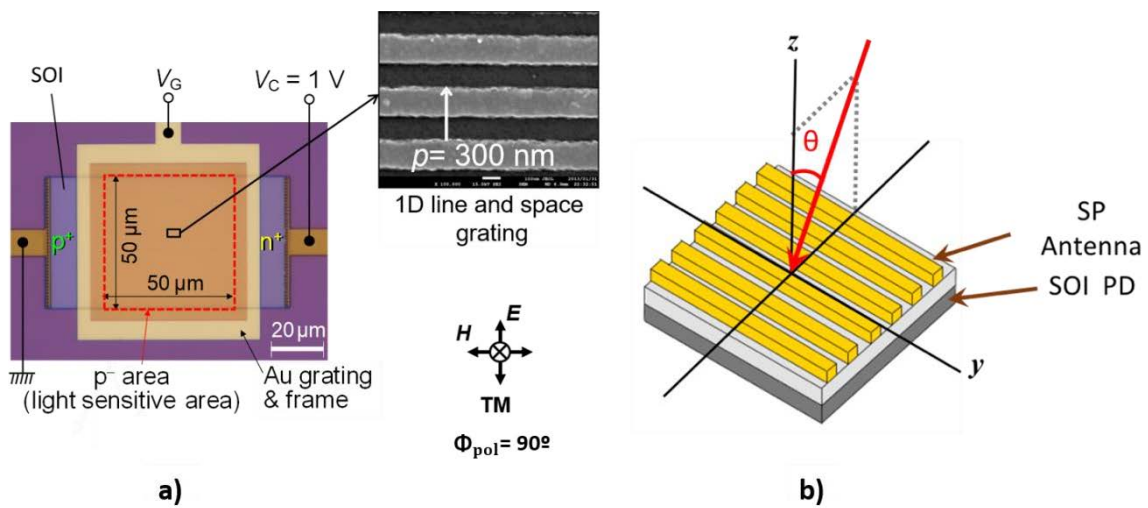


Fig.3.4 SOI PD with SP antenna a) top view (fabricated) b) bird's eye view with angle definition.

high absorption coefficient of silicon in the shorter wavelength region and interferences in the multiple layered device. However, it shows decrease the quantum efficiency at longer wavelengths greater than 500 nm. For the case of SOI PD with Au grating, the light enhancement occurs at the wavelength range from 650 to 750 nm. In the case of grating period, $p = 300$ nm the quantum efficiency reaches 25% at the from the Au grating and the TM waveguide modes (TM_0 and TM_1) in lateral SOI PD. This property of SP antenna enables the integration of multi-wavelength of 680 nm. This peak wavelength could be tuned by controlling the grating period p . Thus, SP antenna enhances the light with wavelength selective nature. Such a characteristic is due to the coupling between the diffracted light wavelength photodetectors in a single chip by simply fabricating with different grating periods. This kind of wavelength selective behaviour could be achieved with the case of TE polarized light as

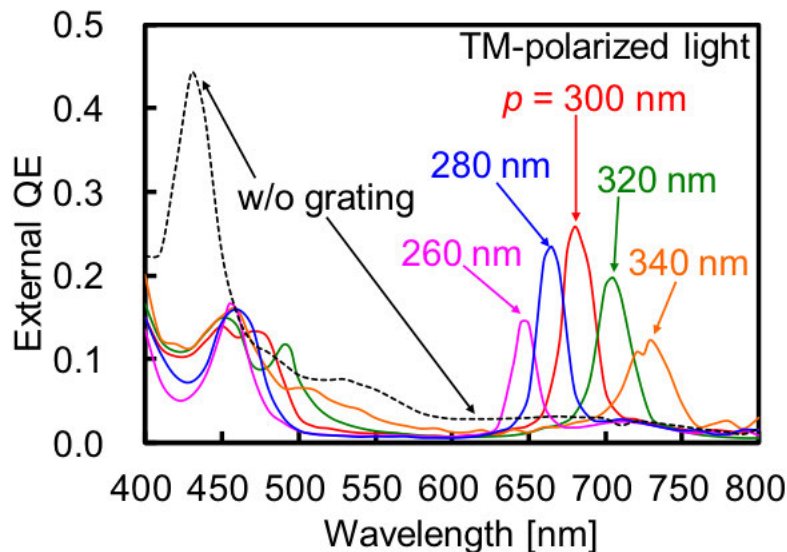


Fig.3.5 Spectroscopic quantum efficiency of SOI PD with and without Au L/S grating for different grating periods, p .

well, by the coupling of diffracted light with the TE waveguide mode in the SOI layer.

To clarify the reason behind the tuning of wavelength by grating period, the measured peak QE of each grating period could be compared with the analytically calculated wavelengths. The dispersion relation solved for the SOI slab waveguide in Eqs. 1 & 2 is used to plot the propagation wavelengths of lateral waveguide modes in the SOI layer vs the free space wavelength as in the previous section and in the same graph we can plot the grating period vs. peak wavelength for comparing the relation between them. These two relations coincide with each other well, indicating that the incident light is strongly

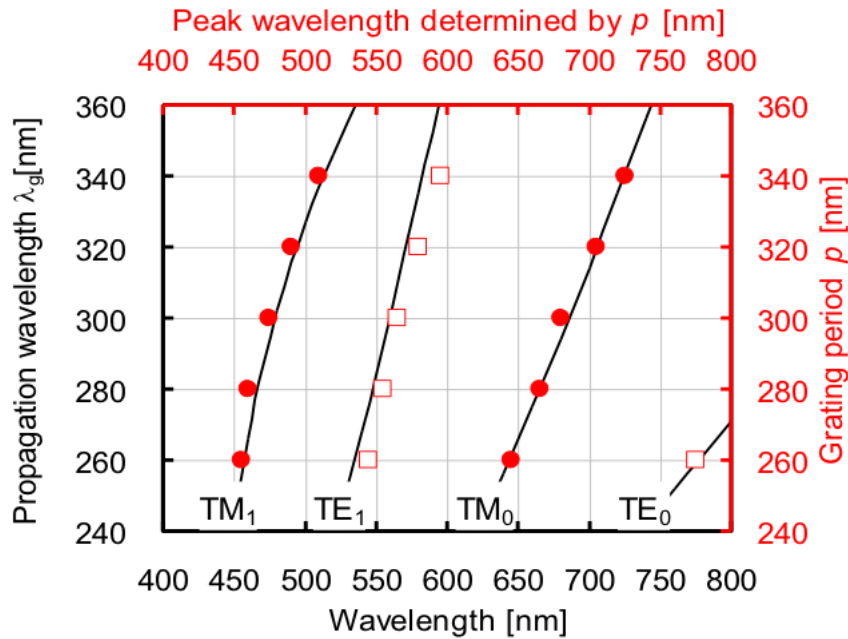


Fig.3.6 Comparison of the relation between the theoretically calculated propagation wavelength vs. free space wavelength and experimentally measured peak wavelength vs. grating period.

coupled to the waveguide mode in SOI layer and absorbed when period is equal to propagation wavelength. Therefore, the peaks with high QE in Fig.3.5 are caused mainly by the coupling of incident light with the waveguide modes and not mainly by the SP excitations around the Au grating). In the Fig.3.6 the peaks in the wavelength range from 650 to 750 nm and from 450 to 550 nm corresponds to the fundamental TM (TM_0) mode and first-order TM (TM_1) mode in the SOI layer respectively[74].

3.3.2 Role as gate electrode

The SP antenna is surrounded by a frame and all the metallic lines of the antenna are connected electrically. Thus, this SP antenna can work as gate electrode for biasing the entire p- region i.e. light sensitive area. When bias voltage is applied to this gate and the substrate electrodes, the depletion region

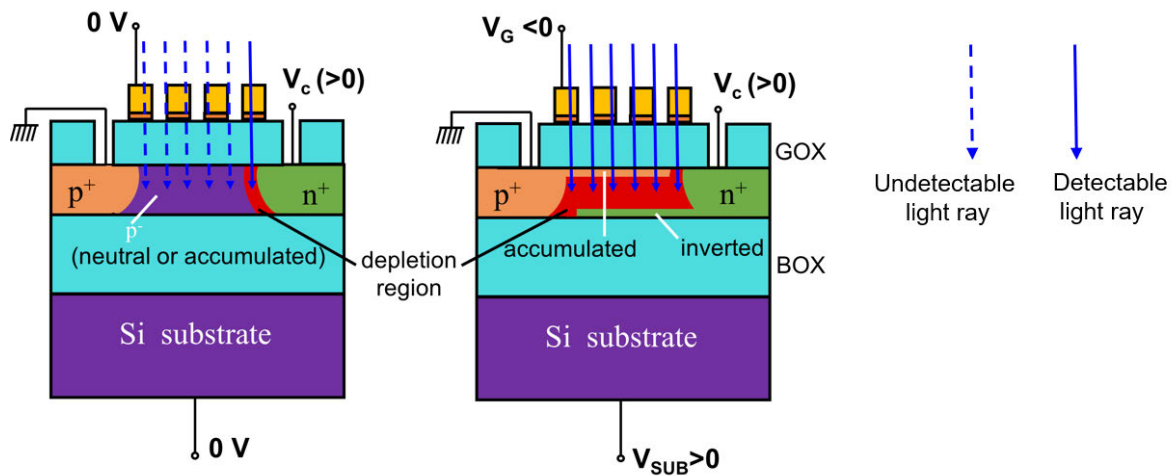


Fig.3.7 Schematic models of different external quantum efficiencies depending on conditions of depletion region. Solid and dotted arrows indicate detectable and undetectable light rays, respectively, due to position and volume of depletion region [75].

can be controlled to yield a maximum external QE. When no biases are applied, the depletion region volume is very less and QE becomes low due to the less detectable light rays[75].

3.3.3 Polarization Selectivity

Our previous study involves the investigation of polarization dependence of the SOI PD with Au L/S grating of period, $p = 300$ nm with a TM-polarized incident light of wavelength 680 nm. This incident wavelength is equal to the peak wavelength of $p = 300$ nm under TM polarized light as shown above in the wavelength selectivity spectroscopic response graph. The SOI PD without Au grating does not show any polarization dependence. However, the SOI PD with Au grating exhibits polarization dependence. The external QE achieved by this incident light is 25% at polarization angle 0 deg and the enhancement is seen until 70 deg and for 90 deg i.e. TE mode there is no enhancement as shown in Fig. 3.7.a). In Fig. 3.7.b) and c) the spectroscopic characteristics is shown for the TM polarized light and TE polarized light respectively. This shows the polarization selective enhancement behaviour of the device [66].

3.3.4 Material Dependence of SP Antenna

The SP antenna is fabricated by Au metal in our research. However, other noble metal such as silver, or aluminium could also be considered. We have also done investigation on the material dependence of L/S metal grating in terms of light enhancement by measuring the external quantum efficiency. The investigation shows that any grating material can enhance the light sensitivity. The peak wavelengths which could be controlled by the grating period, are not much affected by the grating material. The peak wavelength is determined only

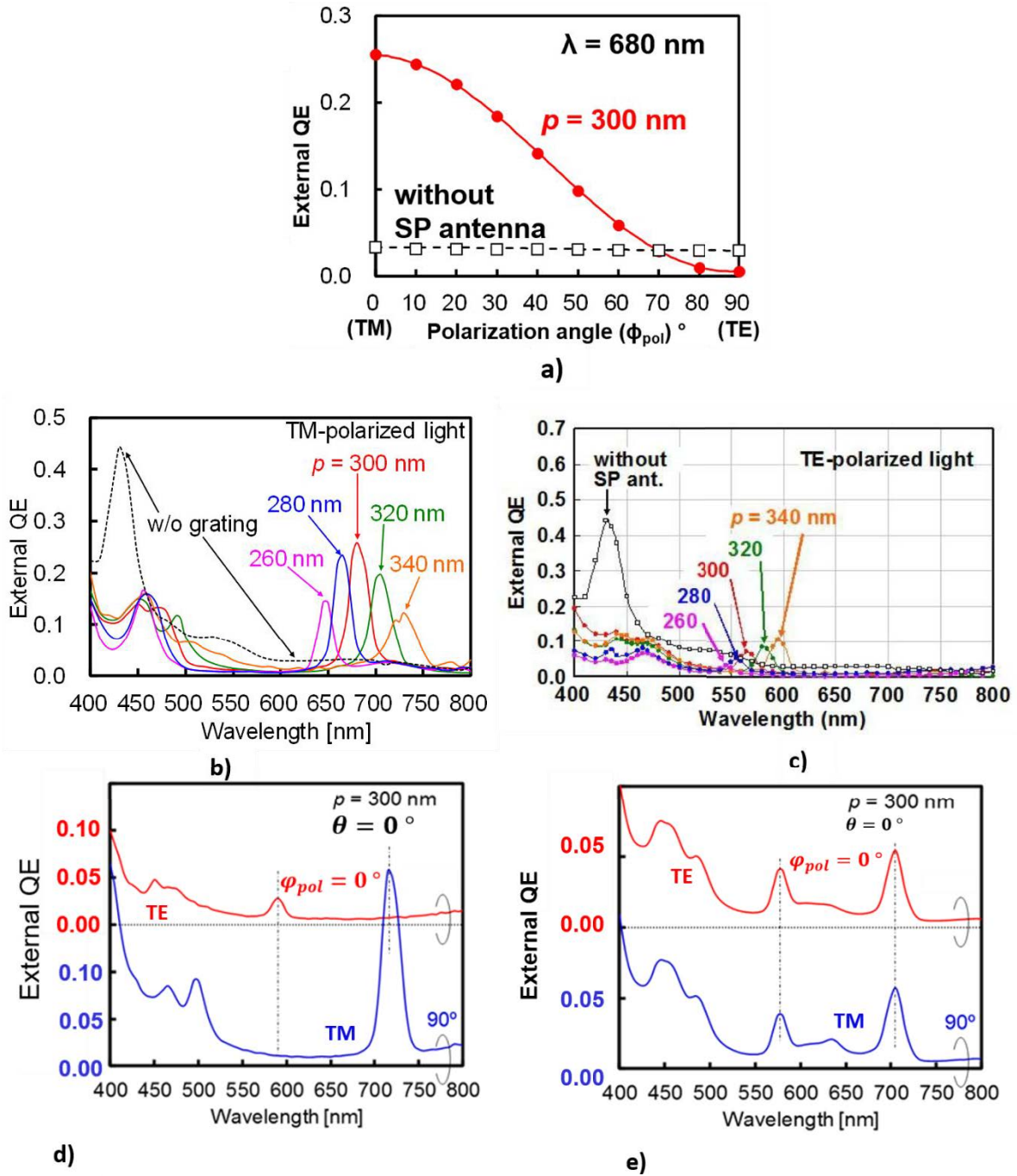


Fig.3.8 Polarization dependence of SOI PD with L/S grating a) polarization angle is varied from 0 to 90 $^\circ$, spectroscopic characteristics of b) TM polarized light and c) TE polarized light, comparison of TE and TM at fixed p for L/S and hole array.

by the grating period and is independent of the material used. The principle of enhancement is clarified that the coupling between the diffracted light and the lateral propagating mode is responsible for light enhancement as shown in Fig. 3.9 and 3.10 [66].

3.3.5 Incident Angle Selectivity

The characteristics of SOI PD with Au L/S grating for various light incident angles, have also been investigated in our previous research. As shown in Fig.2.4 b) the incident angle of the incoming light is varied in 1D direction (θ). A TM polarized monochromatic incident light is illuminated over the PD to measure the quantum efficiency [62]. Fig.3.11 shows the spectroscopic external QE of the fabricated photodiode with grating period, $p = 300$ nm for different incident angles θ and the simulated device (FDTD). The graph shows two peaks at 490 and 700 nm at normal incidence. We have already shown that the peak wavelength could be tailored by period. The current graph shows an interesting behaviour of peak splitting when the incident angle is changed. The separation between the peaks increases as the θ increases. This kind of peak splitting occurs only when the incident light is tilted perpendicular to the grating orientation as shown in Fig.3.4 b).

This concept of peak splitting with the incidence angle could be explained based on the physical concept called phase matching condition. This phenomenon is based on the phase matching between the diffracted light from the antenna surface and the waveguide modes in the SOI slab as shown in Fig.3.12. When the incident light is tilted perpendicular to the grating, phase

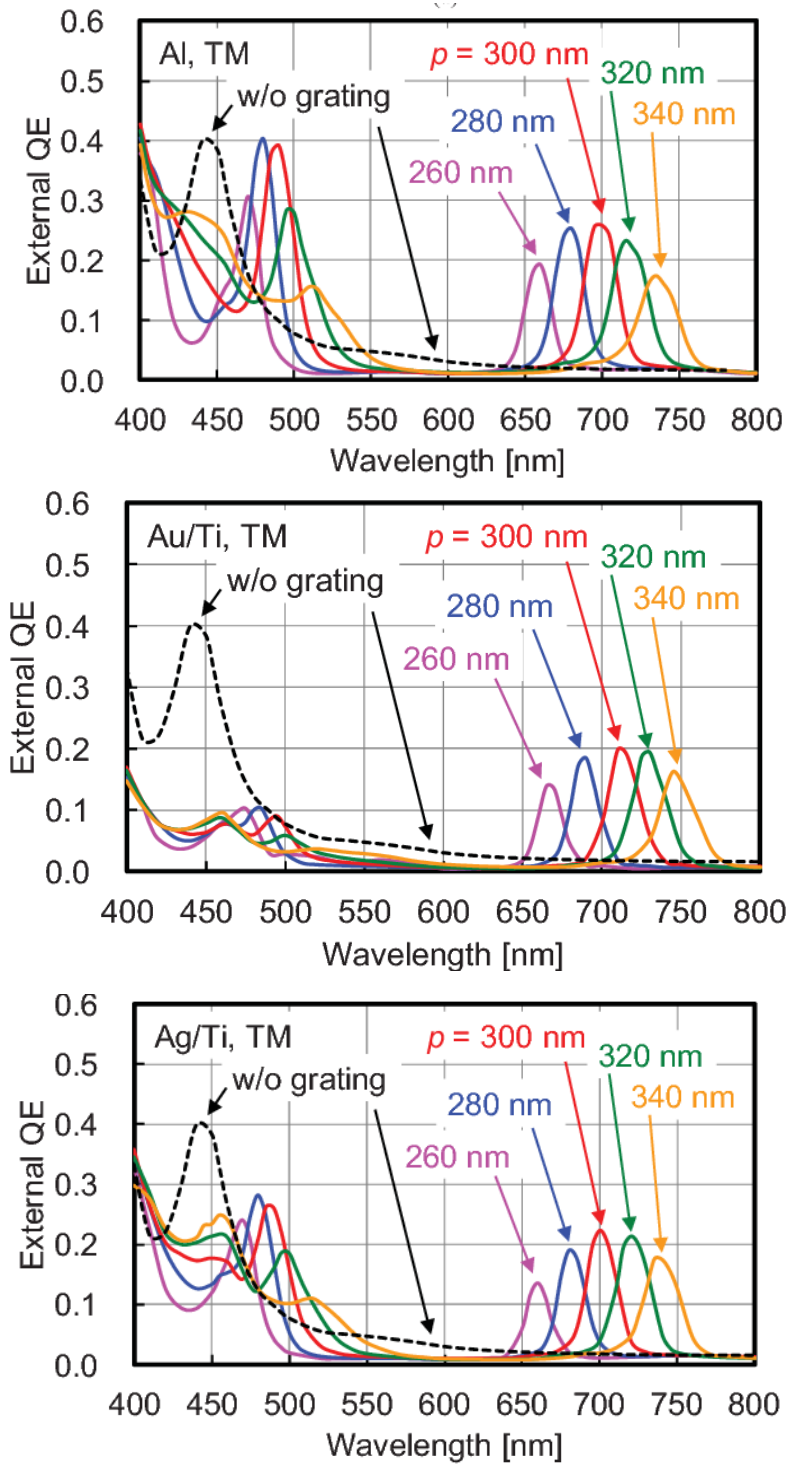


Fig.3.9 Spectroscopic quantum efficiency for SOI PD Al, Au and Ag SP antenna.

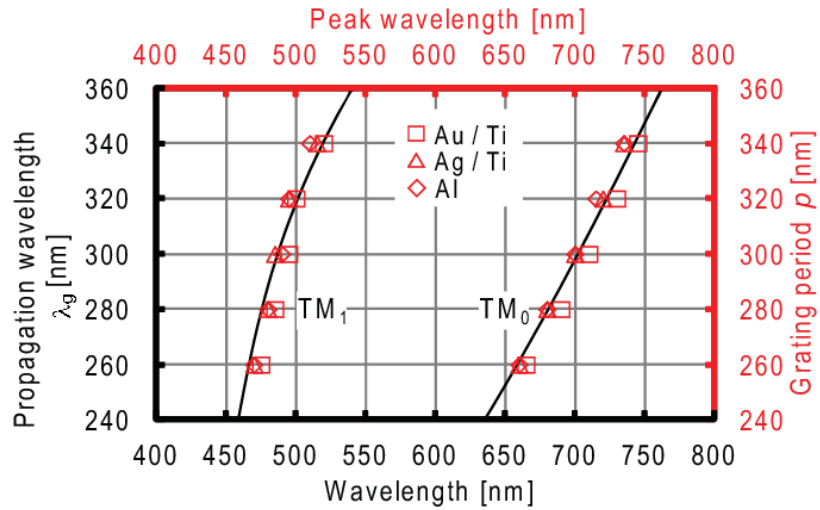


Fig.3.10 Comparison between relationships of propagation wavelength λ_g of lateral waveguide modes in SOI layer vs. free-space wavelength and peak wavelength of external QE vs. grating period p in Figs.3.8. [66]

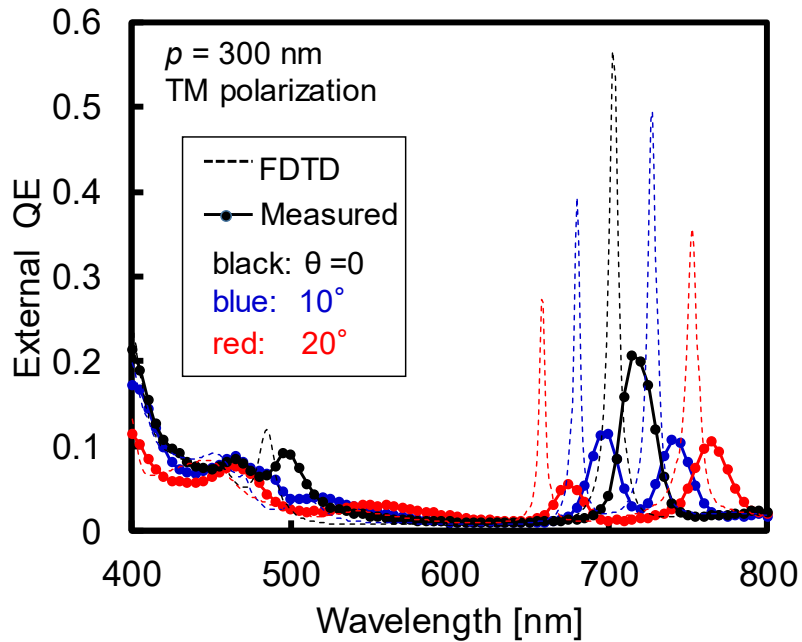


Fig.3.11 Spectroscopic quantum efficiency for SOI Pd with $p = 300$ nm under different incident angles, θ .

difference Δ occurs between the incident between the adjacent lines in the grating.

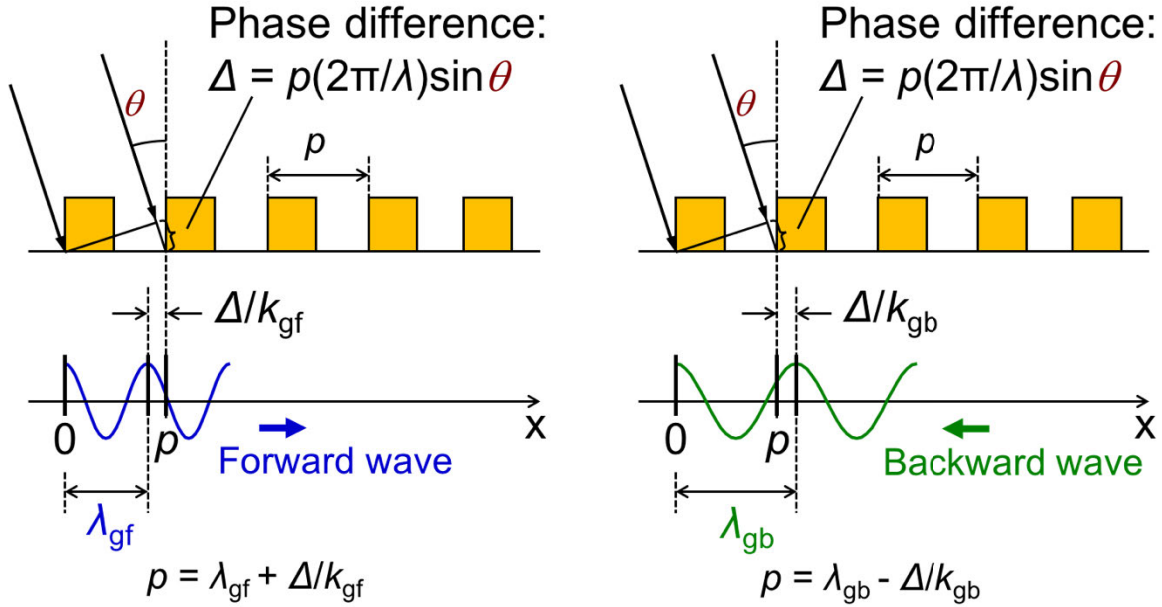


Fig.3.12 Phase matching conditions between diffracted light from antenna and forward or backward waves in the SOI waveguide. λ_{gf} and λ_{gb} are propagation wavelength for forward and backward waves, respectively, and $k_{gf} = 2\pi/\lambda_{gf}$ and $k_{gb} = 2\pi/\lambda_{gb}$ are wavenumbers for forward and backward waves, respectively.

Due to the phase difference, the phase matching conditions for forward and backward waves is different and the propagation wavelength for the forward and backward wave is

$$\lambda_{gf} = 1/\{(1/p) + (1/\lambda)\sin\theta\} \quad (3)$$

$$\lambda_{gb} = 1/\{(1/p) - (1/\lambda)\sin\theta\} \quad (4)$$

respectively. The equation (3) represents for the shorter wavelength and equation (4) represents for the longer wavelength to give λ_{gf} and λ_{bf} respectively.

Fig.3.13 compares the relation between the analytical dispersion curves for the waveguide modes propagating in the silicon slab sandwiched between the infinitely thick SiO₂ cladding layers and the experimentally obtained data for different grating periods and incident angles. These coincide well and clarifies the validity of the above discussion, and the simplicity of the working mechanism. Based on the equations (3) and (4), we can also solve the incidence angle detection by different grating periods with spectroscopic characteristics as shown in Fig.3.14. A sinusoidal response is obtained for each devices with grating period for a wide range of propagation wavelength. At normal incidence when the grating period is equal to the propagation wavelength maximum light

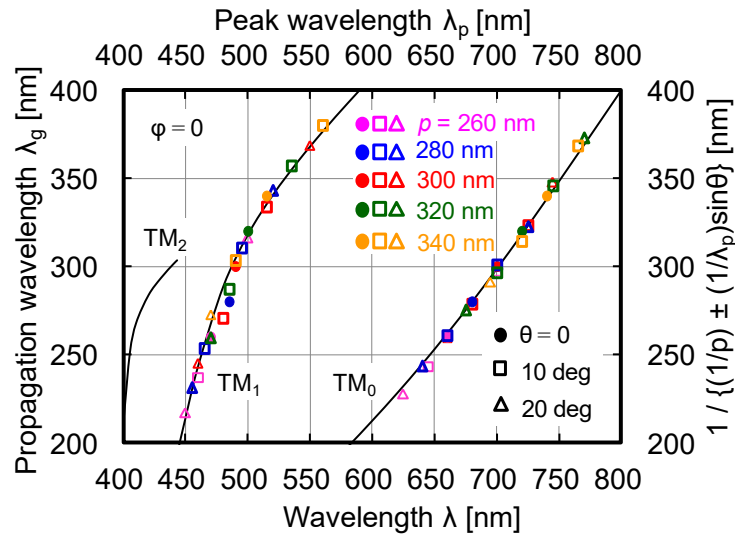


Fig.3.13 Comparison of theoretical and experimental dispersion curves for waveguide modes in the SOI slab for different grating period and light incident angles

absorption occurs. Therefore, the light incident angle is controlled by the peak wavelength and period and purely works on phase matching condition between the diffracted light and the lateral waveguide mode.

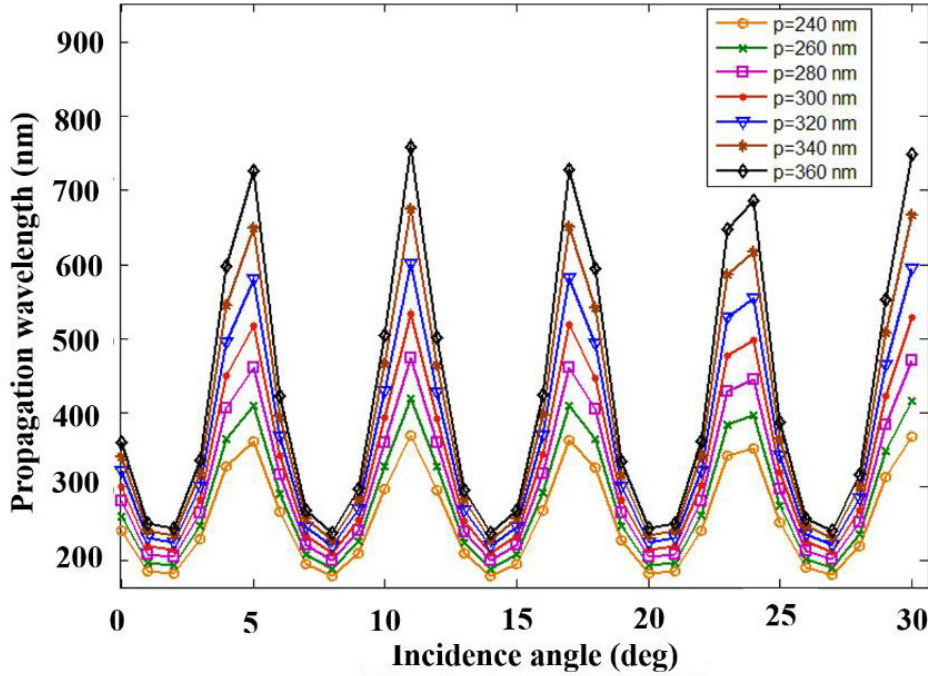


Fig.3.14 Propagation wavelength of different grating periods, p at different incident angles.

3.4 Theoretical Modelling of Peak Angle

The concept of angle detection by SOI PD with SP antenna is discussed by considering a monochromatic incident light of wavelength 685 nm throughout this study. The incident light is rotated by azimuth angle, ϕ and elevation angle, θ with respect to the grating direction as shown in Fig.3.15 in which E, H and S indicates the electric field, magnetic field and Poynting vector. The magnetic field is rotated along the equi- θ line and x-y plane. The angle

dependence could be predicted based on the phenomenon of phase matching condition. In the previous research the wavelength dependence for wide range for different period and light incidence angle was calculated and discussed. In the current research we analyse the angle with fixed wavelength.

The propagation wavelength of each waveguide mode corresponding to the wavelength of the incident light could be calculated for a given SOI thickness by using the transcendental equations. The directivity of the SOI PD with SP antenna can be find out based on the phase matching condition between the diffracted light from the SP antenna and the propagating wave in the SOI symmetrical slab waveguide as show in Fig.3.16. for the case of wave propagation in x direction.

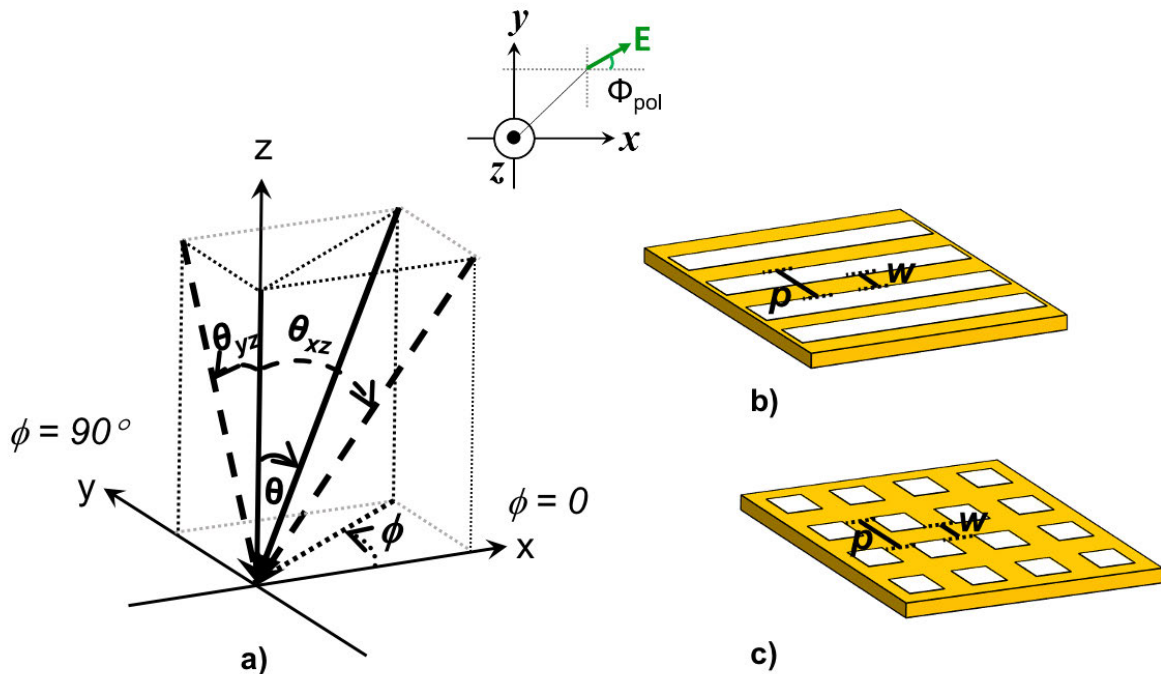


Fig.3.15 a) Azimuth (ϕ), elevation (θ) and polarization (ϕ_{pol}) angles of the incoming light, bird's view of the SP antenna, b) 1D L/S and c) 2D hole array grating.

When the incident light is tilted by projecting S on x-z plane, the phase shift Δ between the light waves entering the adjacent lines in the antenna is given by,

$$\Delta = p (2\pi / \lambda) \sin\theta_{xz} \quad (5)$$

and

$$\theta_{xz} = \tan^{-1} (\tan \theta \cos \phi) \quad (6)$$

where p is the period and λ is the wavelength in the free space. This phase shift results in different phase matching conditions for forward wave,

$$\theta_{xz} = \sin^{-1}\lambda [(1/ \lambda_{gf}) - (1/p)] \quad (7)$$

and for backward wave

$$\theta_{xz} = \sin^{-1}\lambda [(1/p) - (1/ \lambda_{gb})] \quad (8)$$

where λ_{gf} and λ_{gb} are respective propagation wavelengths in the SOI PD (SOI slab waveguide). For the waves propagating in the y direction, θ_{yz} in place of θ_{xz} should be considered.

$$\theta_{yz} = \tan^{-1} (\tan \theta \sin \phi) \quad (9)$$

For our device with t_{SOI} and given λ , the corresponding λ_g is found out, and then the peak angle that satisfy the phase matching condition and expectedly offers maximum quantum efficiency is obtained for a desired p by the solving the Eq. (6) or (9) and Eq. (7) or (8). Note that Eq. (7) is used when $p > \lambda_g$, and Eq. (8) is for $p < \lambda_g$. The 1D L/S grating SP antenna shows efficient coupling only for the propagating waves in y direction.

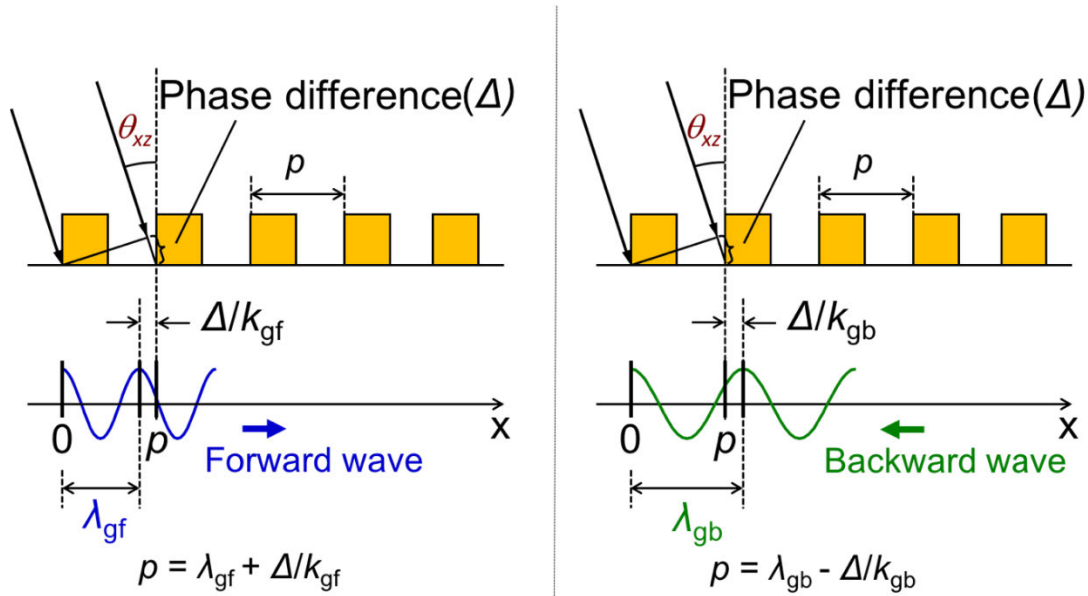


Fig.3.16 Phase matching conditions between diffracted light from antenna and forward or backward waves in the SOI waveguide. λ_{gf} and λ_{gb} are propagation wavelength for forward and backward waves, respectively, and $k_{gf} = 2\pi/\lambda_{gf}$ and $k_{gb} = 2\pi/\lambda_{gb}$ are wavenumbers for forward and backward waves, respectively. θ_{xz} is the elevation angle of light projected on x - z plane. θ_{yz} should be considered instead of θ_{xz} when the waves propagate in y

3.4.1 Elevation Angular Dependence (θ)

We first show the elevation (θ) angular dependence, by varying only elevation angle and azimuth angle as fixed for the SOI PD with SP antenna of silicon slab thickness, $t_{SOI} = 100$ nm for the TM waveguide mode at a fixed wavelength of 685 nm ($\lambda_g = 285.5$ nm). By using the equations for phase matching conditions (θ_{yz} for the forward waves) for a given wavelength and fixed azimuth angle of 90° , we can calculate the elevation angle detection of different grating periods, p ranging from 285 to 340 nm at an interval of 5 nm. The theoretical analysis is represented in the graph, Fig.3.17. The graph shows

a linear increment in the peak angle as the grating period increases. The prediction of peak elevation angle at which the light absorption of the device is high for 12 different periods is analysed. From the graph it is clearly shown that each period provides a distinct peak elevation angle. The peak angle could be tuned by the grating period. Thus, devices with different grating period when constructed in a single chip, it may facilitate light field imaging with detection of light from different angles.

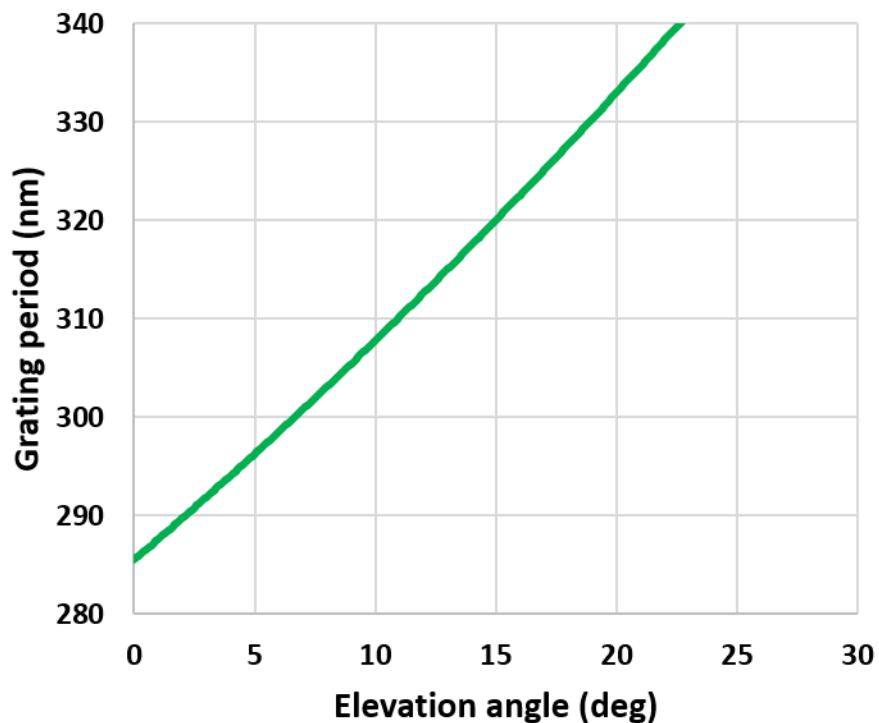


Fig.3.17 Elevation angle prediction for different grating periods, p at fixed incident wavelength, $\lambda = 685 \text{ nm}$ (theoretical and numerical estimation).

3.4.2 Azimuth-Elevation Angular Sensitivity (θ and ϕ)

The theoretical estimation for predicting the arrival of the incoming angle has been done in previous section by calculating the elevation angle. However,

elevation angle alone could not tell the user exactly about the direction of the incoming light. The light may be incident on the surface of the image sensor either at the right or left side of the normal plane of the sensor. Therefore, it is important to detect the direction of light in 2D. We can predict the capability of our device to detect the azimuth-elevation angular information of the incoming light as discussed in this section. In the previous section, by using the equations of phase matching condition we predicted the peak elevation angle at fixed azimuth angle.

Now, we can predict the peak elevation angle at all azimuth angles by using

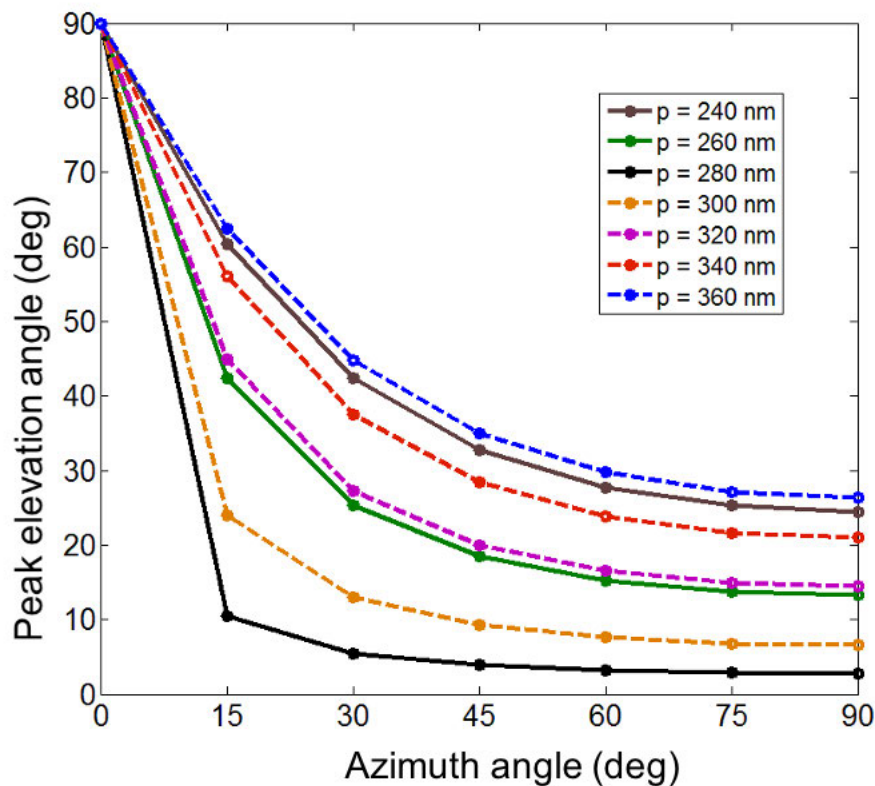


Fig.3.18. Azimuth and elevation angle dependence for different grating periods, p .

the theoretical equations. In this case as shown in Fig.3.15 a) the polarization component, magnetic field is rotated parallel to the equi- θ line. Fig.3.18 represents the theoretically calculated peak elevation angle vs. azimuth angle. This azimuth-elevation angular data can be more easily represented in the form of 2D graph, spatial pattern. Spatial pattern represents the azimuth-elevation angular distribution using the polar coordinates to clearly show the full sphere of optical information impinging on the device.

Fig.3.19 is the theoretical spatial pattern which represents the azimuth and elevation direction of the incident light (elevation angle and azimuth angle as radial and polar axes, respectively) for the SOI PD with L/S grating SP antenna with $t_{SOI} = 100$ nm and $p = 300$ nm. The high quantum efficiency locus for TM_0 mode is predicted and represents a two-fold symmetry. Fig. 3.20 shows

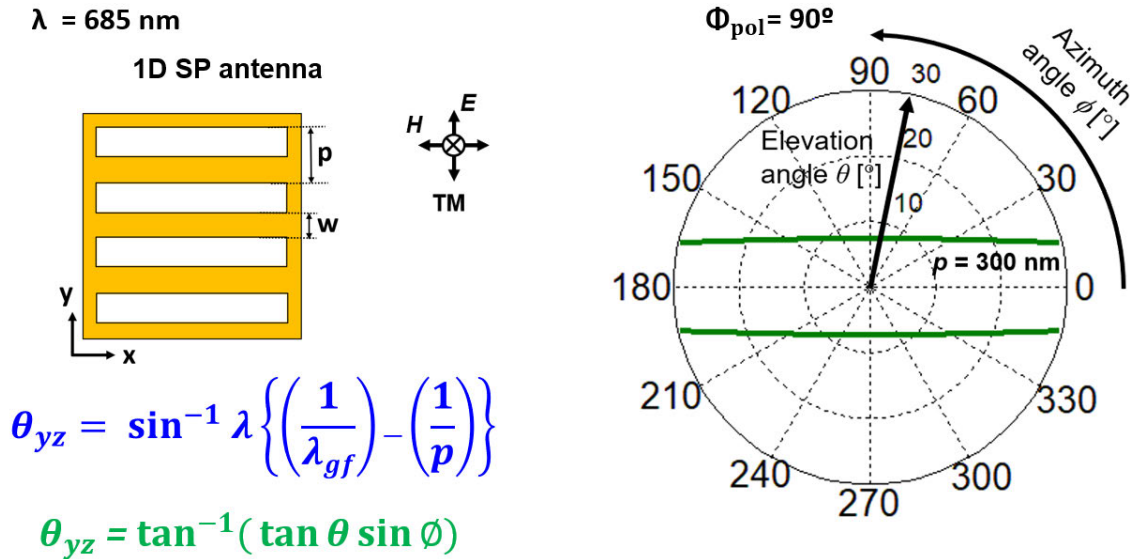


Fig.3.19. Theoretical spatial patterns with respect to the azimuth (ϕ) and elevation angles (θ) for $t_{SOI} = 100$ nm, $\lambda = 685$ nm ($\lambda_g = 285.5$ nm (TM_0 mode)) and $p = 300$ nm for 1D L/S grating

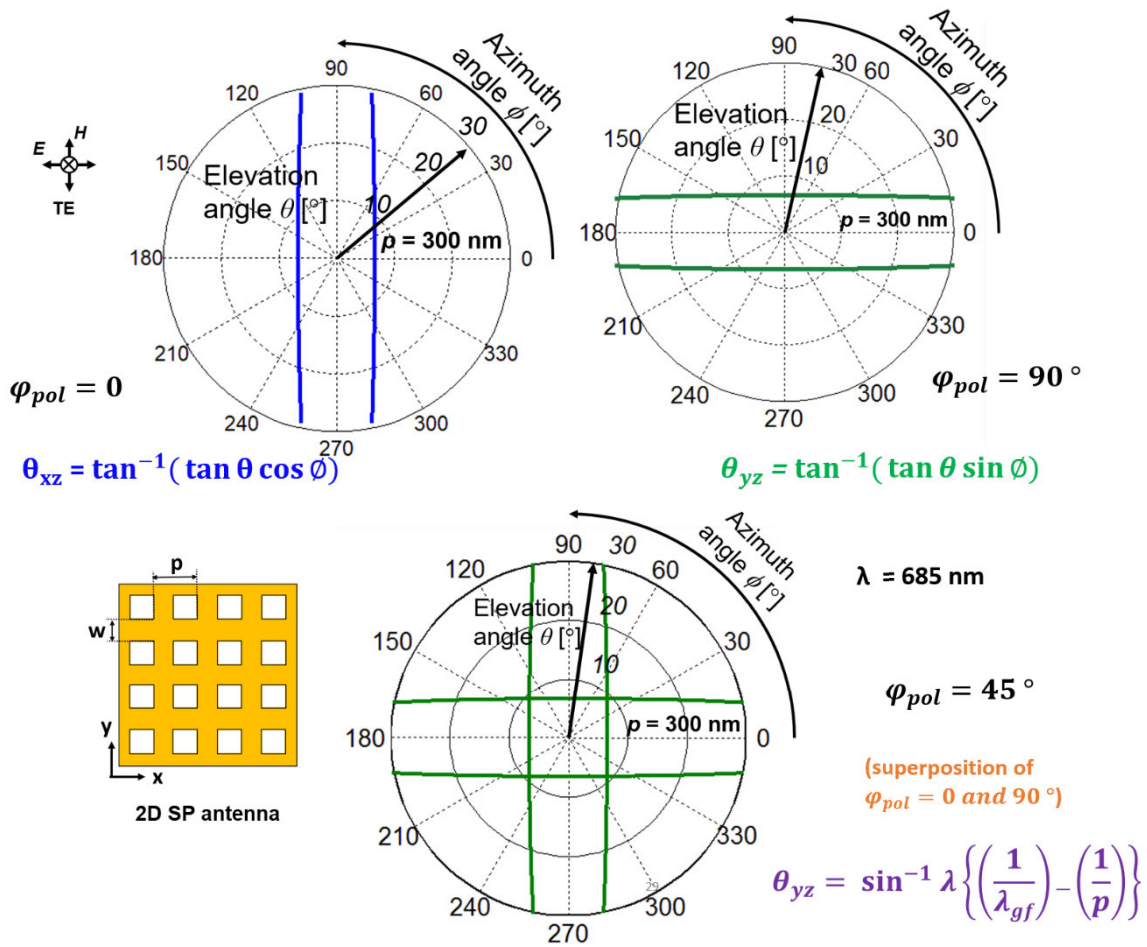


Fig.3.20. Theoretical spatial patterns with respect to the azimuth (ϕ) and elevation angles (θ) for $t_{SOI} = 100\text{nm}$, $\lambda = 685 \text{ nm}$ ($\lambda_g = 285.5 \text{ nm}$ (TM_0 mode)) and $p = 300 \text{ nm}$ for 2D hole array grating.

the spatial pattern for the SOI PD with 2D hole array grating with respect to its polarization. For pol 0, a two-fold symmetry along vertical direction due to the coupling of wave in xz direction occurs and pol 90° , a two-fold symmetry along horizontal direction due to the coupling of yz direction occurs. In the case of pol 45° a super position of polarization 0 and 90° occurs and results in a four-fold symmetry.

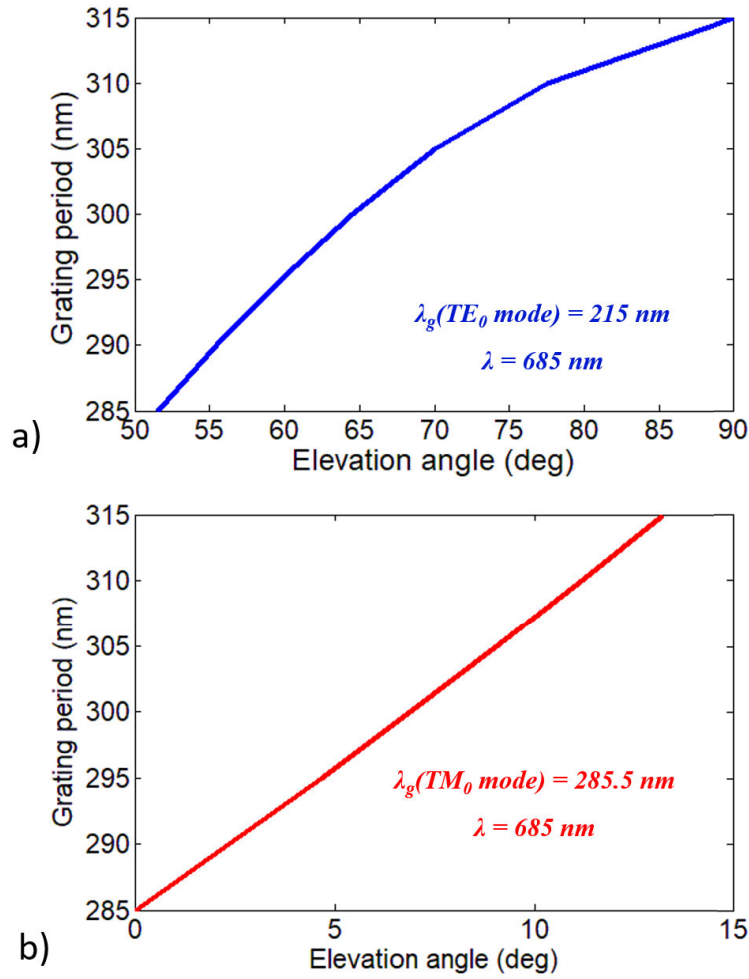


Fig.3.21. Elevation angle prediction for different grating periods, p at fixed incident wavelength, λ for a) TE_0 mode and b) TM_0 mode.

3.4.3 Effect of Propagation Modes

The peak elevation angle of our proposed device has significant dependence on the effect of the waveguide modes. As discussed earlier the PD is embedded on an SOI waveguide structure which supports propagation of both the TE and TM modes. The spectroscopic behaviour also ensured the high

quantum efficiency peaks corresponding to the fundamental modes of TE and TM in our previous studies and small peak with less quantum efficiency corresponds to TE_1 and TM_1 modes. From the dispersion curve we can calculate the propagation wavelengths corresponding to the incident wavelength, 685 nm as 215 nm for TE_0 mode and 285.5 nm for TM_0 mode. By using phase matching condition we can solve for peak elevation angle for both the fundamental waveguide modes, TE_0 and TM_0 as shown in Fig.3.21 a) and b), respectively. Although coupling of incident light with TE_1 and TM_1 modes in SOI slab also occurs we showed only for the fundamental modes. However, the peak corresponding to the TE_1 and TM_1 modes has less quantum efficiency.

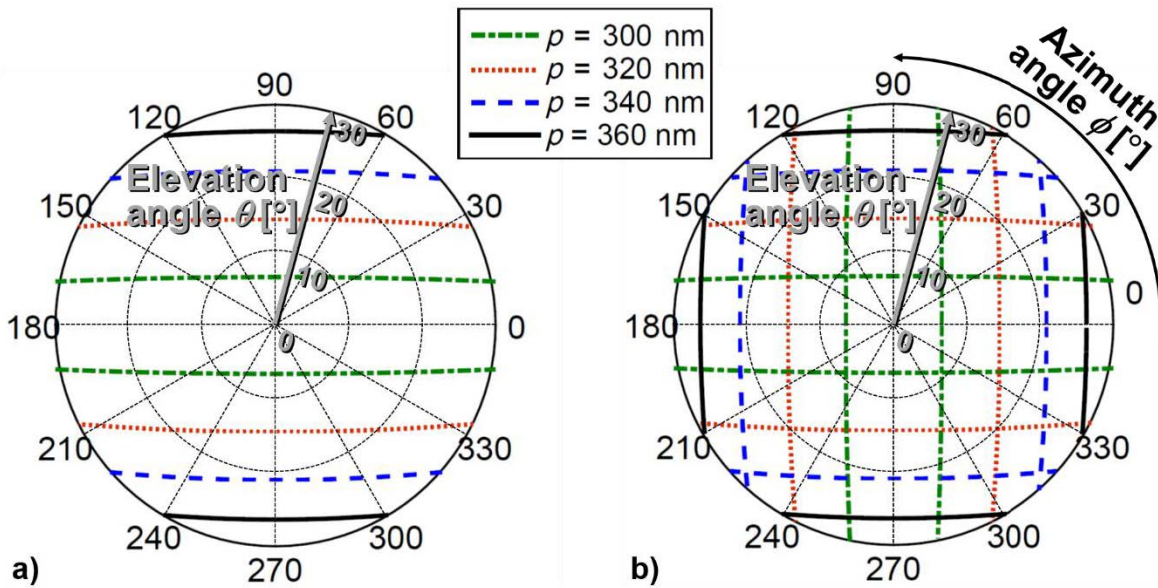


Fig.3.22. Theoretical spatial patterns with respect to the azimuth (ϕ) and elevation angles (θ) for $\lambda = 685$ nm, TM_0 mode ($\lambda_g = 285.5$ nm), $t_{SOI} = 100$ nm, and various p 's for forward waves, SOI PD with a) 1D L/S grating and b) 2D hole array grating.

3.4.4 Effect of Grating Period

The spatial pattern for SOI PD with 1D L/S grating and 2D hole array grating with $t_{SOI} = 100$ nm, $\lambda = 685$ nm, TM_0 mode ($\lambda_g = 285.5$ nm) for different grating period is calculated. The forward waves with $p > \lambda_g$ and backward waves with $p < \lambda_g$ for both the 1D and 2D grating is shown in Fig 3.22 a) and b) and Fig.3.23 a) and b) respectively. For the forward waves (Fig.3.22), the L/S and hole array shows two-fold and four-fold symmetry such that the patterns move away from the centre of origin as p increases. For the backward waves (Fig.3.23), the pattern of the L/S and hole array grating moves towards the center as the period increases. The shift in the pattern reveals that the 2D angular distribution could be tuned by the grating period.

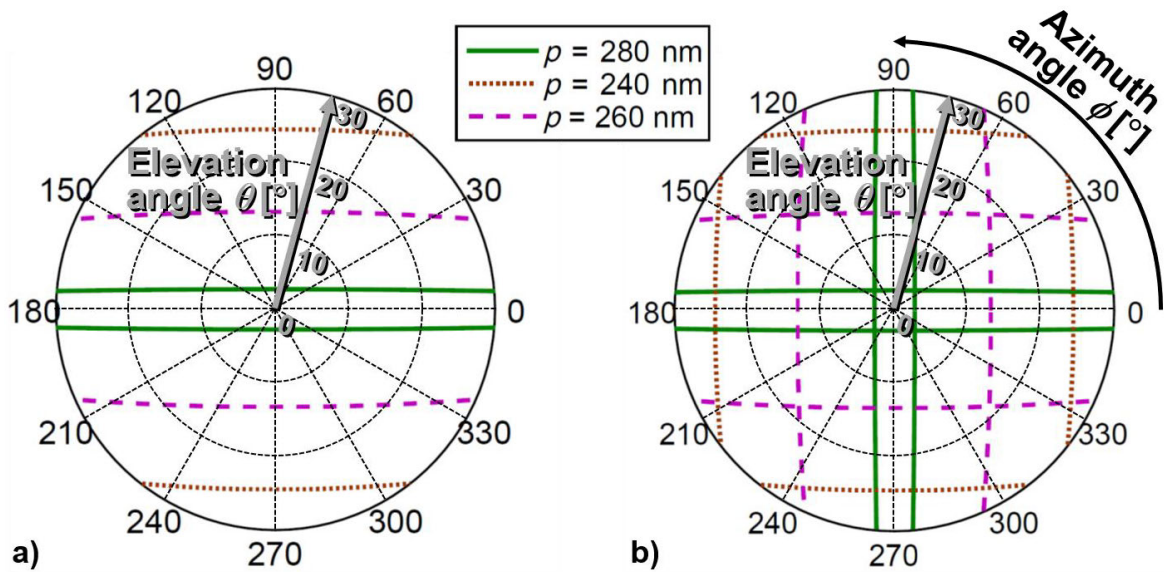


Fig.3.23. Theoretical spatial patterns with respect to the azimuth (ϕ) and elevation angles (θ) for $\lambda = 685$ nm, TM_0 mode ($\lambda_g = 285.5$ nm), $t_{SOI} = 100$ nm, and various p 's for backward waves, SOI PD with a) 1D L/S grating and b) 2D hole array grating.

3.5 Conclusion

In this chapter our novel device SOI PD with two types of grating, 1D L/S grating and 2D hole array grating SP antenna is proposed. The working principle of the device and the spectroscopic characteristics with wavelength, polarization and incidence angle selectivity is overviewed. The new feature of azimuth-elevation incident angle dependence is focused and discussed using theoretical estimation. A framework of mathematical equation is formalized for the theoretical prediction of the azimuth-elevation angular distribution. Using Matlab coding spatial pattern for 2D data representation is calculated. Thus, the theoretical modelling of the CMOS based pixel scale photodetector is done successfully and discussed in this chapter.

Chapter 4

SIMULATION AND MEASUREMENT RESULTS

This chapter involves the design of the proposed photodetector consists of SOI pn-junction photodiode with SP antenna (1D L/S grating and 2D hole array grating) for azimuth-elevation incident light angle dependence and evaluation of the same through electromagnetic simulation based on 3D FDTD (Finite Difference Time Domain) method for numerical prediction[82]. The numerically predicted azimuth-elevation angular distribution is clarified by the theoretical concept and further verified by the experimental demonstration of the fabricated devices.

4.1 Simulation Method and Conditions

4.1.1 Introduction of FDTD Method

The analysis of structures by Finite-Difference Time-Domain method is done by solving the differential form of Maxwell`s equations. They are widely used for the determination of electric and magnetic fields distribution, energy and power distributions of plasmonic and photonic structures such as slab waveguides, plasmonic gratings, nanoantenna, metallic nanorods, nanoparticles, sub-wavelength apertures and other opto-electronic devices for imaging, sensing, etc. The FDTD methods evaluate the structure based on discretization of the Maxwell`s equation in both time and space domains in order to calculate the electric and magnetic fields at different positions at different time-steps. This process of determination of the fields, E and H at different points in space and at different times, an FDTD algorithm called Yee`s algorithm is employed. According to this algorithm, each electric field component is surrounded by four magnetic field components and each magnetic field component is surrounded

by four electric field components. Our group has previously employed FDTD to calculate the absorption efficiency and field distribution of the device composed of SOI PD with SP antenna and successfully verified various characteristics of the device with the experimental demonstration. In this thesis, FDTD is employed to design an optimum device structure and to evaluate the performance of the device. Our aim to investigate the angle detection capability of our novel photodetector in two dimensions. 3D FDTD facilitates for the 2D tilting and rotation of the incident light and for determining the performance of the device in 3D volume. We use absorption efficiency as the metric to detect the incident light angle. The FDTD evaluation involves calculating the power absorbed in the silicon layer of the device relative to the input power. The FDTD evaluation is carried out to investigate the angular distribution with several characteristics. In our research, we utilized an FDTD software called FULLWAVE by R-Soft to carry out FDTD analysis of our novel devices, SOI PD with 1D and 2D grating SP antenna. This software has many advantages such as it enables FDTD analysis of the metallic structures to include the Lorentz and Drude models of dispersion relations of the complex permittivity of the metals. In our simulation we use Lorentz- and the Drude-type dispersions for expressing the complex permittivity of the Si and Au, respectively.

4.1.2 Designing of device

Our proposed novel device composed of photodiode (PD) formed on a SOI substrate with surface plasmon (SP) antenna stacked over it, is designed to obtain maximum absorption efficiency. We started the discussion by considering the SOI PD with 2D hole array grating as shown in Fig.4.1. The FDTD computation requires the numerical simulation parameters such as finite

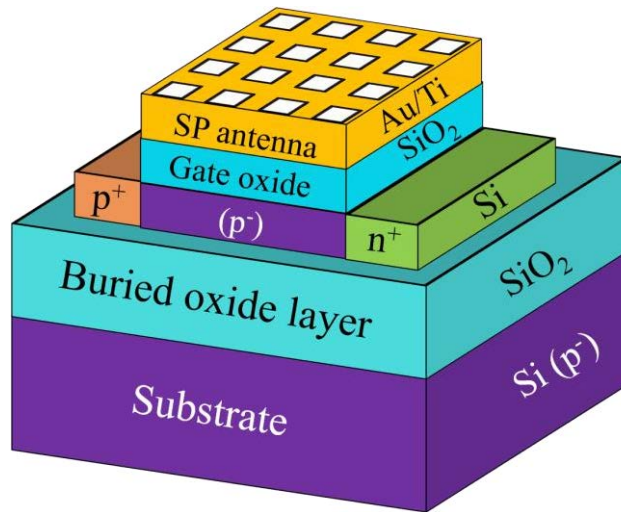


Fig.4.1 3D view of the SOI PD with 2D hole array grating SP antenna mounted over the gate region of the PD with an electrical isolation of SiO₂.

computation domain, boundary conditions, spatial grid sizes and temporal grid (time step and time stop criteria).

4.1.2.1 Computational Domain

Fig.4.2 shows the cross-sectional view of the SOI PD with 2D SP antenna and the definition of 2D unit periodic structure for computational domain indicated by red dotted region. This choice of computational domain includes the portion of device structure to be simulated. The FDTD simulation is done by FULLWAVE by solving the electromagnetic fields in a structure defined in this domain as a function of time in a finite spatial domain on a spatial grid. The structure is assumed to be periodically infinite in y direction.

4.1.2.2 Boundary Condition

The computational domain must be designed carefully by applying boundary conditions at the spatial edges of the unit periodic structure defined.

Generally, an absorbing boundary condition is applied to absorb the propagation energy that impinges on the boundary of the computational domain to eliminate any outward propagating energy out of the domain. The most effective boundary is the perfectly matched layer (PML), in which magnetic and electric conductivities are introduced so that the wave impedance remains constant, absorbing the energy without inducing reflecting of energy.

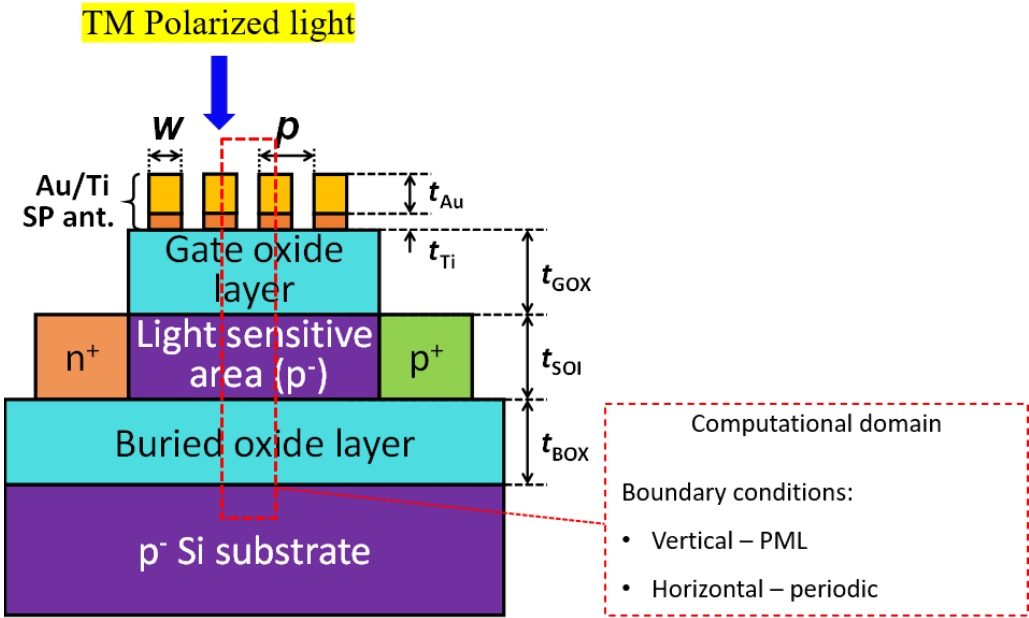


Fig.4.2 Cross-sectional view of the SOI PD with 2D SP antenna and 2D unit structure for computational domain. The structure is assumed to be periodically infinite in y direction by applying periodic boundary in horizontal direction. For vertical boundary PML is applied.

Other boundary conditions are periodic, symmetric, anti-symmetric, and PEC boundary conditions. A periodic boundary condition is also called as Bloch boundary which stipulates any electromagnetic field that leaves the boundary

on one end of the computational domain must reenter the domain on the opposite end. This can be given by mathematical expression as follows,

$$E(x_i) = E(x_i + \Delta) e^{tk_i x_i}$$

where the device structure is assumed to be periodic along x direction with phase difference k_i and period Δ (length of the domain along periodic direction, x).

In our simulation we apply PML boundary conditions at the top and bottom of the structure at the boundary of the domain to eliminate any outward propagation of energy from the domain. We apply periodic boundary in the horizontal, x and y direction. Because the hole array grating structure is 2D and periodic along both the x and y direction. Hence simulation is done by assuming the unit cell in 2D periodic directions (Fig.4.2).

4.1.2.3 Spatial grid

In Fullwave both a uniform and non-uniform spatial grid is supported. The specification of this grid is done as a combination of spatial grid sizes (in micrometer) or as 'points-per-wavelength' (PPW). The grid can be smoothly varied between the regions. As the spatial grid is designed smaller and smaller more accurate in the simulation is achieved and results in resolving the smallest feature of the field to be simulated. This is dictated by the wavelength in the structure to be analysed, and in some cases dictated by the geometry of the photonic structure. The grid spacing is usually less than wavelength/10 in order to resolve the wavelength in time. The grid size used in the simulation is $\Delta d = \Delta x = \Delta y = \Delta z = 5nm$.

4.1.2.4 Incident source

In FULLWAVE simulation the launch field, or excitation, is used to excite the structure within the computational domain. This incident excitation source must be chosen corresponding to the type of simulation results needed. A CW excitation is used for a steady-state analysis of a structure is required and a pulsed excitation is used when the spectral characteristics of a structure are needed.

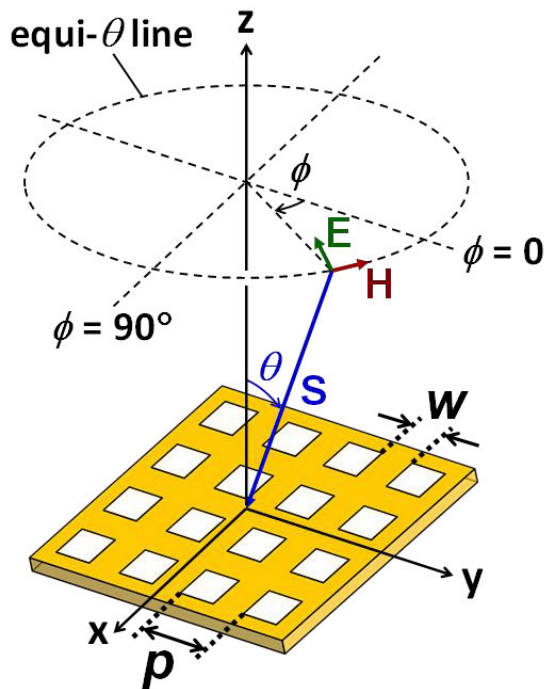


Fig.4.3 Bird's eye view of the SP antenna with 2D hole array grating with the definition of incident angle of light with elevation (θ) and azimuth (ϕ) angles. E , H and S are electric field, magnetic field and Poynting vector, respectively. The H is rotated parallel

In our simulation we excite the structure by placing the plane wave at the top of the structure. Fig.4.3a) shows the bird's eye view of the SP antenna with 2D hole array grating and b) is the definition of incident angle of light with elevation (θ) and azimuth (ϕ) angles. E , H and S are electric field, magnetic

field and Poynting vector, respectively. The H is rotated parallel to the equi- θ line and x-y plane.

4.1.2.5 Temporal Domain Settings

The two main temporal domain settings are the time step and stop criteria.

- **Time step:** For achieving a stable simulation, Courant condition must be adhered which relates the spatial and temporal step size as follows

$$c\Delta t < \frac{1}{\sqrt{\left(\frac{1}{\Delta x^2} + \frac{1}{\Delta y^2} + \frac{1}{\Delta z^2}\right)}}$$

where c is light speed in vacuum.

- **Stop criteria:** A stop time must be defined to stop the simulation run. The stop time must not be too short as it results in inaccurate results and long time also results in inefficient.

In our simulation we use a time step, $\Delta t = \Delta d/c = 1.66 \times 10^{-18}$ for 2D or 3D electromagnetic calculations.

4.1.2.6 Material Definition

In FULLWAVE, a variety of material types including linear, non-linear, dispersive, anisotropic, and magnetic materials are supported. In our simulation we use the following materials, vacuum, SiO₂, Si, Ti and Au. The vacuum and SiO₂ are designed by defining its relative permittivity as 1 and 2.13, respectively. For the materials, Si and Au the FDTD calculation is done by defining their complex permittivity which is expressed by the Lorentz and Drude dispersions, respectively. The complex relative permittivity of silicon is given by

$$\epsilon_r = \epsilon_\infty + \frac{(\epsilon_s - \epsilon_\infty)\omega_p^2}{\omega_p^2 + 2j\omega\delta_p - \omega^2}$$

where

ω_p , frequency of pole pair,

ϵ_∞ , relative permittivity at infinite frequency,

ϵ_s , zero-frequency or static relative permittivity,

δ_p , damping coefficient.

All these parameters are decided by fitting the experimental results provided by SOPRALAB for visible wavelength range. The complex relative permittivity of gold is,

$$\epsilon_r = \epsilon_\infty + \frac{\omega_p^2}{\omega^2 - j\omega\gamma_p}$$

where

ω_p , Drude pole frequency

γ_p , inverse of pole relaxation time

$\epsilon_\infty=1$, $\omega_p = 1.027 \times 10^{16}$ rad/s & $\gamma_p=2.83 \times 10^{14}$ rad/s.

4.1.2.7 Absorption efficiency

The external quantum efficiency is equivalent to the absorption efficiency and could be predicted by FDTD evaluation. The Absorption efficiency is calculated over the area of silicon by using absorption spatial output that records the power

absorbed as a function of space at specific times. The following expression is used to evaluate,

$$U_E(r', t_s) = \omega \text{Im}[\epsilon(r')] |E(r', t_s)|^2$$

where

E , electric field,

ϵ , spatially dependent index &

r' , spatial coordinate.

4.1.3 Optimization of Device

The goal of this work is to investigate the capability of the angle sensing behaviour of our device. In our device when the light at different angles are incident over it, the angle at which maximum light absorption occurs is considered as the peak angle. Therefore, quantum efficiency is used as the metric for angle detection. FDTD is used to numerically predict the quantum efficiency of our device before fabricating the device. In FDTD designing, we device structure is designed and optimized to absorb maximum light in the SOI layer. Let us consider the SOI PD with 2D hole array SP antenna initially and initiate the discussion. The incident light of monochromatic wavelength, 685 nm is tilted by the elevation angle, θ and rotated by the azimuth angle, ϕ with the magnetic field rotated along the equi- θ line and x-y plane. The FDTD parameters, such as the grid size, time step, wavelength, incident source, boundary condition, incident angle definition are summarized in Table 4.1.

For optimization of device, SOI PD with fixed grating thickness, $t_{Au/Ti} = 100/5$ nm, $t_{GOX} = 100$ nm, $t_{SOI} = 100$ nm and $t_{BOX} = 200$ nm and grating period,

Table 4.1 FDTD parameters for the designing of the simulation set-up.

Parameter	Value
<i>Grid size</i>	<i>5 nm</i>
<i>Time step</i>	<i>1.66×10^{-18}</i>
<i>Incident wavelength</i>	<i>685 nm</i>
<i>Launch type</i>	<i>Plane wave</i>
<i>Boundary condition (z)</i>	<i>PML</i>
<i>Boundary condition (x & y)</i>	<i>Periodic</i>
<i>Elevation angle (θ)</i>	<i>0 : 1 : 30</i>
<i>Polarization angle</i>	<i>ϕ</i>

$p = 300$ nm is considered. The width, w of the grating is varied when a light with perpendicular polarization is incident on it. The calculated absorption efficiency for different grating width is shown in the graph as follows (Fig.4.4). The graph clearly shows that the light absorption is enhanced at a specific incident angle which is called the peak angle. As the width is varied the intensity of the peak angle is also varied. The width at which a maximum absorption is achieved is $w = 90$ nm and the corresponding duty ratio is $w/p = 0.3$ which is the optimum width and width/period, respectively. The peak absorption efficiency in the case of $t_{Au} = 100$ nm is 0.06. We can still improve the efficiency by reducing the size of the grating thickness from 100 to 50 nm. For the device with same structural dimensions, absorption efficiency for the device with $t_{Au} =$

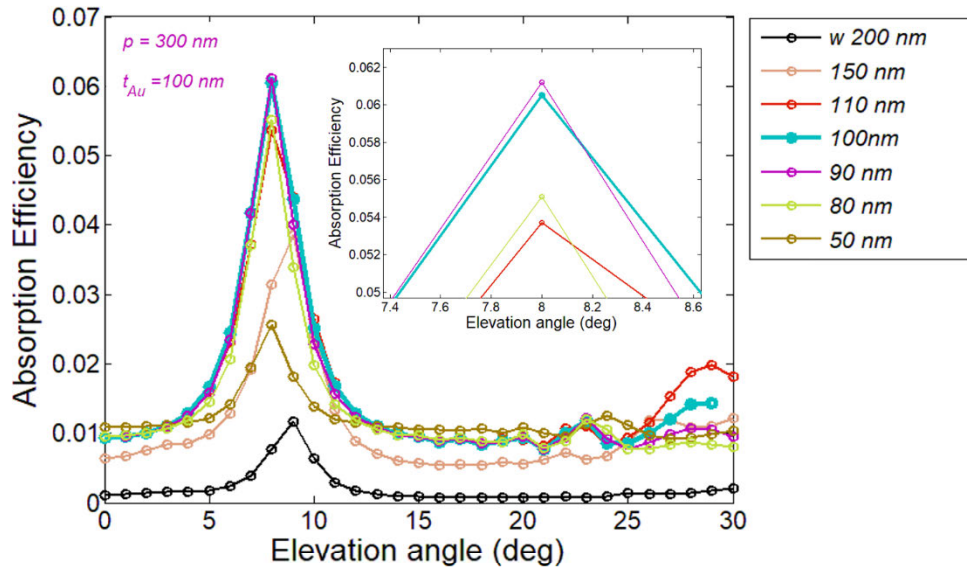


Fig.4.4 Absorption efficiency in SOI PD with 2D hole array of Au thickness 100 nm as a function of incidence angle θ calculated by FDTD. Grating width, w is varied while grating period, p is fixed at $p = 300$ nm.

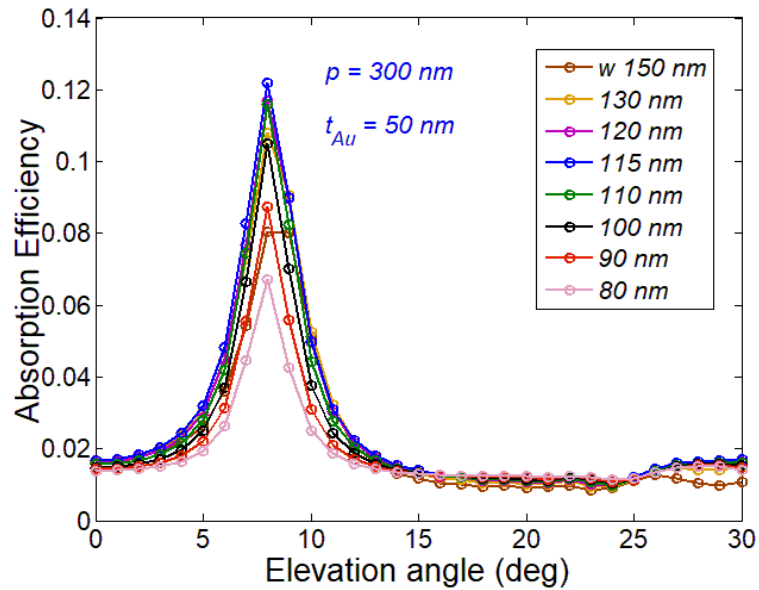


Fig.4.5 Absorption efficiency in SOI PD with 2D hole array of Au thickness 50 nm as a function of incidence angle θ calculated by FDTD. Grating width, w is varied while grating period, p is fixed at $p = 300$ nm.

50nm is calculated for different widths and shown in Fig. 4.5. The absorption efficiency increases as the width increases from 80 to 115 nm and then decreases from 120 to 150 nm. The absorption efficiency is much improved in the case of Au thickness of 50 nm. Therefore, the optimum width and w/p at which a maximum absorption is achieved is $w = 115$ nm and $w/p = 0.38$. The peak absorption efficiency in the case of $t_{Au} = 50$ nm is 0.12 and nearly two times greater than that of $t_{Au} = 100$ nm (0.06). Table 4.2 summarizes the optimum width and maximum efficiency of the SOI PD with 2D hole array SP antenna for these two cases.

Table 4.2 optimization of grating thickness (t_{Au})

Grating period, p (nm)	Grating thickness, t_{Au} (nm)	Optimum Width, w (nm)	Optimum Width, w/p (nm)	Peak quantum efficiency
300	100	90	0.3	0.06
	50	115	0.38	0.12

Now for the devices with different grating periods, $p = 260$ to 340 nm, with the optimum grating thickness, t_{Au} of 50nm, investigation on optimum width is done. The Table 4.3 summarizes the dimensions of the structural parameters of the device.

Next the optimization of width parameter is being done for the device with grating period, 320 nm. The absorption efficiency of the width ranging from 120 to 150 nm has been analyzed. The absorption efficiency is maximum (around 0.16) at $w = 125$ nm and then decreases as the width increases to 150 nm as shown in Fig.4.6. Hence the optimized w and w/p are found to be as 125 nm and 0.39.

Table 4.3 Structural parameter for the optimization of device

Layer thickness	Value (nm)
t_{Au}	50
t_{Ti}	5
t_{GOX}	100
t_{SOI}	100
t_{BOX}	200
p	Different fixed values (260 : 20 : 340)
w	vary

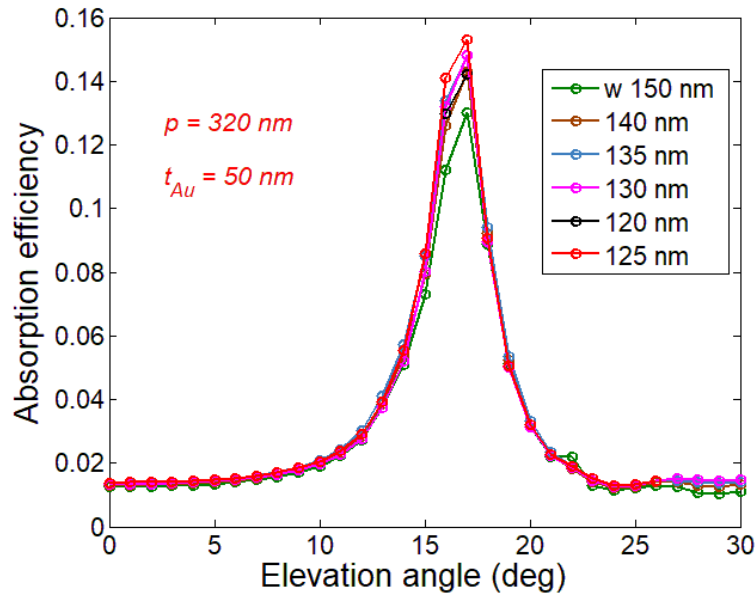


Fig.4.6 Absorption efficiency in SOI PD with 2D hole array of grating period, p is fixed at $p = 320 \text{ nm}$ and width, w is varied as a function of incidence angle θ calculated by FDTD.

The optimization of width for different grating periods, 340, 260 and 280 nm is calculated by FDTD simulation and summarized in table 4.4 with the corresponding predicted absorption efficiency.

Table 4.4 optimum width and absorption efficiency for various grating period, p

p (nm)	Optimum w	Optimum w/p	Absorption efficiency
260	130	0.5	0.055
280	125	0.44	0.14
300	115	0.38	0.12
320	125	0.39	0.158
340	135	0.39	0.136

4.1.4 Simulation Conditions for Angle detection

Fig. 4.7 and 4.8 show the incident light configuration for numerical analysis of azimuth-elevation (ϕ , θ) angle detection under different conditions. The arrival direction of the light is represented by azimuth (ϕ) and elevation (θ) angles. In the first condition shown in Fig. 4.7, the numerical prediction of absorption efficiency is calculated for the polarization of the light not fixed and the magnetic component, H being rotated parallel to the equi- θ line and x-y plane. This is due to that the experimental photocurrent is measured for an incident light with fixed incident and polarization angle with the device being rotated in azimuth (ϕ) and elevation (θ) directions. In the case of Fig. 4.8, the light with fixed polarizations are incident at different directions (ϕ and θ) and

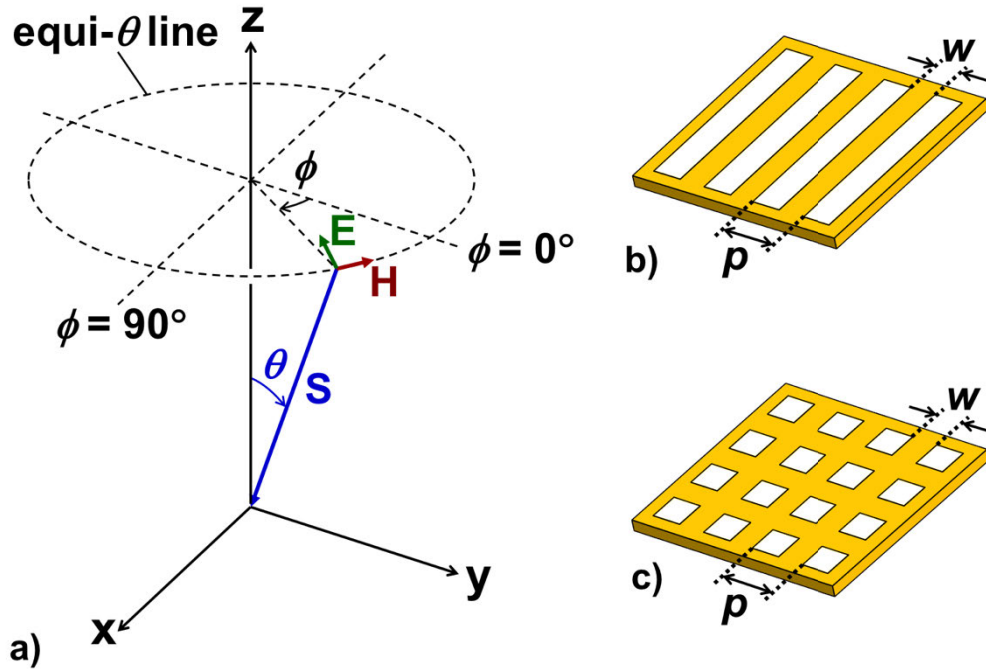


Fig.4.7 a) Definition of direction of the incoming light by azimuth and elevation (ϕ and θ) angles. The electric field, magnetic field and Poynting vector is denoted by E , H and S , respectively. Bird's eye view of the SP antenna with b) 1D L/S grating and c) 2D hole array grating.

θ_{xz} and θ_{yz} are the projections of the elevation (θ) angle on the x-z and y-z planes respectively, and the relation between θ and ϕ is formulated by using trigonometric rules as follows,

$$\theta_{xz} = \tan^{-1}(\tan \theta \cos \phi)$$

$$\theta_{yz} = \tan^{-1}(\tan \theta \sin \phi)$$

The polarization of the light is defined as ϕ_{pol} with respect to the grating direction. Fig. 4.7 and 4.8 b) and c) are the bird's view of the 1D L/S and 2D hole array grating, respectively.

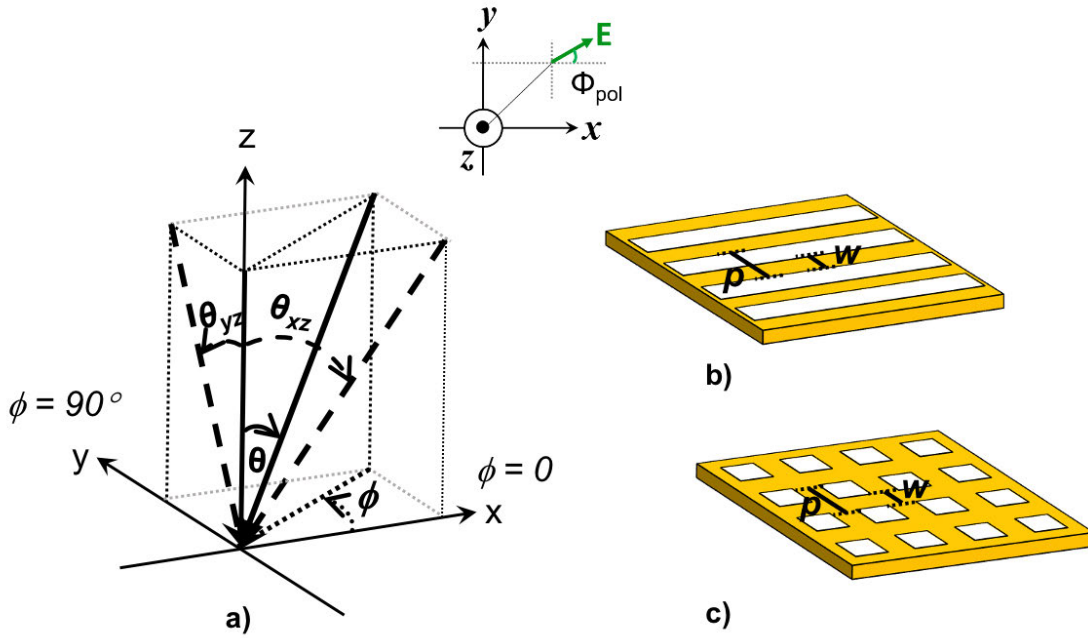


Fig.4.8 a) Definition of the incident angles, azimuth and elevation (ϕ and θ) and polarization (ϕ_{pol}) angles, projections of elevation angle, θ_{xz} and θ_{yz} , b) and c) 1D and 2D SP antenna, respectively.

4.2 Measurement Setup

The schematic of the measurement setup used for the experimental demonstration of our proposed device is shown in Fig. 4.9. The output photocurrent is measured by mounting the device in a small evaluation box and moved from its position to control the direction of light striking on its surface. An arrangement of stages attached to this evaluation box is used for this purpose. Three stages are used in this setup namely, XY stage for controlling the movement along x and y direction to position the beam at center, goniometer for tilting the elevation (θ) angle and rotational stage for controlling the azimuth (ϕ) angle. This setup is similar to the incident light configuration shown in Fig. 4.7 simulation condition where device is fixed, and light is moved. In order to

realize the simulation condition shown in Fig. 4.8 the measurement setup needs to be modified. Now the system consists of four stages, XY stage, rotational stage and two kinds of goniometer stages, one controls the tilting along x direction (θ_{xz}) and another controls in y (θ_{yz}) direction. In this case the laser is polarized to the desired polarization (ϕ_{pol}) angle and illuminated on the device. In addition to the development of this setup, an Excel/VBA program is developed to measure the photocurrent with a semiconductor parameter analyzer by controlling the device stages at different azimuth and elevation angles.

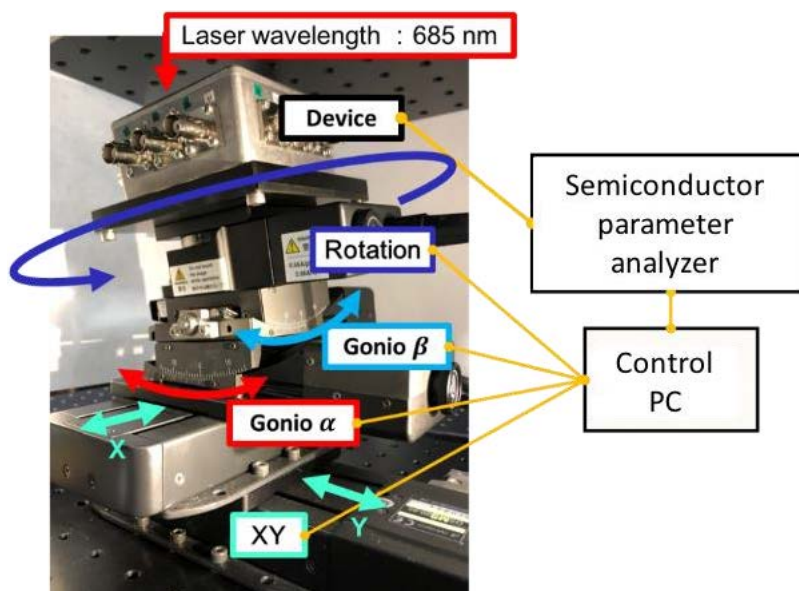


Fig.4.9 Schematic of the measurement setup with device fixed in a evaluation box supported by different stages and controlled by the external PC and semiconductor analyzer.

Fig. 4.10 shows the schematic of the complete optical set up for the measurement of output photocurrent. The incident source is a monochromatic laser light of wavelength, 685 nm. Next to the laser source is a mirror to reflect

the light in the optical device, half-wave plate to shift the polarization state of the incident light. Then the light is passed through the laser beam expander to expand the beam size. Finally, the light is incident on the normal axis of the evaluation box at the center of which the device is mounted. In Fig.4.10 a) the

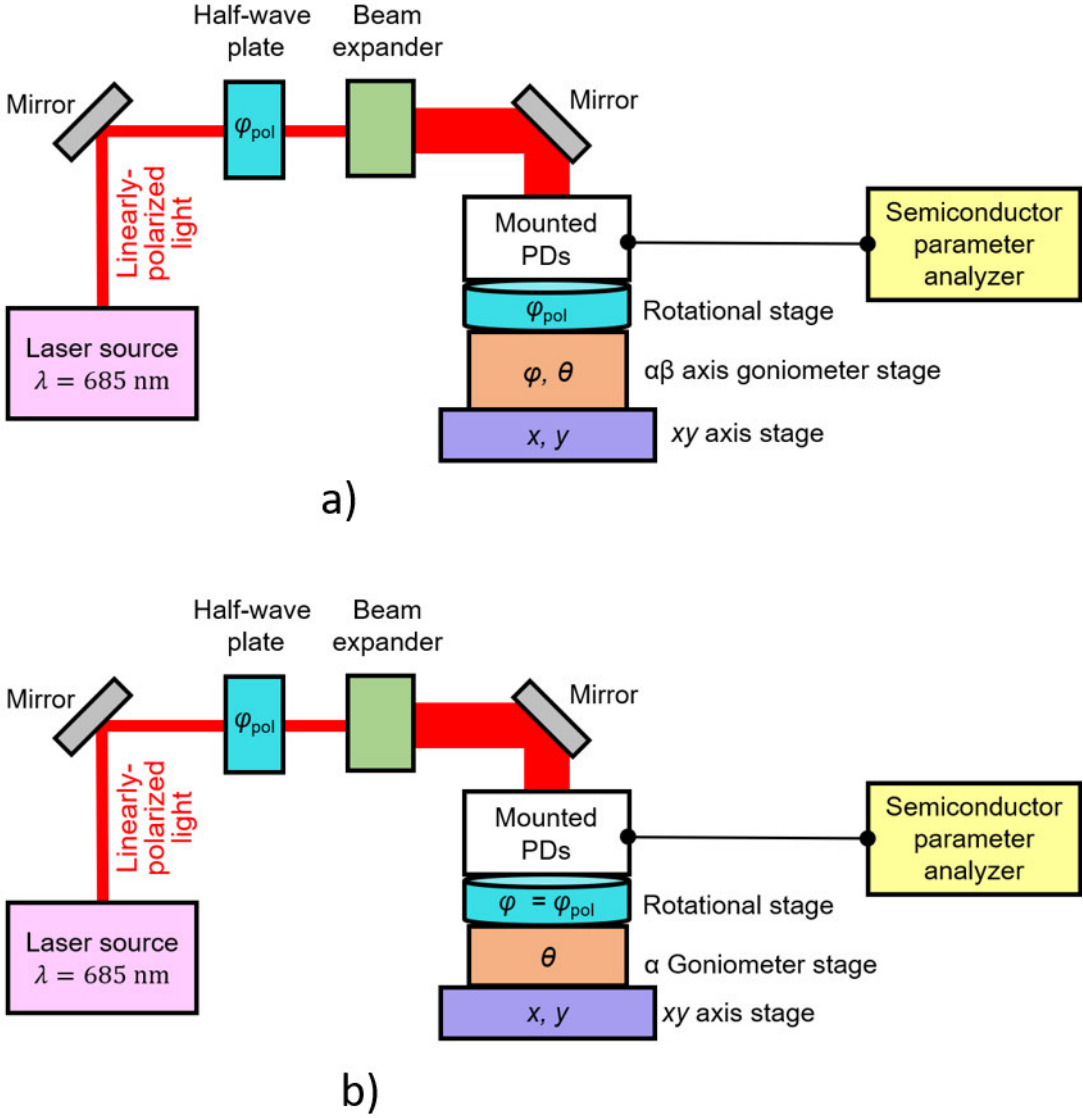


Fig.4.10 Schematic of the full optical setup for device measurement for the conditions a) $\phi = \phi_{pol}$ and b) ϕ_{pol} is fixed.

rotational and XY stages are employed for fixing the device position and the azimuth and elevation tilting is achieved by controlling the $\alpha\beta$ goniometer stage. Thus, in this case, for a fixed polarization of light, azimuth-elevation angle measurement is carried out. In Fig.4.10 b) the rotational stage is used to control the azimuth angle and the α goniometer stage is used to control the elevation angle. Thus, this setup facilitates the measurement of the device when the polarization is rotated equal to the azimuth angle.

4.3 Results of 1D L/S antenna

In this section the quantum efficiency is calculated by FDTD simulation and by the measured output photocurrent through the experimental demonstration of the SOI PD with 1D L/S antenna. FDTD simulation predicts the quantum efficiency by calculating the ratio of the power absorbed in the Si layer to the incident power assuming that all the photogenerated carriers in the SOI layer contributes to the photocurrent. In experimental demonstration, the output photocurrent (I_{ph}) of the device is measured and the external quantum efficiency (η) is calculated by the following equation,

$$\eta = \left(\frac{I_{ph}}{q}\right) \cdot \left(\frac{P}{h\nu}\right)^{-1} \cdot \left(\frac{1}{\cos\theta}\right)$$

where q is the elementary charge (1.602×10^{-19} C), P is the incident power (W), λ is the wavelength, h is the Planck's constant (6.626×10^{-34} [Js]), ν is the frequency of the incident light, and θ is the elevation angle.

4.3.1 Elevation (θ) angle dependence

The characterization of the 1D L/S grating for elevation angle dependence at fixed azimuth and polarization angle is shown by FDTD

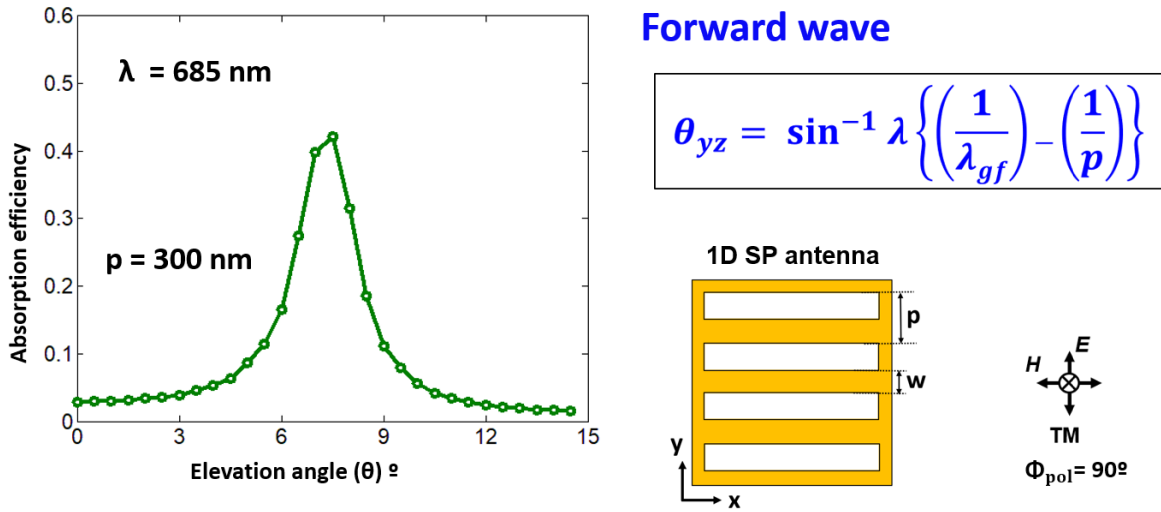


Fig.4.11 FDTD calculated elevation angle dependence of the device, SOI PD with 1D L/S grating for grating period, $p = 300 \text{ nm}$.

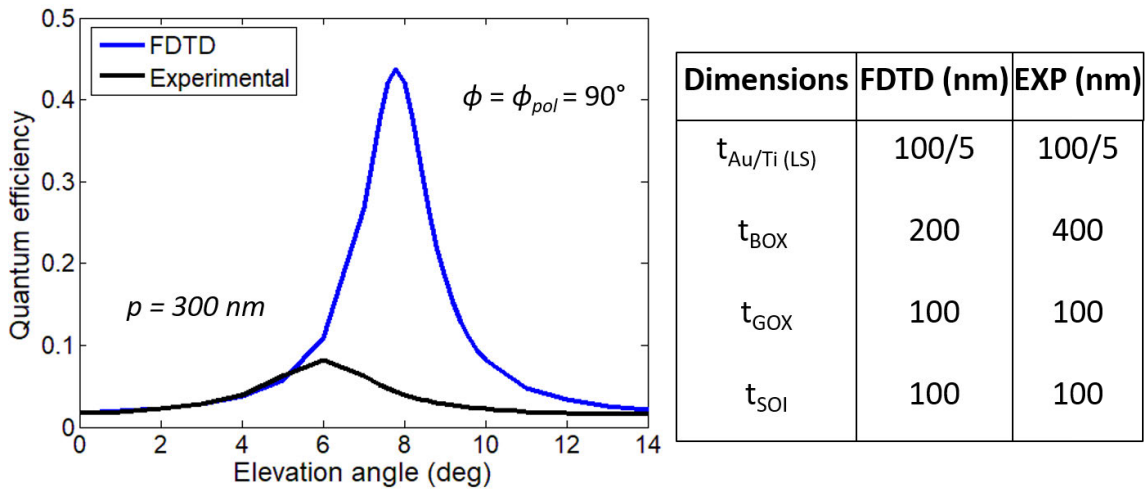


Fig.4.12 Comparison of numerical prediction and experimental verification for the SOI PD with 2D hole array grating with period, $p = 300 \text{ nm}$ at $\phi = \phi_{pol} = 90^\circ$.

calculation, experimental demonstration, and theoretical comparison. The structure of the device is designed with the dimensions $t_{GOX} = 100$ nm, $t_{SOI} = 100$ nm, $t_{BOX} = 200$ nm for FDTD and experimental have the same structural dimensions except for the $t_{BOX} = 400$ nm. The theoretical calculation is done by considering the SOI slab waveguide with Si core of 100 nm and claddings of infinite thickness for finding the propagation wavelength, λ_g as 285.5 nm and phase matching condition equation for finding the peak angle. Fig. 4.11 shows the absorption efficiency calculated by the FDTD method for a L/S grating device of grating period, $p = 300$ nm with $w/p = 0.5$ as a function of the elevation angle by considering the unit periodic structure. The incident light is perpendicular to the direction of the grating i.e. TM polarized incident light of wavelength, 685 nm is tilted along the elevation angle in perpendicular direction of the grating i.e $\phi = \phi_{pol} = 90^\circ$. The graph shows a Gaussian peak due to the coupling of the diffracted light from the grating and the forward propagation wave. In Fig. 4.12 the quantum efficiency of experimental demonstration of the device with $p = 300$ nm is shown and compared with the FDTD quantum efficiency with the same dimensions except for the box thickness which is shown in the table in Fig.4.12. The peak angle obtained in the experiment is nearly matching with the FDTD with a deviation of less than 0.6° . This may be due to some small changes in the fabricated SOI thickness of around 1 nm.

Fig. 4.13a shows the absorption efficiency calculated for various L/S devices of different grating periods, p and fixed $w/p = 0.5$ of range 285 to 340 nm at the steps of 5nm as a function of the elevation angle at the step size of 1 nm. For each device, a sharp peak emerges at different angles corresponding to the period. These peaks correspond to the maximum absorption efficiency due

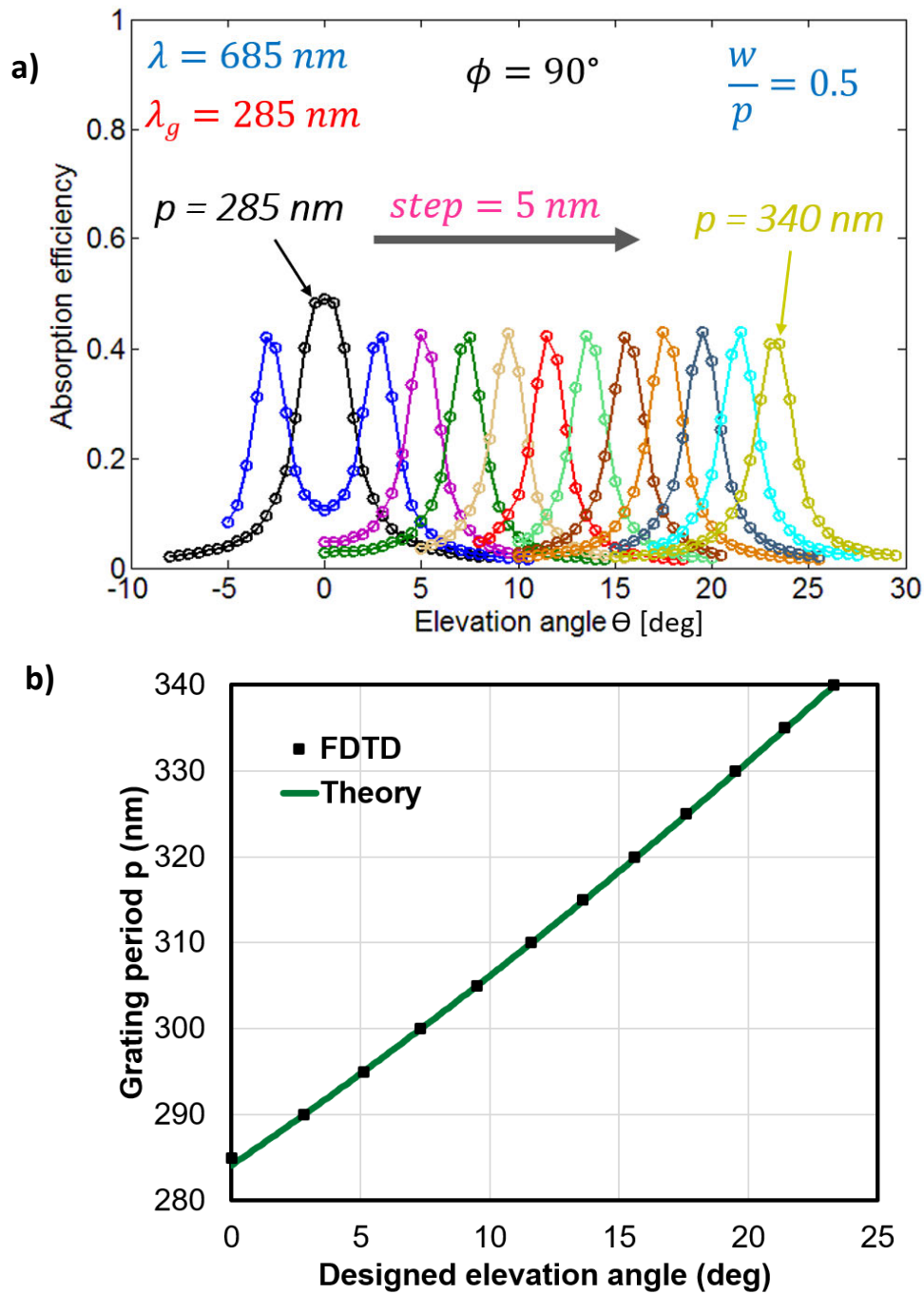


Fig.4.13 a) FDTD calculated elevation angle dependence and b) comparison of theoretical peak angle predicted by phase matching of the device, SOI PD with 1D L/S grating for different grating periods.

to strong coupling of the incident light with the lateral light propagation at specific incident angle which depends on the grating period. Thus, the graph shows clearly that the 12 different devices analyzed exhibits 12 different peak angles with a uniform absorption efficiency and the peak width except in the case of $p = 285$ nm. This is due to the matching of propagation wavelength (285.5 nm) and the grating period and this effect is discussed in detail in the previous chapter. The peak angle could be predicted theoretically by using equations of phase matching conditions.

The peak angle of the device for the coupling of incident wavelength (685 nm) with the TM_0 mode of the propagation wavelength in a SOI slab is calculated theoretically for different grating periods. Fig.4.13b shows the

Table 4.5 Summary of the dimension devices under different investigation conditions.

Dimension (nm)		I. $\varphi = \varphi_{pol}$				II. φ_{pol} fixed	
		FDTD		EXP		EXP	
		HA	LS	HA	LS	HA	LS
$t_{Au/Ti}$		50/5	100/5	100/5	100/5	50/5	50/5
t_{GOX}		100	100	100	100	100	100
t_{SOI}		100	100	100	100	105	105
t_{BOX}		200	200	400	400	400	400
w/p	$p = 260$	0.38	0.5			0.32 ($p=286$)	0.51 ($p=286$)
	280	0.39	0.5				
	300	0.38	0.5	0.33	0.55		
	320	0.39	0.5				
	340	0.39	0.5				

comparison of the theoretical peak angle predicted by phase matching condition with the peak angle calculated by FDTD prediction for different grating devices. The peak angles predicted by the FDTD calculation follows the same trend with the theory and the peak angles are in agreement with each other. The Table 4.5 shows the summary of the dimension devices under different investigation conditions for the FDTD and experimental conditions of the two cases 1. $\phi = \phi_{pol}$ and 2. ϕ_{pol} is fixed.

4.3.2 Azimuth-Elevation (ϕ and θ) angle dependence

The investigation on the elevation angle dependence shows the capability of incident angle detection by the device and in fact distinct angles by different grating periods. However, this investigation is based on azimuth angle fixed at perpendicular direction of the grating. In real time we need to discriminate the incident light whether it strikes the sensor at left or right side of the device. So, it is important to analyse the azimuth and elevation dependence of the device. For the incident light configuration shown in Fig. 4.7, i.e. $\phi = \phi_{pol}$ (the polarization component is rotated with the azimuth angle) the azimuth-elevation angle is investigated for the device with grating period, $p = 300$ nm and shown in Fig. 4.14. The gaussian peak with high intensity is obtained for perpendicular direction. As the azimuth angle decreases the light absorption is also decreases and finally reaches almost zero for the case of parallel direction. Fig. 4.15 shows the azimuth-elevation angle dependence for the effect of periods for the range of 280 to 340 nm at the steps of 20 nm. The angular distribution of the quantum efficiency with respect to the ϕ and θ is represented

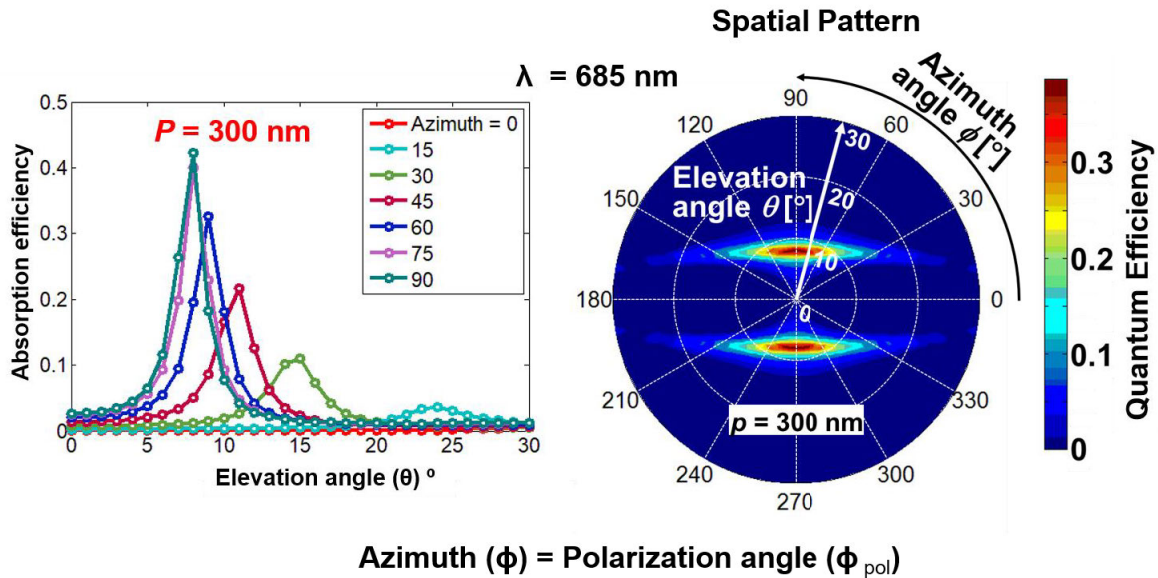


Fig.4.14 The gaussian peak distribution and the corresponding spatial patterns of quantum efficiency with respect to the azimuth and elevation angles for SOI PD with 1D L/S grating, $t_{SOI} = 100$ nm and $p = 300$ nm.

in the form of spatial pattern as shown in Fig.4.14. The contour of the map is indicated by the red and blue color region at high and low quantum efficiency, respectively. The theoretical estimation in the previous chapter has to be verified and therefore, theoretical spatial pattern for the devices analysed by simulation is shown in the Fig.4.15. The FDTD reproduces the theoretical calculation in that the spatial pattern exhibits contour with two gentle arcs with two-fold symmetry. The propagation wavelength is 285.5 nm for the incident light, 685 nm with SOI slab thickness of 100 nm. The symmetrical pattern of the quantum efficiency moves away from the center position as the size of p increases ($p = 280$ to 340 nm) for the case of forward waves ($\lambda_g < p$) and moves towards the center position for backward waves ($p < \lambda_g$). In the case of forward

and backward waves, the peak angles of the quantum efficiency are $\sim 1^\circ$ greater and lesser than the theoretical values, respectively. This could be explained by

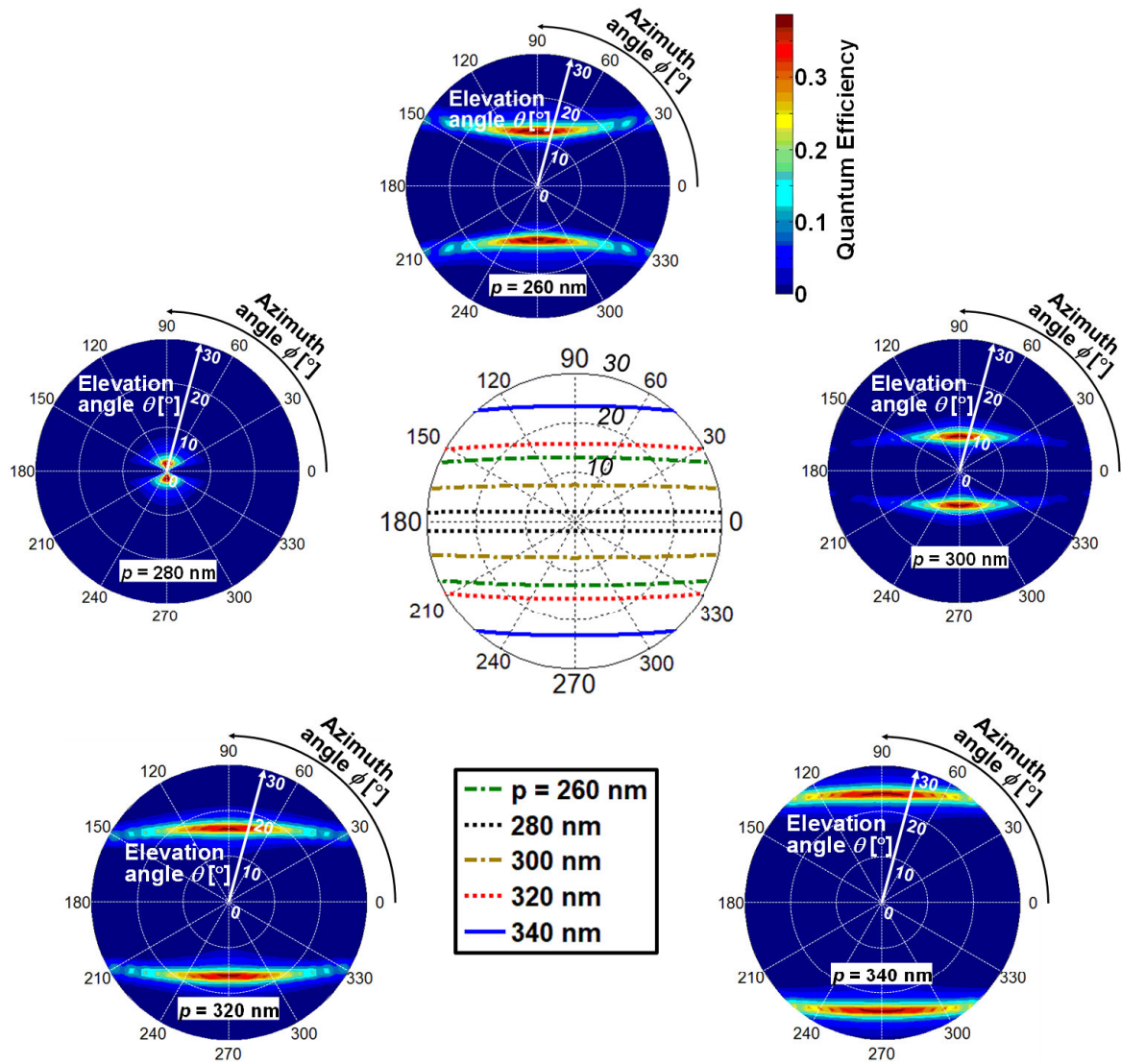


Fig.4.15 FDTD spatial patterns of quantum efficiency with respect to the azimuth and elevation angles for SOI PD with 1D L/S grating, $t_{\text{SOI}} = 100 \text{ nm}$ with different p and the corresponding theoretical spatial patterns.

the waveguide modes in the SOI slab, where the propagation wavelength is shortened from its original value of 285.5 to around 283 nm due to the finite thickness of the cladding layers in the FDTD simulation. The peak quantum efficiency is highly enhanced and reaches around 40%. This is due to the lateral propagation light wave in the SOI layer of our device, which acts as the important feature as an angle selective PD.

Fig.4.16 a) shows the top view of the fabricated SOI PD with 1D L/S SP antenna with optical micrograph of the PD and the scanning-electron

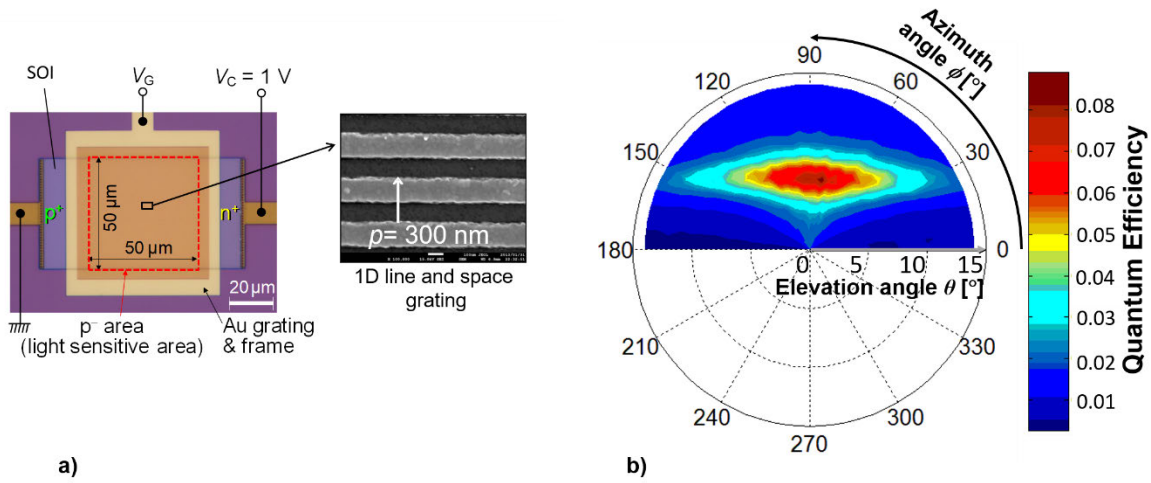


Fig.4.16 a) Top views of the fabricated SOI PD with SP antenna. Optical micrograph of the PD, scanning-electron micrographs of 1D L/S grating b) Experimental spatial patterns of quantum efficiency with respect to the azimuth and elevation angles for SOI PD with 1D L/S grating, $t_{SOI} = 100$ nm with period, $p = 300$ nm. ($\phi = \phi_{pol} = 90^\circ$).

micrographs of the 1D L/S grating with $p = 300$ nm. The spatial pattern of the external quantum efficiency with respect to the azimuth angle range of 0 to 180° and elevation angle range of 0 to 14° for the device with $p = 300$ nm and SOI thickness as same as the FDTD and theory ($t_{SOI} = 100$ nm) and $t_{BOX} = 400$ nm.

The quantum efficiency is measured by fixing the laser source and rotating the azimuth and tilting the gonio stage for ϕ and θ dependence. The measured spatial pattern reproduces the simulated spatial pattern very well. However, the quantum efficiency of the fabricated device is smaller when compared to the FDTD prediction (FDTD = 0.42 and EXP = 0.081). An abnormal substrate/gate bias dependence is found out in this case due to the presence of fixed oxide and/or trapped charges and therefore QE could not be maximized. Otherwise, higher QE (~45%) is routinely obtained which will be shown in other experimental data in Fig.4.18 and 4.19. This could be increased by improving the integrity of structure and the optical properties of the material.

4.3.3 Polarization (ϕ_{pol}) angle dependence

The analysis of the directivity in terms of elevation and azimuth angle have been investigated by theoretical prediction of peak angles, numerical prediction of quantum efficiency and peak angle verification and finally by experimental demonstration when the magnetic field of the light is rotated along the azimuth angle of the incident light. In nature light is made up of a collection of polarized rays. Hence, we further explore in detail about the capturing of azimuth-elevation incidence angle with the polarized incident light. For SOI PD with 1D SP antenna of period, 300 nm azimuth-elevation angle dependence is calculated by FDTD simulation for the angle range of $\phi = 0$ to 360° and $\theta = 0$ to 10° . Fig.4.17 shows the FDTD spatial pattern of $p = 300$ nm at $\phi_{pol} = 90^\circ$, when (a) the polarization component is rotated along the azimuth angle and (b) the polarization angle is fixed. The shape of the pattern in first case is like a gentle arc whereas in the second case the pattern is a line. In both cases the pattern

formation is occurs at almost same angle range especially, at $\phi = 90^\circ$, both have same peak position. The peak angle of FDTD has good agreement with the theory with a minimum angle deviation of around 0.5° . The predicted quantum efficiency is 45% which is due to the lateral light propagation.

For SOI PD with 1D SP antenna, with fixed grating period, $p = 270$ and 286 nm and SOI thickness, $t_{SOI} = 105$ nm, the polarization dependence of the azimuth-elevation angle is analyzed experimentally. We measured the output

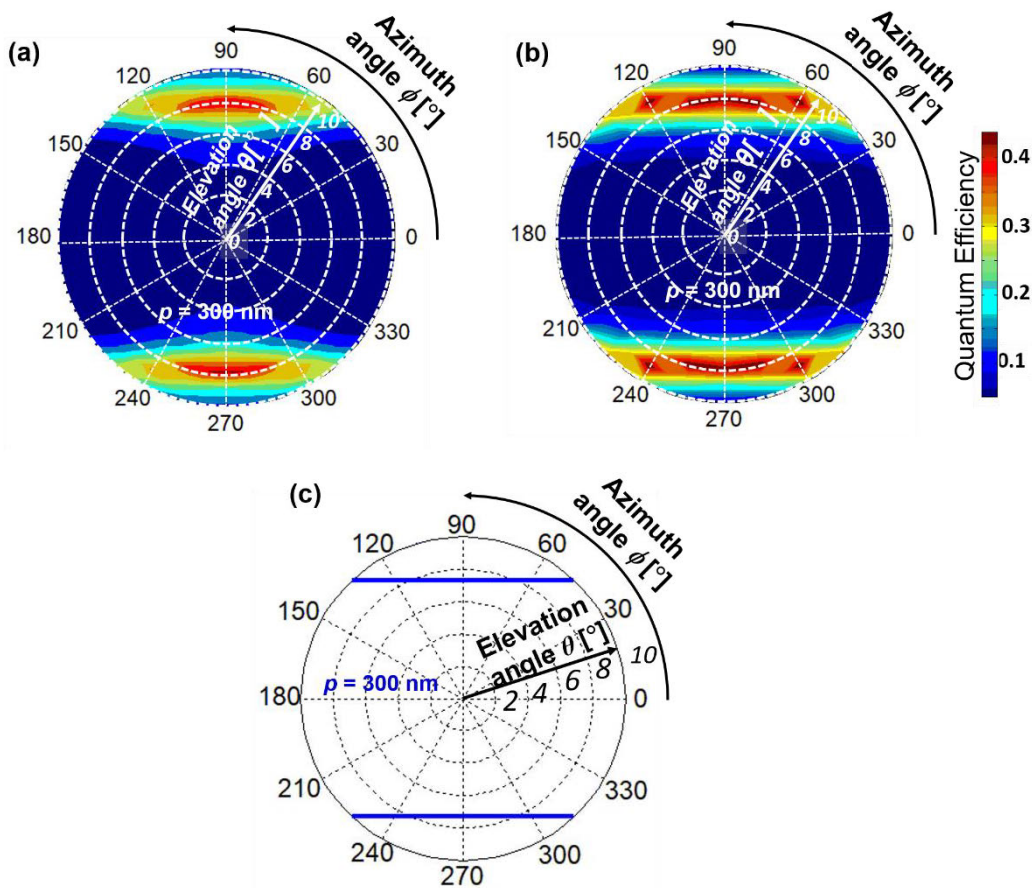


Fig.4.17 FDTD spatial patterns of predicted quantum efficiency of SOI PD with L/S of $p = 300$ nm, $\phi_{pol} = 90^\circ$ for (a) rotated ($\phi_{pol} = \phi$)polarization and (b) fixed polarization and (c) theoretical spatial pattern of $p = 300$ nm.

photocurrent of the photodiode at different polarization angle, $\phi_{pol} = i) 0, ii) 45^\circ$ and iii) 90° by illuminating with a monochromatic incident laser source and calculated the external quantum efficiency to plot the spatial pattern in polar coordinates with azimuth and elevation angle as polar and radial axes as shown in Fig. 4.18 and Fig.4.19 and compared with the theoretical estimation. The elevation angle range measured and studied are 0 to 8° and for azimuth angle of full rotation is analyzed (0 to 360°). A pair of gentle lines with two-fold

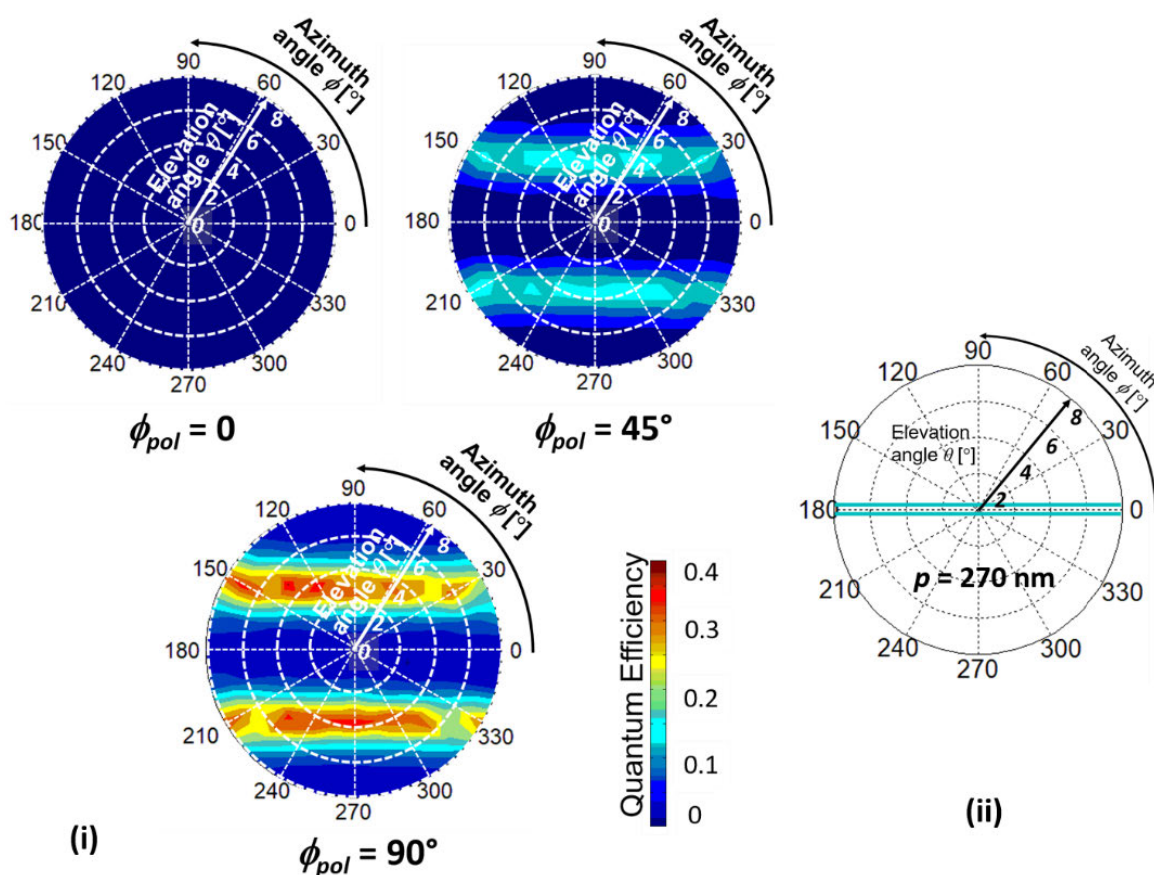


Fig.4.18 (i) Experimental spatial patterns of quantum efficiency with respect to the azimuth and elevation angles for SOI PD with 1D L/S grating, $t_{SOI} = 105 \text{ nm}$ with period, $p = 270 \text{ nm}$ for polarizations, $\phi_{pol} = 0, 45^\circ$ and 90° and (ii) theoretical spatial pattern for $p = 270 \text{ nm}$.

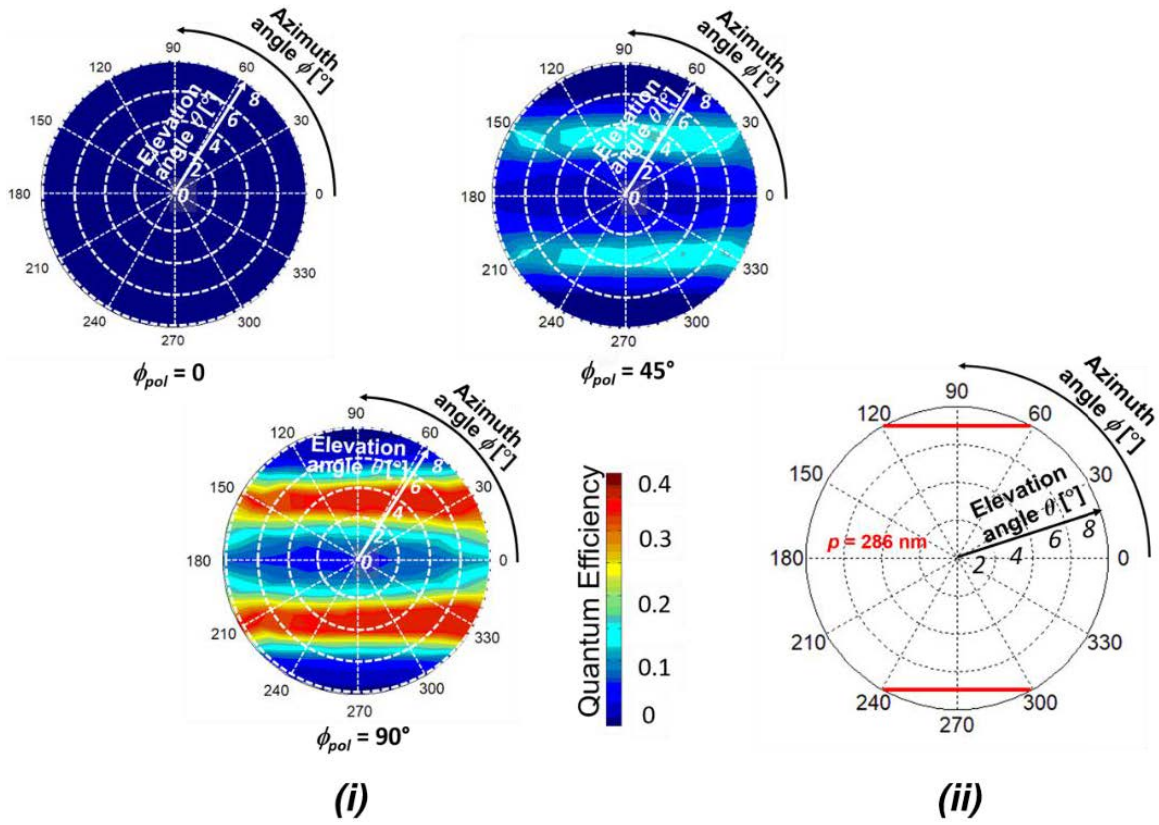


Fig.4.19 (i) Experimental spatial patterns of quantum efficiency with respect to the azimuth and elevation angles for SOI PD with 1D L/S grating, $t_{SOI} = 105 \text{ nm}$ with period, $p = 286 \text{ nm}$ for polarizations, $\phi_{pol} = 0, 45^\circ$ and 90° and (ii) theoretical spatial pattern for $p = 286 \text{ nm}$.

symmetry as obtained in spatial pattern of previous cases is obtained. The three spatial pattern shows the variation in the contour of the two-fold arcs. In the case of $\phi_{pol} = 90^\circ$, a maximum external quantum efficiency is seen and as the polarization angle is reduced to 45° , the quantum efficiency decreases below half of the former condition. In the case of $\phi_{pol} = 0$, a two-fold symmetry is very hard to find out since the generation of photocurrent is very low under this condition. This is because for $\phi_{pol} = 0$, the incident light is TE wave, so the coupling occurs between the incident TE polarized wave and TE waveguide

mode propagating in the SOI slab. But the phase matching occurs above the elevation angle under this study. For the case of $\phi_{pol} = 90^\circ$, the incident TM polarized wave couples with the fundamental TM waveguide mode and produces maximum external quantum efficiency of 46% and 40% for device with $p = 270$ and 286 nm, respectively. The theoretical pattern shows the agreement with experimental results with a deviation of around 3° .

4.4 Results of 2D hole array antenna

The incident angle detection of the SOI PD with 2D hole array SP antenna by numerical prediction by FDTD method and experimental demonstration is discussed in this section.

4.4.1 Elevation (θ) angle dependence

In Fig.4.20, the quantum efficiency of experimental demonstration of the device with $p = 300$ nm is shown and compared with the FDTD quantum efficiency with the same dimensions except for the box thickness which is shown in the table in Fig. 4.20. The peak angle obtained in the experiment and FDTD are 8.6° and 8° respectively which is 1.3° and 0.7° less than the theoretical peak angle. The peak quantum efficiency is smaller when compared to the FDTD prediction (FDTD = 0.12 and EXP = 0.00028). This could be increased by improving the integrity of structure and the optical properties of the material. The quantum efficiency of the 1D L/S (0.42) is greater than the 2D hole array (0.12).

4.4.2 Azimuth-Elevation (ϕ and θ) angle dependence

The investigation of incidence angle of the SOI PD with 2D SP antenna is further explored by analyzing the azimuth-elevation angle dependence. For the incident light configuration shown in Fig. 4.7, i.e. $\phi = \phi_{pol}$ (the polarization

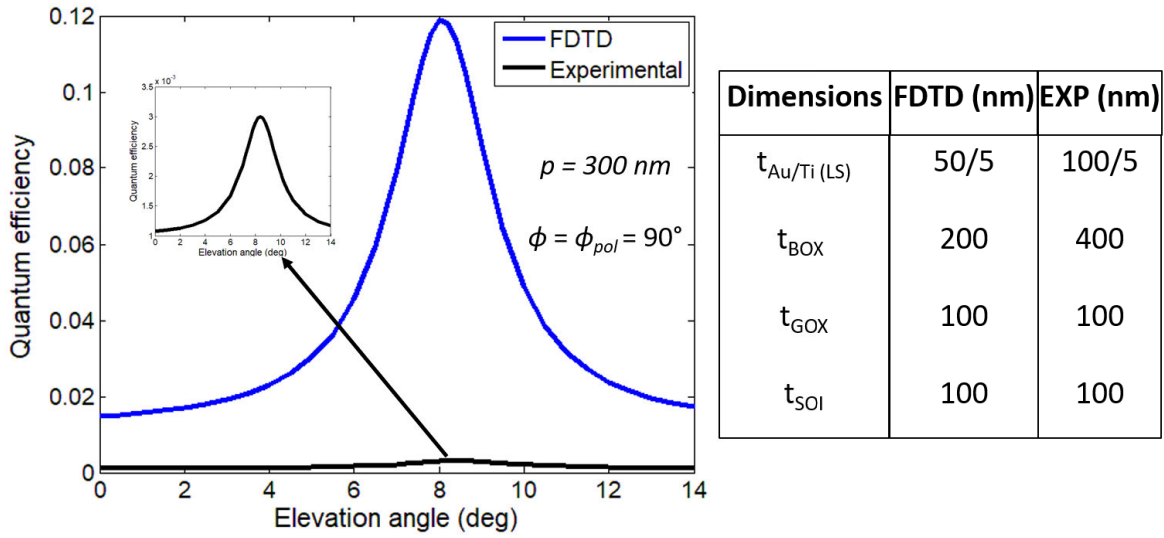


Fig.4.20 Comparison of numerical prediction and experimental verification for SOI PD with 2D hole array grating with, $p = 300 \text{ nm}$ at $\phi = \phi_{\text{pol}} = 90^\circ$.

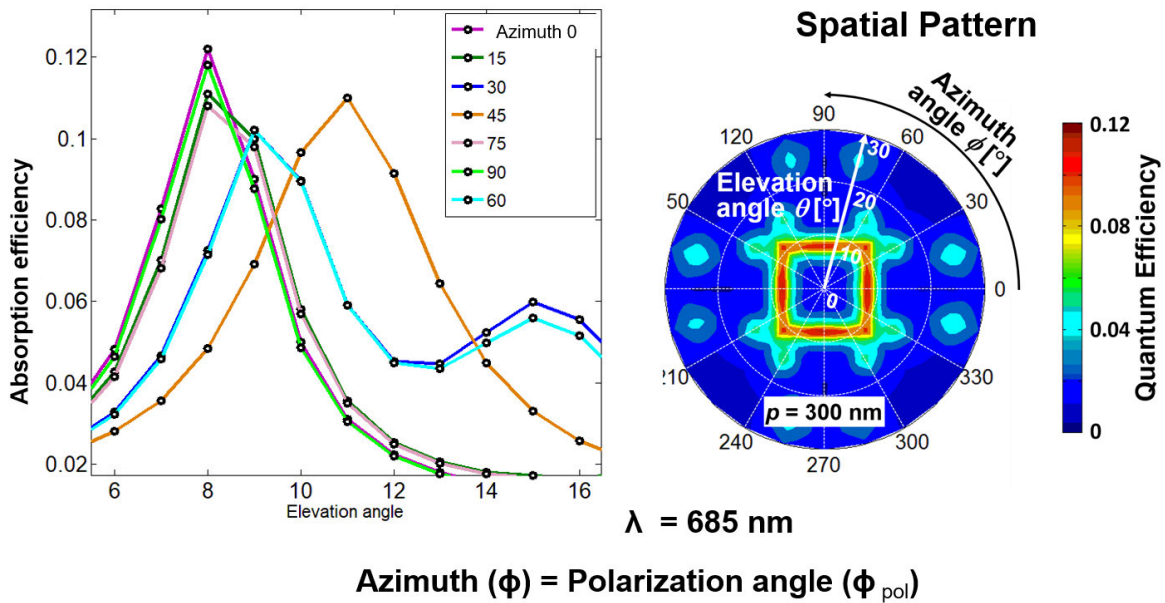


Fig.4.21 The gaussian peak distribution and the spatial pattern of quantum efficiency with respect to the azimuth and elevation angles for SOI PD with 2D hole array grating, $t_{\text{SOI}} = 100 \text{ nm}$ and $p = 300 \text{ nm}$.

component is rotated with the azimuth angle) the spatial pattern of quantum efficiency with respect to the incidence angle is investigated for the device with grating period, $p = 300$ nm and shown in Fig. 4.21. The gaussian peak is shifted until azimuth angle reaches 45° and again shifted back gradually to the original position as azimuth angle is further increased to 90° . In Fig. 4.22 the FDTD and theoretical spatial pattern for the devices with periods, $p = 260$ to 340 nm is shown. The FDTD spatial pattern reproduces the theoretical spatial pattern with the contour lines aligned in four-fold symmetry. The movement of contour plot with respect to the period, follows the same trend observed in the 1D L/S grating except for the case of $p = 280$ nm. In the case of $p = 280$ nm, the peak quantum efficiency reaches a high value of 0.14 at normal incidence because the λ_g is shortened closer to the value of grating period, 280 nm. This shortening of wavelength in the SOI slab is the reason for a small shift in the peak angle of around 2° . In the case of forward and backward waves, the shift is larger and smaller than the theoretical peak, respectively. The propagation wavelength shift also depends on the layout of the top layer of the SOI slab. The difference in the grating type, cause the difference in the propagation wavelength. However, the appearance of the four-fold symmetry with less intense around the center point with high intensity could be explained by the coupling of incident light with the high order mode of TM waveguide (TM_1), $\lambda_g = 467$ nm. The reason for the smaller quantum efficiency for 2D hole array grating may be due to the smaller diffraction efficiency.

Fig.4.23 a) shows the top view of the fabricated SOI PD with 2D hole array SP antenna with optical micrograph of the PD and the scanning-electron micrographs of the 2D hole array grating with $p = 300$ nm. The spatial pattern

of the external quantum efficiency with respect to the azimuth angle range of 0 to 180° and elevation angle range of 0 to 14° for the device with $p = 300$ nm and SOI thickness as same as the FDTD and theory ($t_{SOI} = 100$ nm) and $t_{BOX} = 400$ nm. The quantum efficiency is measured by fixing the laser source and rotating

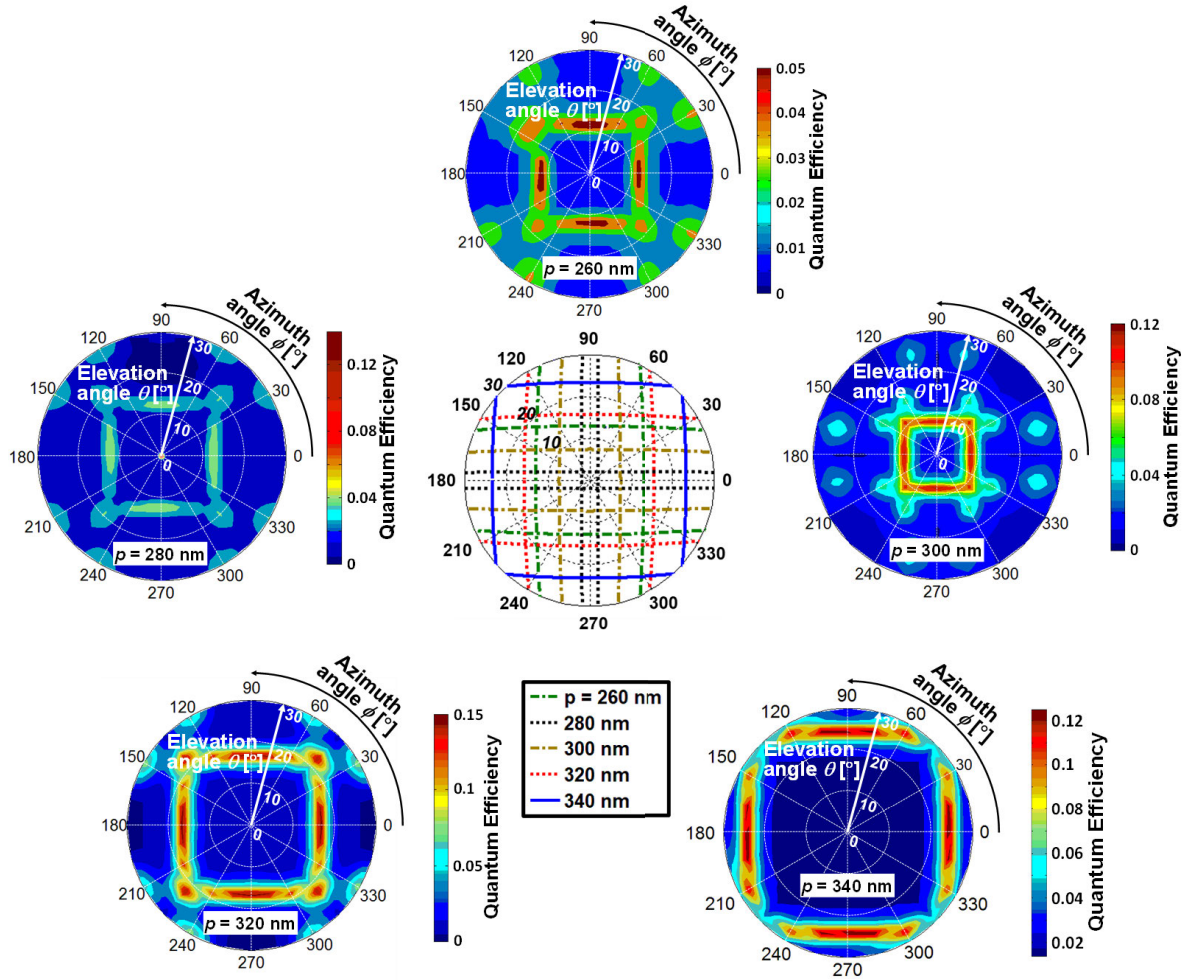


Fig.4.22 FDTD spatial patterns of quantum efficiency with respect to the azimuth and elevation angles for SOI PD with 2D hole array grating, $t_{SOI} = 100$ nm with different p and the corresponding theoretical spatial patterns. $\phi = \phi_{pol} = 90^\circ$.

the azimuth and tilting the gonio stage for ϕ and θ dependence. The measured spatial pattern reproduces the simulated spatial pattern very well but with the less contour intensity in some areas. The quantum efficiency is low compare to the case of 1D L/S as well. However, the quantum efficiency of the fabricated device needs to be improved like 1D L/S grating. An abnormal substrate/gate bias dependence is found out in this case also due to the presence of fixed oxide and/or trapped charges and therefore QE could not be maximized. Otherwise, higher QE ($\sim 6.5\%$) is routinely obtained which will be shown in other experimental data in Fig.4.25 and 4.26.

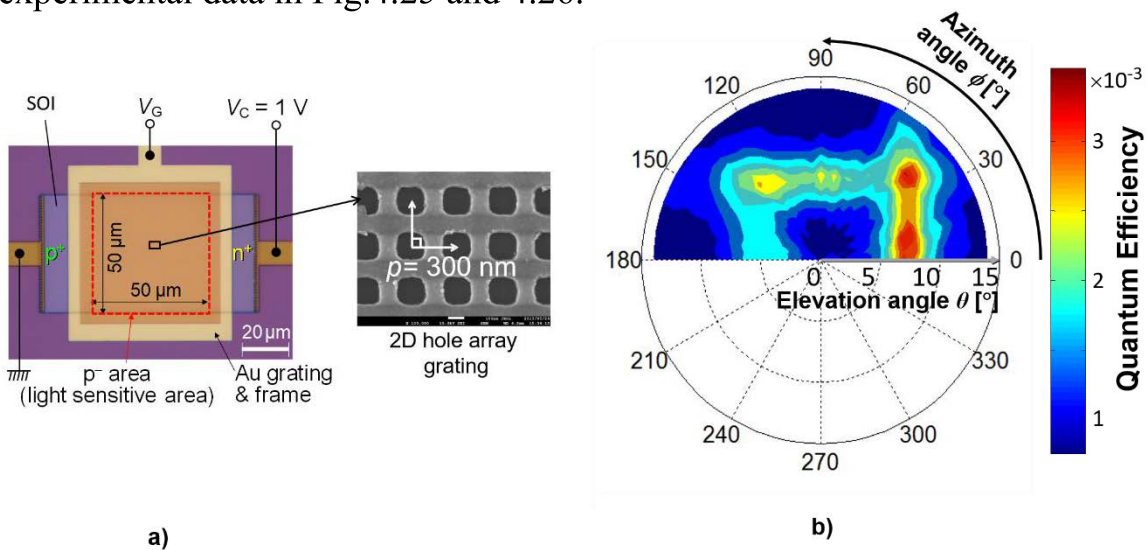


Fig.4.23 a) Top views of the fabricated SOI PD with SP antenna. Optical micrograph of the PD, scanning-electron micrographs of 1D L/S grating b) Experimental spatial patterns of quantum efficiency with respect to the azimuth and elevation angles for SOI PD with 1D L/S grating, $t_{SOI} = 100$ nm with period, $p = 300$ nm. ($\phi = \phi_{pol} = 90^\circ$).

4.4.3 Polarization (ϕ_{pol}) angle dependence

The azimuth-elevation angle dependence could be analyzed for polarized incident lights for the SOI PD with 2D hole array SP antenna at different angles such as, $\phi_{pol} = 0$ to 90° for the device with $t_{SOI} = 100$ nm and $p = 300$ nm by FDTD simulation method. The calculation is done by using the incident light configuration shown in Fig. 4.8. The polarized light is tilted along xz and yz plane and rotated along the azimuth angle. The calculated absorption efficiency is shown in Fig. 4.24 with the theoretical spatial pattern.

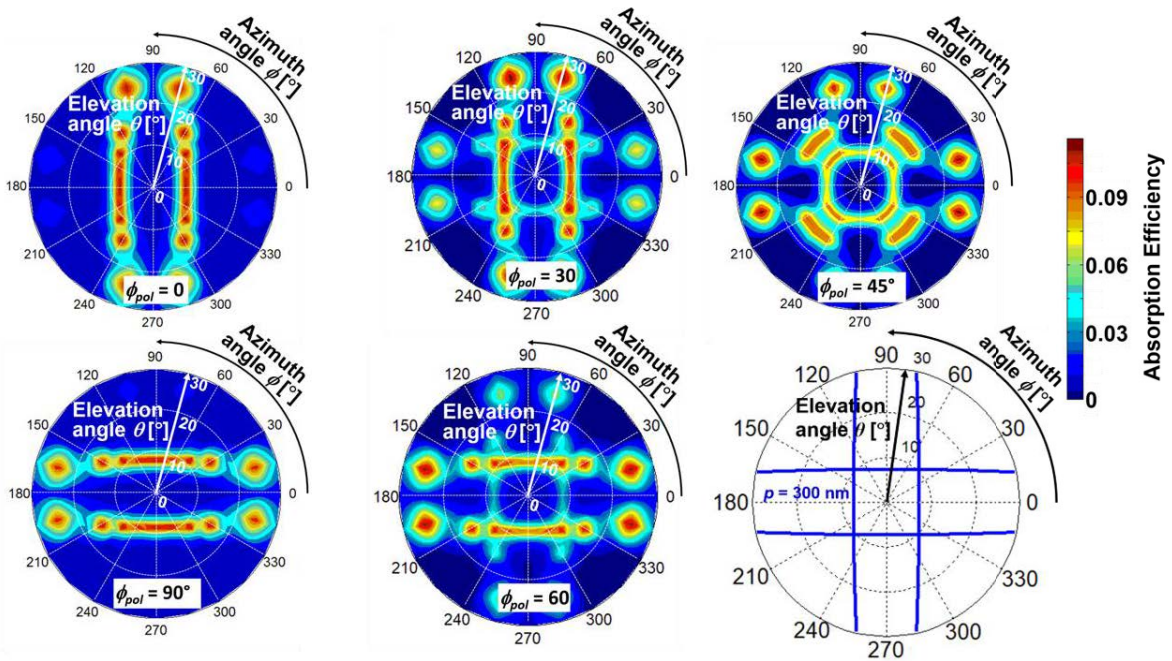


Fig.4.24 a) Simulation spatial patterns of absorption efficiency with respect to the azimuth and elevation angles for SOI PD with 1D L/S grating, $t_{SOI} = 100$ nm with period, $p = 300$ nm for different polarizations(ϕ_{pol}) with the theoretical spatial pattern for $p = 300$ nm and $t_{SOI} = 100$ nm.

For the case of $\phi_{pol} = 0$, the spatial pattern shows a contour curve with two-fold symmetry in vertical direction whereas in the case of $\phi_{pol} = 90^\circ$, the symmetrical pattern is aligned along the horizontal direction. This is due to the highly

symmetric geometry of the 2D hole array grating. In the case of $\phi_{pol} = 45^\circ$, the resultant pattern is appeared as the super-position of the parallel and perpendicular polarization. The theoretical estimation is required to support the numerical prediction. The nature of the waveguide mode is slightly altered in the SOI slab in the simulation condition due to the finite thickness and extra grating layer on top of the SOI slab which differs from the analytical structural

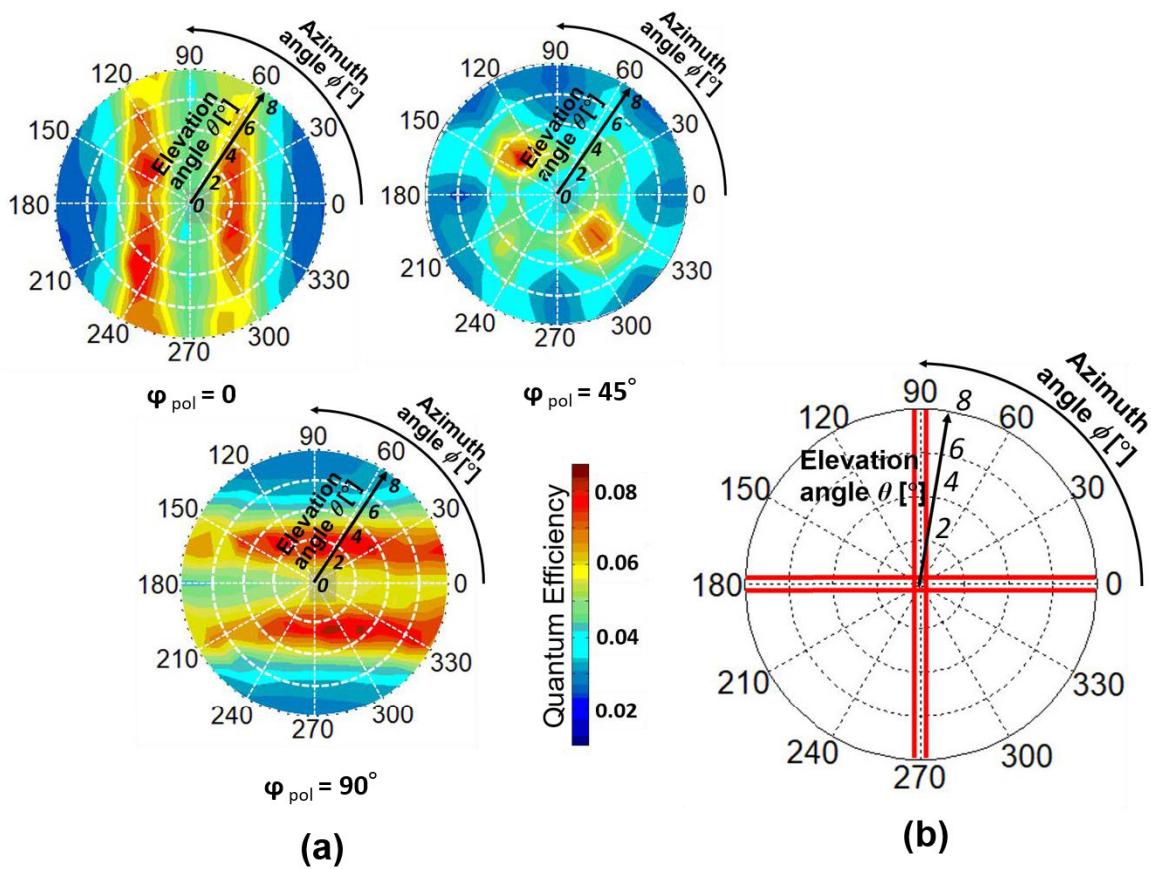


Fig.4.25 a) Experimental spatial patterns of quantum efficiency with respect to the azimuth and elevation angles for SOI PD with 2D hole array grating, $t_{SOI} = 105$ nm with period, $p = 270$ nm for polarizations, (i) $\phi_{pol} = 0$, (ii) $\phi_{pol} = 45^\circ$ and (iii) $\phi_{pol} = 90^\circ$, b) theoretical spatial pattern for $p = 270$ nm and $t_{SOI} = 105$ nm.

dimensions. The theoretical spatial pattern is also shown for the device with grating period, $p = 300$ nm (Fig.4.24). The peak positions of the theory and the FDTD are in good agreement.

The experimental demonstration for the evaluation of the polarization dependence with respect to the azimuth-elevation angle of the device, SOI PD with 2D hole array grating SP antenna is discussed here. This investigation is done by utilization of the measurement setup consists of $\alpha\beta$ gonio stage and

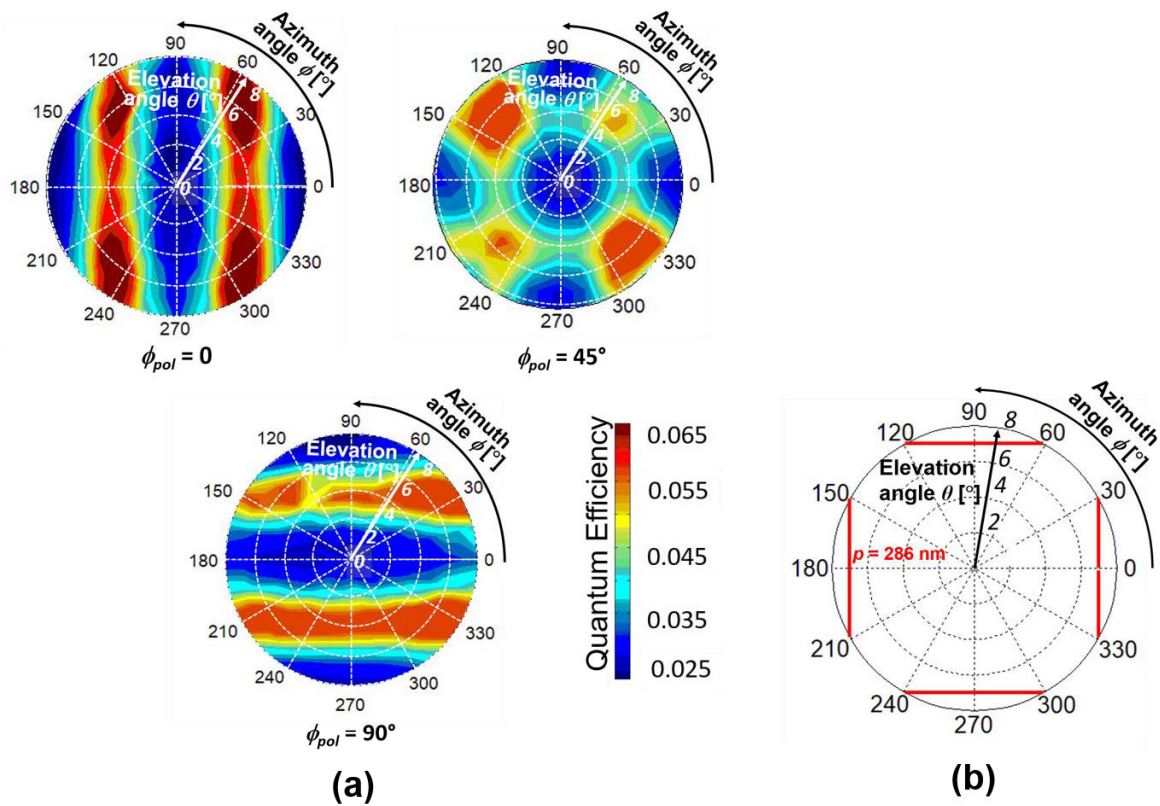


Fig.4.26 a) Experimental spatial patterns of quantum efficiency with respect to the azimuth and elevation angles for SOI PD with 2D hole array grating, $t_{SOI} = 105$ nm with period, $p = 286$ nm for polarizations, (i) $\phi_{pol} = 0$, (ii) $\phi_{pol} = 45^\circ$ and (iii) $\phi_{pol} = 90^\circ$, b) theoretical spatial pattern for $p = 286$ nm and $t_{SOI} = 105$ nm.

rotational stage. The half waveplate is used to control the polarization of the incident light. The Fig. 4.25 and 4.26 shows the (a) experimental spatial pattern of the SOI PD with 2D hole array SP antenna of $p = 270$ and 286 nm, respectively for different polarizations and (b) the theoretical spatial pattern. The polarization 0 and 90° exhibits a two-fold symmetry and highly symmetric as in the case of FDTD simulation. And the polarization 45° clearly shows the super-position of the results of the polarizations 0 and 90° . The theoretical spatial pattern with the same SOI thickness and period is compared. The peak position of the experiment is agreed with the theory. The quantum efficiency of the device is 0.08 which is greatly improved when compared with the case of $\phi = \phi_{pol}$. The spatial pattern shows the azimuth-elevation distribution with polarization dependence.

4.4.4 Comparison of peak angle and quantum efficiency (1D and 2D SP antenna)

The incident angle at which maximum quantum efficiency obtained is considered as peak angle. The peak angle of the simulated results of the SP antenna of 1D L/S grating or 2D hole array grating is compared with the theory peak as a function of grating period of the SP antenna at the condition $\phi = \phi_{pol} = 90^\circ$. In Fig.4.27 peak angle is plotted vs. grating period. In the case of L/S grating and hole array grating, angle deviation of $\sim 0.5^\circ$ and $\sim 1^\circ$ with respect to the theory is obtained, respectively. For the case of forward waves with $p > \lambda_g$ (300, 320 and 340) and backward waves with $p < \lambda_g$ (280 and 260) the angular shift is increased and decreased, respectively. The difference in the grating difference in the propagation wavelength in the SOI slab waveguide. In Fig.4.28

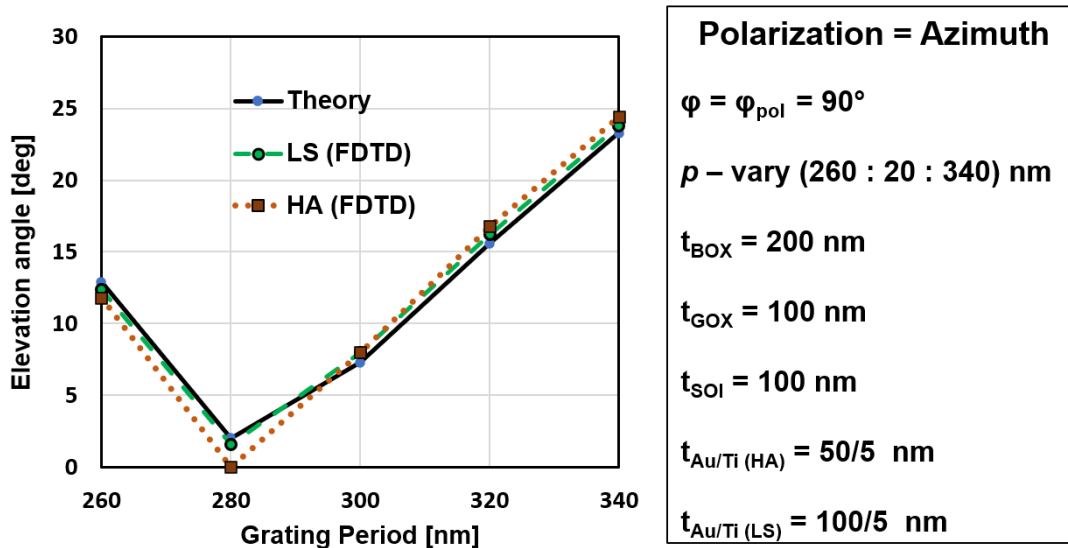


Fig.4.27 Comparison of peak angle of 1D L/S grating and 2D hole array grating with theory with respect to the effect of grating period, p . Incident angle configuration is such that the $\phi_{pol} = \phi$.

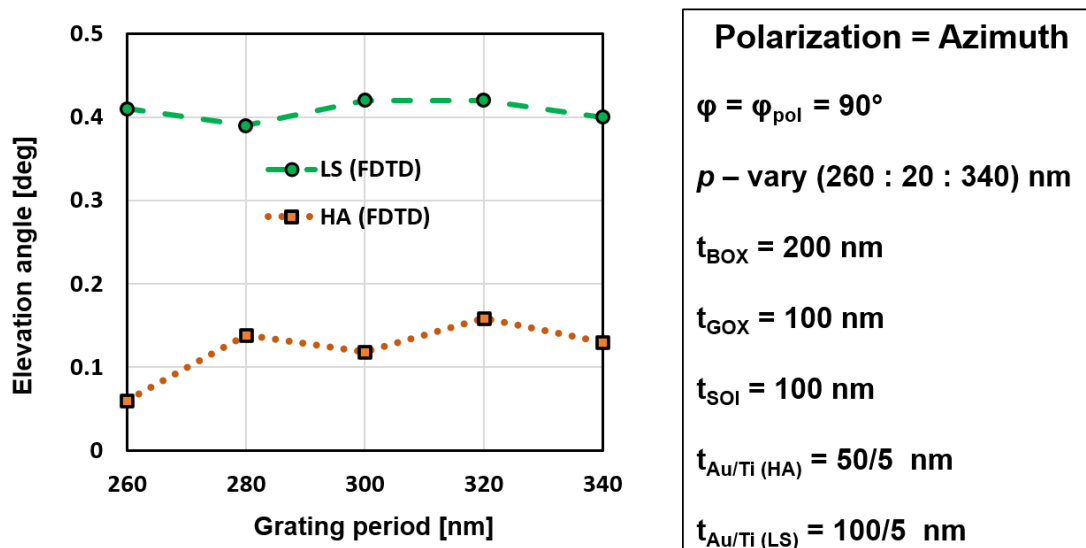


Fig.4.28 Comparison of absorption efficiency of 1D L/S grating and 2D hole array grating with theory with respect to the effect of grating period, p . Incident angle configuration is such that the $\phi_{pol} = \phi$.

the absorption efficiency of the SP antenna of 1D L/S grating and 2D hole array grating is compared as a function of grating period of the SP antenna at the condition $\phi = \phi_{pol} = 90^\circ$. The 1D L/S grating allows maximum coupling of light between the diffracted waves and propagating waves for all the devices with different p . However, the 2D hole array grating exhibits less absorption efficiency when compared with the L/S due to less diffraction efficiency. Thanks to lateral light propagation in the SOI PD for the high quantum efficiency of 40% in SOI PD with L/S grating. In Table 4.6, the comparison of peak angle and absorption efficiency of L/S and hole array SP antenna with

Table 4.6 Comparison of peak angle and absorption efficiency of L/S and hole array SP antenna for fixed grating period, $p = 300 \text{ nm}$, $\phi_{pol} = \phi$.

P =300 nm	Peak Angle(°)	
	HA	LS
Exp	8.6	6
FDTD	8	7.8
Theory	7.3	7.3

P =300 nm	Quantum Efficiency	
	HA	LS
Exp	0.0028	0.081
FDTD	0.118	0.42

Polarization = Azimuth
$\phi = \phi_{pol} = 90^\circ$
$t_{BOX_FDTD} = 200 \text{ nm}$
$t_{BOX_EXP} = 400 \text{ nm}$
$t_{Au/Ti (HA_FDTD)} = 50/5 \text{ nm}$
$t_{Au/Ti (HA_EXP)} = 100/5 \text{ nm}$
$t_{Au/Ti (LS_FDTD)} = 100/5 \text{ nm}$
$t_{Au/Ti (LS_EXP)} = 100/5 \text{ nm}$
$p = 300 \text{ nm}$
$t_{GOX} = 100 \text{ nm}$
$t_{SOI} = 100 \text{ nm}$

fixed grating period of 300 nm is shown. The peak angle of measured hole array and L/S grating shows a deviation of $\sim 1.3^\circ$ respectively whereas the simulated hole array and L/S shows a deviation of ~ 0.7 and ~ 0.5 respectively. The reason for the deviation of experimental value from the FDTD results is due to a small discrepancy in the SOI thickness of around 1 nm. The quantum efficiency of the experimental demonstration and the FDTD simulation is also compared. The performance of the fabricated device in terms of quantum efficiency is comparatively lesser than the simulated devices. The integrity of the structure and the optical characteristics of the material need to be improved.

Table 4.7 shows the comparison between the external quantum efficiency of the two experimental conditions. In the first case both the devices hole array and L/S grating shows less quantum efficiency. The newly fabricated devices with high integrity of structure and much improved optical properties of the material exhibits a high quantum efficiency of 0.081 and 0.4 for hole array SP antenna and LS SP antenna, respectively. Thus, high performance devices are fabricated and the capability of incident angle of light is exhibited.

Table 4.7 Comparison of measured quantum efficiency between the two cases

1. $\phi = \phi_{pol}$ and 2. ϕ_{pol} is fixed.

QE	I ($\phi = \phi_{pol} = 90^\circ$)	II $\phi_{pol} = 90^\circ$
HA	0.0035	0.065
L/S	0.081	0.4

Fig. 4.29 shows the comparison of peak angle of 1D L/S grating and 2D hole array grating with theory with respect to the effect of grating period, $p = 270$ and 286 nm and quantum efficiency of the two devices $p = 270$ and 286 nm. Incident angle condition is the $\phi_{pol} = \phi = 90^\circ$. The peak angle of hole array of $p = 270$ and 286 nm is deviated from the theory by $\sim 2.2^\circ$ and $\sim 2.7^\circ$ respectively. For L/S of $p = 270$ and 286 nm, $\sim 3.4^\circ$ and $\sim 3.3^\circ$ is obtained. The quantum

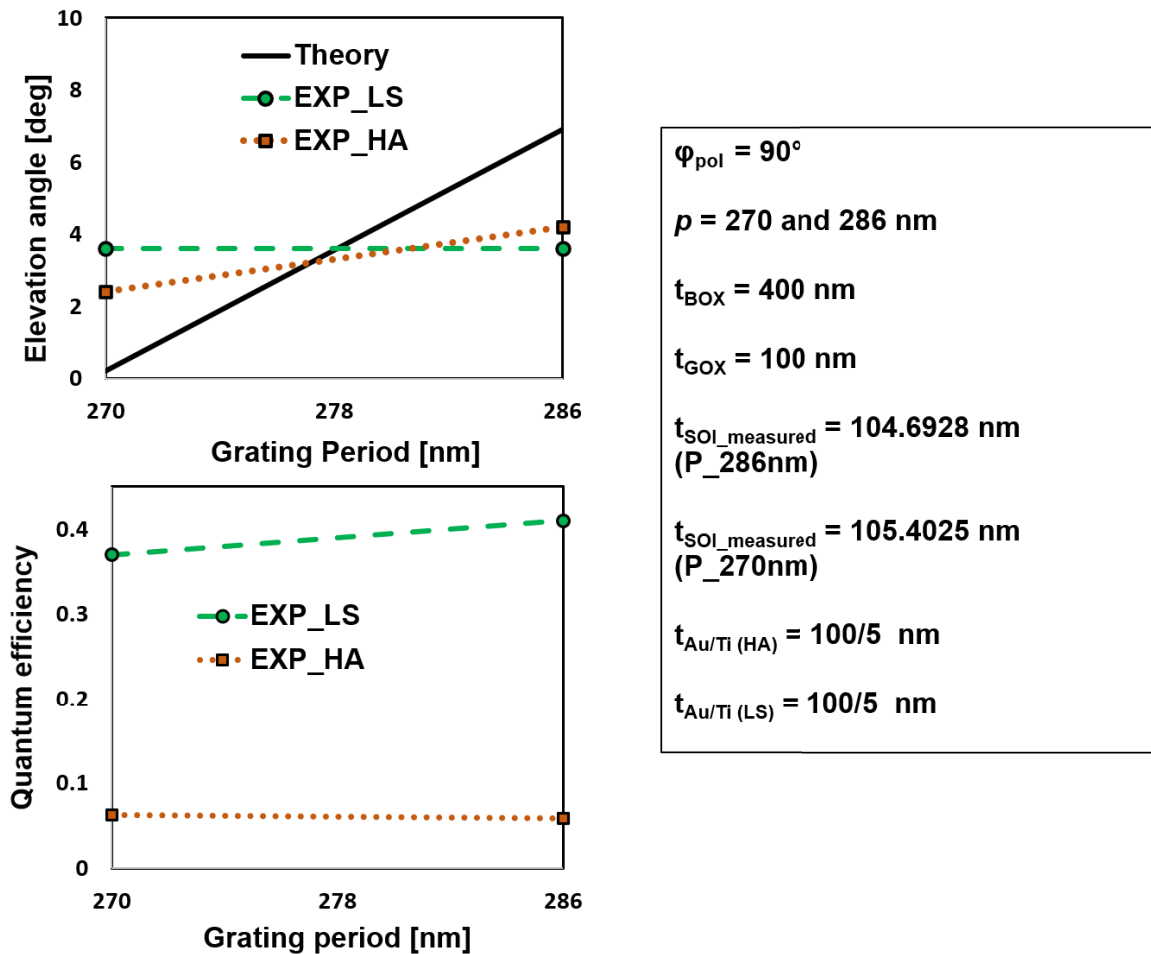


Fig. 4.29 Comparison of peak angle and quantum efficiency of 1D L/S grating and 2D hole array grating with theory with respect to the effect of grating period, $p = 270$ and 286 nm. Incident angle condition is the $\phi_{pol} = \phi = 90^\circ$.

efficiency comparison shows apparently that the SOI PD with L/S exhibits a high quantum efficiency of 46%.

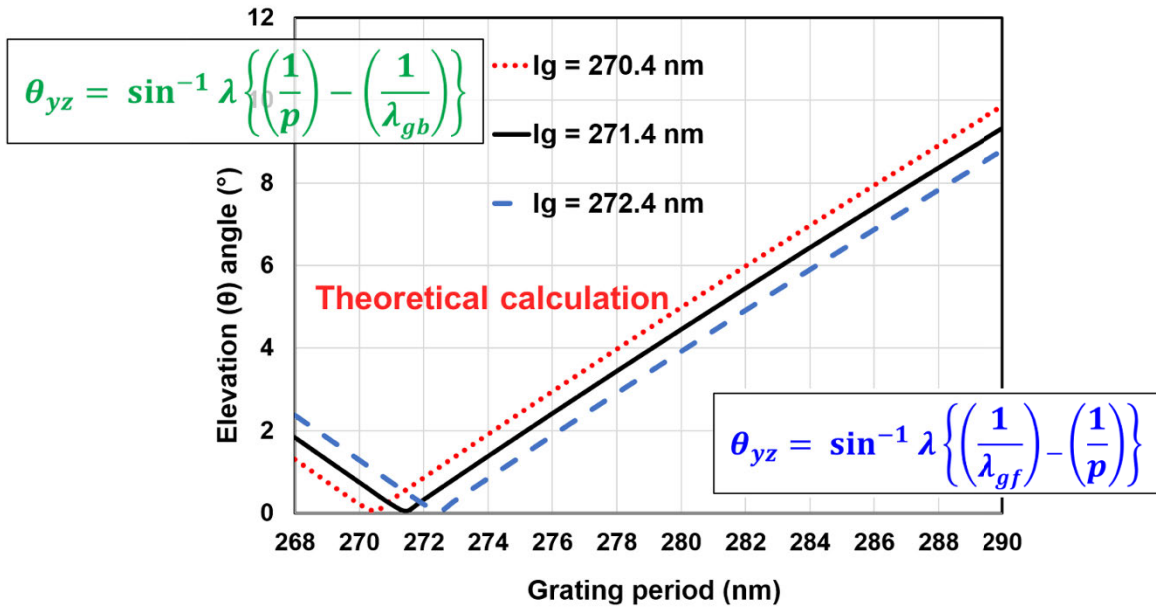


Fig.4.30 Effect of propagation wavelength on elevation angle.

Table 4.8 Assumed propagation wavelength and its corresponding SOI thickness

	p = 270 nm (Y5X7)		p = 286 nm (Y5X11)	
	LS	HA	LS	HA
Peak Angle [°] (Measured)	3.6	2.4	3.6	4.2
SOI thickness [nm] (Assumed)	103.23		102.25	
(TM ₀) λ _g [nm] (Assumed)	275.69		278.1	

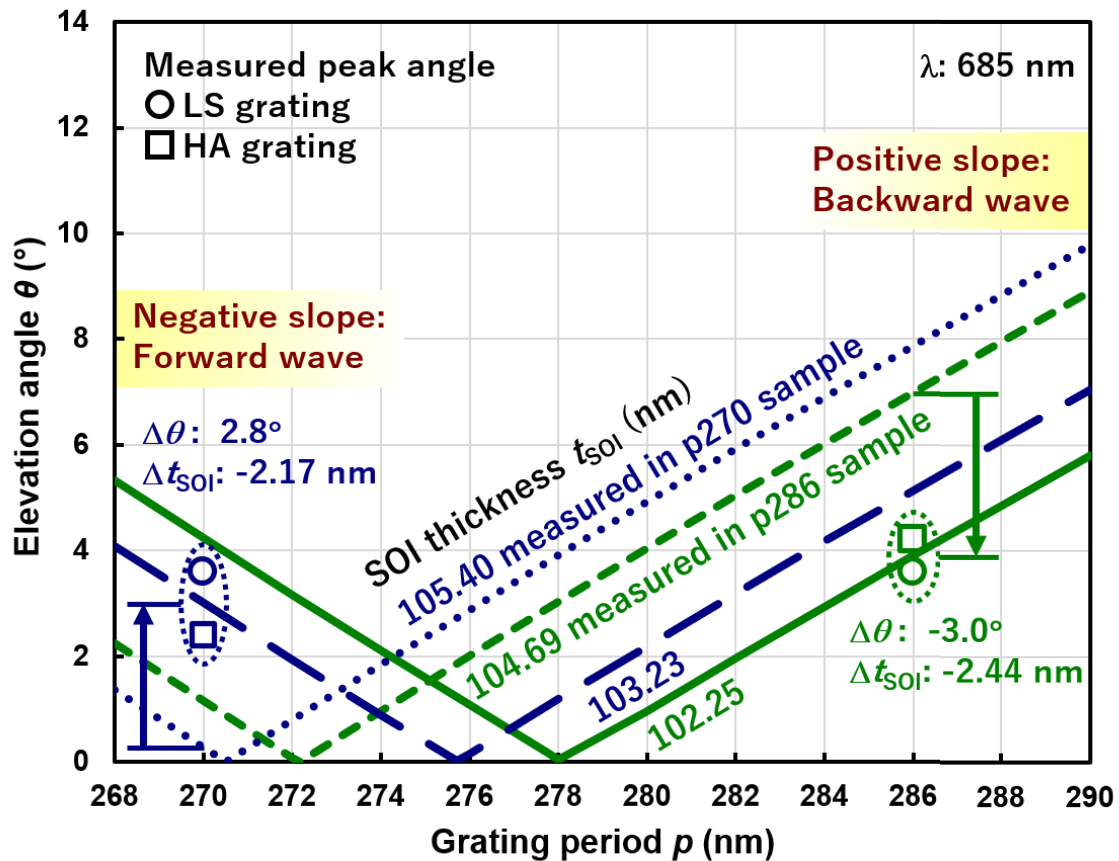


Fig.4.31 Comparison of measured and theoretical peak angles.

In Fig 4.30, the effect of propagation wavelength is shown. The change of propagation wavelength with 1 nm shows significant effect in the elevation angle. The reason for the peak angle deviation of the measured results may be due to the change in propagation wavelength. This propagation wavelength changes occur due to the variation in the SOI thickness. Thus, we can predict the SOI thickness for the measured peak angle. In Fig. 4.31 shows the comparison between measured and theoretical peak elevation angles. Samples with the grating periods of 270 and 286 nm have different measured SOI thicknesses of 105.40 and 104.69 nm, respectively. Deviation from the

theoretical lines based on the measured SOI thickness can be explained by 2.17 and 2.44 nm decrease of the SOI thicknesses, respectively. Note that the decrease in SOI thickness results in the increase and the decrease of the peak elevation angles for forward and backward waves, respectively. Thus, this graph evidently exhibits that change in SOI thickness of around 2 nm, results in the shift of the peak angle. Therefore, it is concluded that the small surface roughness causes this angle shift. Table 4.8 shows the assumed propagation wavelength and the corresponding SOI thickness calculated for the measured peak angles by using phase matching condition and transcendental equations.

4.4.5 Improvement of Angular Resolution

The angular resolution of our devices, 1D and 2D SP antenna could be determined by calculating the FWHM of the gaussian peak distribution output signal at a fixed azimuth angle = 90° and shown in Fig. 4.32. As shown in the figure, the L/S and HA shows a high QE of 45% and 6.5% respectively. The peak width of our devices is compared with the conventional ASP and shown in the Table 4.9. Our proposed device has an angular resolution of 2.2° and 2° for 2D and 1D SP antenna, respectively, whereas the conventional ASP shows 8° . For comparison the peak width of a bare photodiode is also shown which is larger than 80° . Thus our device exhibits a much improved angular resolution than the conventional ASP.

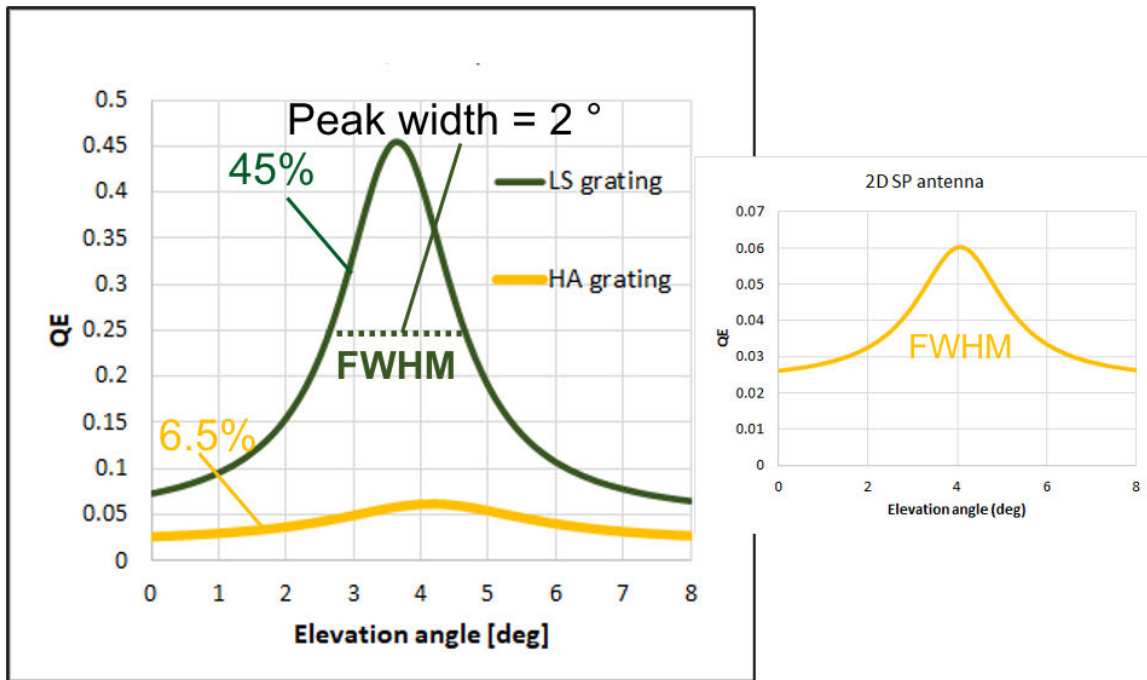


Fig.4.32 Peak width of the measured devices, L/S and 2D HA grating at fixed azimuth angle

Table 4.9 Comparison of peak width with the conventional ASP

Device	Peak width (°)
Proposed ASP (2D SP antenna)	2.2
Proposed ASP (1D SP antenna)	2
Conventional ASP (Interleaved diodes within well diode)	8
Bare Pixel	Larger than 80

4.4.6 Possibility of Color Image Sensor

A color photograph could be accomplished if a camera is comprised of image sensor that discriminates the wavelength from the incident light. Throughout our study on angle sensitive behaviour of the SOI PD with SP antenna, monochromatic light is used for simplicity. In order to realize a color image sensor, an additional optical component which acts as a color filter is required.

4.5 Conclusion

Thus, this chapter explains about the design of the proposed photodetector consists of SOI pn-junction photodiode with SP antenna (1D L/S grating and 2D hole array grating) for azimuth-elevation angle detection and evaluation of the same through electromagnetic simulation based on 3D FDTD (Finite Difference Time Domain) method for numerical prediction. The numerically predicted azimuth-elevation angular distribution is clarified by the theoretical concept and further verified by the numerical prediction and experimental demonstration of the fabricated devices.

Chapter 5

SUMMARY AND CONCLUSION

5.1 Summary

Recent development in the research of image sensors focuses on the pixel level CMOS photodetector to capture the incident angle of light in addition to the intensity for computational imaging technology. To realize this technology based on light field detection, the optical system with traditional models were constructed. Such kind of light field cameras are based on rotating cameras, large camera array, mirror-based cameras and pinhole array cameras. All these models make the optical system bulky and the construction cost is also very high. Research towards miniaturization, leads to the development of microlens array placed in front of the image sensors. However, this system also complex and the need for a pixel level detector-based CMOS technology is started to strive the research field and commercial industry based on image sensor such as Hitachi, SONY, Toshiba, etc. The currently developed angle sensitive pixels (ASP) could capture the light fields enables applications such as lens-less imaging and 3D imaging, but the drawback is only one light field parameter of the incident light is detected and the efficiency of the detector is low. To overcome this drawback, we proposed a pixel level detector based on CMOS technology to detect the incident angle of light with high quantum efficiency. We have already developed a CMOS photodetector based on SOI technology. We have achieved a high quantum efficiency in SOI photodiode (PD) by incorporating a surface plasmon (SP) antenna over it. In this thesis, our goal is to investigate the incident angle dependence of the SOI PD with SP antenna of

1D L/S grating or 2D hole array grating for enabling potential applications such as lensless imaging, 3D imaging and depth refocusing.

In *chapter 1*, the basics of the light field or plenoptic imaging with interesting applications were discussed briefly. The need for light field camera with angle sensitive pixels, ASP was explained by discussing the existing light field cameras and its limitations. The introduction of our novel device, SOI photodetector based on the CMOS technology was discussed with the current status of the research. The motivation, objective and synopsis of the book chapter is provided.

In *chapter 2*, the structure of our proposed device, based on pixel level CMOS photodetector, SOI PD with SP antenna of two different structures was discussed. The SP antenna is composed of either 1D L/S grating or 2D hole array grating to couple the diffracted light with the SOI PD. The SOI PD is similar to the structure of the SOI slab waveguide as the Si layer is sandwiched between the SiO₂ layers of gate oxide and buried oxide layers. The SP antenna is electrically isolated from the photodiode by a gate oxide layer. This enables SP antenna to act as a gate electrode to increase the quantum efficiency by controlling the depletion layer. We used a commercial SOI wafer for the fabrication process, the complete process flow of the device fabrication including gate oxide adjusting, antenna formation and gate pad formation was shown and explained along with the device packaging for measuring the output photocurrent of the photodetector. The incident angle dependence has to be investigated under different light arrival directions. To achieve this with a fixed light source, a measurement set-up was constructed based on the different tilting

and azimuth stages called goniometer and rotational stages, respectively. The measurement set-up was shown schematically explained for the analysis of output current measurement.

In *chapter 3*, involves the description of the theoretical concept behind the principle of angle detection in the proposed device. The principle of operation of the lateral light wave propagating in the SOI slab along with different waveguide modes was explained well and exhibited graphically using the dispersion relations for symmetrical slab waveguide. The concept of angle detection involves efficient coupling between the diffracted light from the SP antenna and the SOI waveguide mode. A mathematical equation was formalized based on this concept which relates the incident angle of the light with wavelength of incident light and propagating mode and the grating period of the antenna. The incident angle data for SOI PD with SP antenna of 1D or 2D hole array grating was represented in polar coordinates in the form of spatial pattern. The spatial pattern for various periods and different waveguide modes was also discussed in this chapter.

In *chapter 4*, the simulation and measurement results were represented. An introduction on the simulation method, 3D Finite-Difference Time-Domain (FDTD) and designing of devices and optimization of device structure was discussed well. The incident light configuration two different analysis was shown, and the evaluation of azimuth-elevation angle dependence was carried out based on that. The results are measured from the experimental set-up and plotted in the form of spatial pattern to simultaneously represent the azimuth and elevation angle dependence. Using the simulation and measurement set-up

different investigations were done discussed. The spatial pattern for calculated quantum efficiency and theoretical estimation on the effect of grating period of both the type of SP antennas, 1D L/S grating and 2D hole array grating when the polarization of light is rotated along with the azimuth angle of light was represented and discussed with a fair comparison. The azimuth-elevation angle dependence of the fabricated devices of fixed period for 1D and 2D grating was measured by rotating and tilting the device such that the polarization component was rotated along with the azimuth angle. Although, the angles were limited, good reproduction of data was achieved. Further investigation on polarization dependence was investigated for both the devices, 1D and 2D grating. The polarization characteristics of 1D and 2D SP antenna exhibits different from each other. Thus, theoretical estimation, numerical prediction and experimental demonstration of angle sensing capability was investigated and discussed in this chapter successfully.

The objectives of the thesis have been analyzed successfully as follows,

1. Device is characterized for angle selectivity.

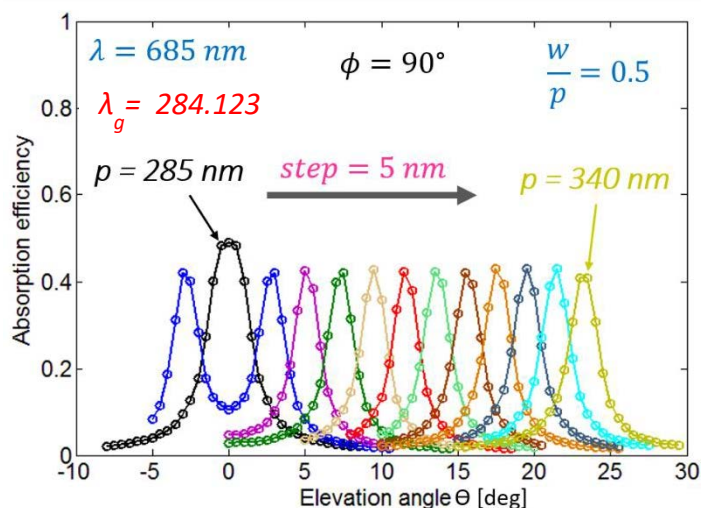


Fig.5.1 Angle selectivity for SOI PD with 1D SP antenna for different grating period, p

2. Theoretical formulation and plotting spatial pattern.

$$\theta_{yz} = \sin^{-1} \lambda \left\{ \left(\frac{1}{\lambda_{gf}} \right) - \left(\frac{1}{p} \right) \right\}$$

$$\theta_{yz} = \tan^{-1}(\tan \theta \sin \phi)$$

$$\theta_{xz} = \tan^{-1}(\tan \theta \cos \phi)$$

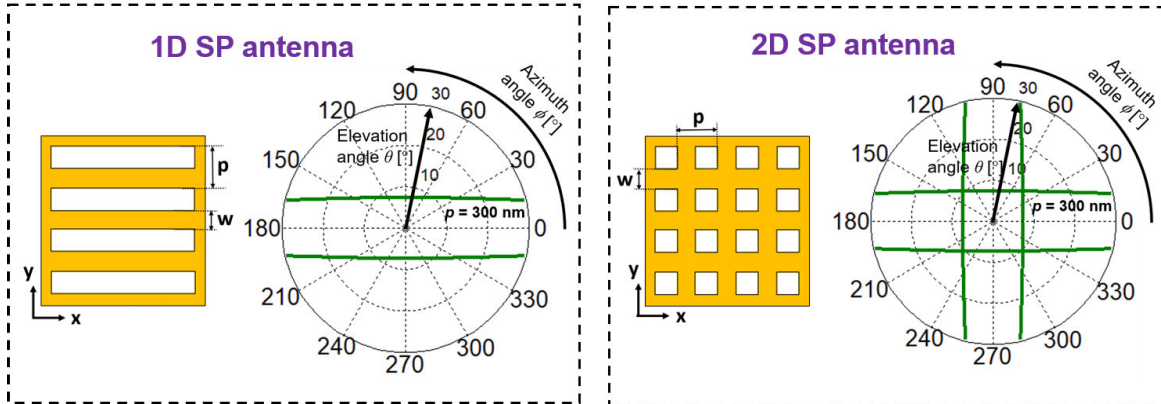


Fig.5.2 Theoretical formulation based on phase matching condition for predicting the angle and its corresponding spatial pattern for both 1D and 2D SP antenna

3. Evaluation by FDTD and its spatial pattern

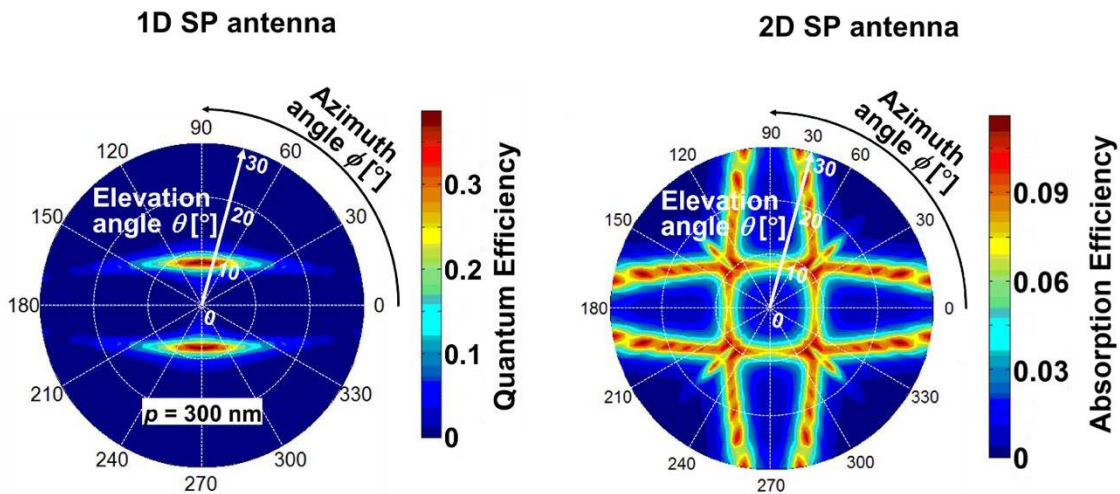
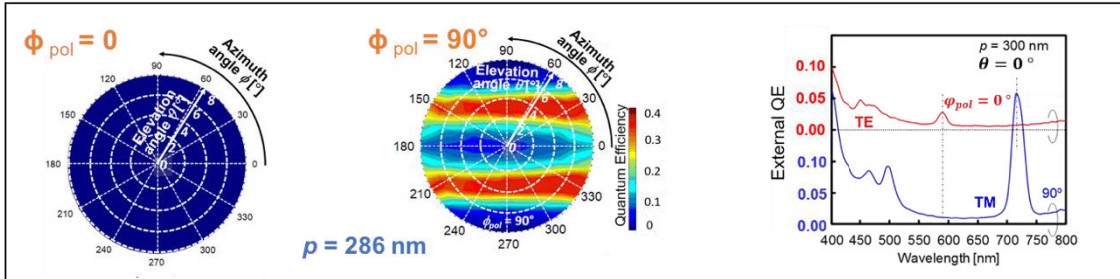


Fig.5.3 Evaluation of the device by FDTD for calculating the output response and its corresponding spatial pattern for both 1D and 2D SP antenna

4. Experimental Demonstration of angle selectivity

1D SP antenna



2D SP antenna

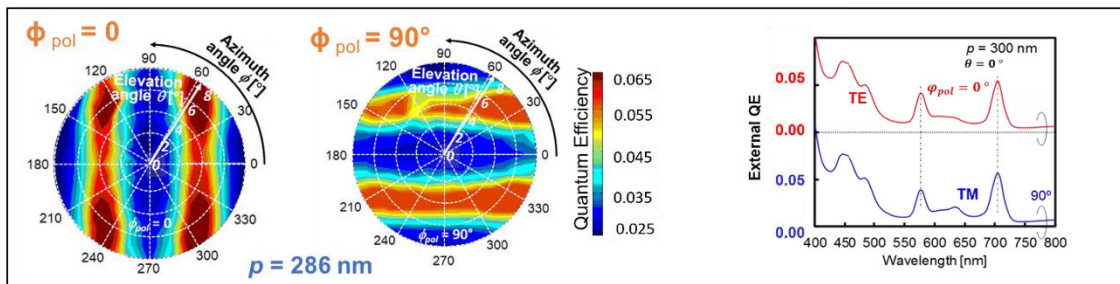


Fig.5.4 Experimental spatial pattern for 1D and 2D SP antenna for parallel and perpendicular polarization and its corresponding spectroscopic characteristics

5. Understanding theoretical, numerical and experimental results

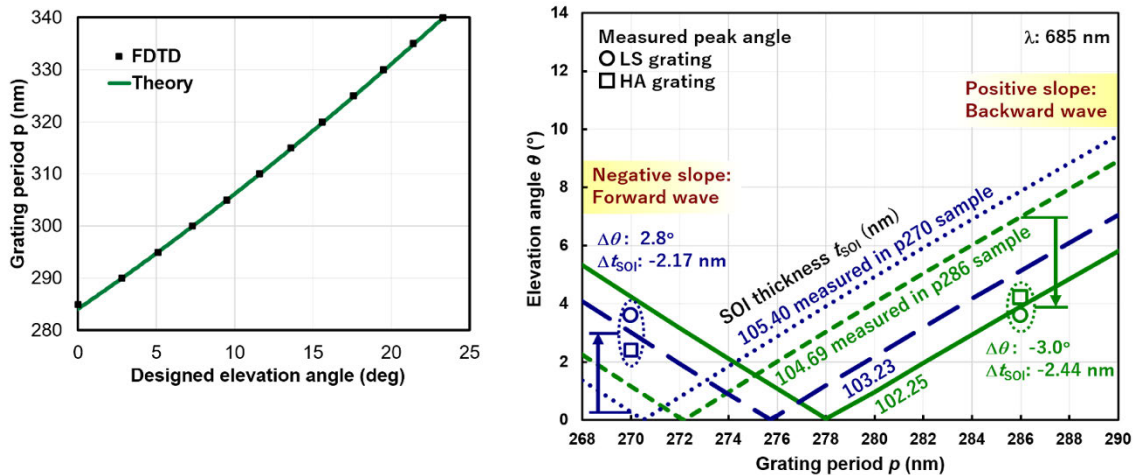


Fig.5.5 Comparison of FDTD and theory peak position (coincides with each other) and measured and theory peaks (fitting line shows peak deviation is due to small discrepancy in the SOI thickness)

5.2 Conclusion

➤ **Proposal of ASP**

A new type of ASP with the following features has been proposed,

- SOI technology
- CMOS compatible
- Pixel scale
- Angle selectivity
- Device structure – simple

➤ **Origin of angle selectivity**

SP antenna discriminates angle by selective coupling of diffracted light and lateral propagation light when phase matching condition is satisfied.

➤ **Unique feature of device**

- SP antenna realizes high QE up to 45% (1D L&S) and excellent angular resolution (FWHM~2 deg) after optimizing the geometry (thickness and width) and layout of the grating.
- SP antenna features tuning of peak angle by changing grating period
- An array of pixels including different grating periods could be integrated in a single chip

5.3 Current Issues

The capability of the light detection by our proposed device by varying the azimuth and elevation angle of light is evident from our studies. However, the elevation angle is investigated for a limited angle. In future, the measurement set-up should be constructed to cover a wide range of angle. In order, to realize an image sensor, the PDs need to be arranged in a single chip.

By considering the potential application such as lensless imaging or depth focusing, pixel arrangement and its computational algorithm should be proposed, or a new experimental setup should be proposed for construction and measurement.

5.4 Future Work

1. To explore further into SP antenna of different types, for example, triangular lattice arrangement of hole array SP antenna.
2. Image reconstruction
 - To consider the arrangement of ASP using the SOI PD with L/S grating.
 - Modeling for the output signal of each ASP.
 - Image reconstruction using computational post-processing.

5.4.1 Modelling of ASP

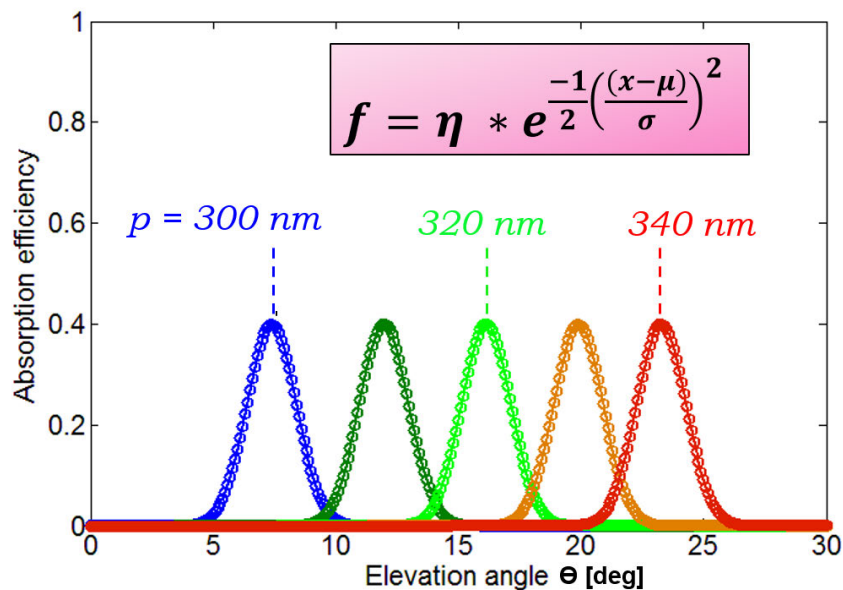


Fig.5.6 Modelling of output response of the ASP as a function of the elevation angle.

References

1. Adelson, E.H.; Bergen, J.R. "The Plenoptic Function and the Elements of Early Vision," *Comput. Model. Vis. Process.* 2020, 3–20, doi:10.7551/mitpress/2002.003.0004.
2. Wetzstein, G.; Ihrke, I.; Lanman, D.; Heidrich, W. "Computational plenoptic imaging," *Comput. Graph. Forum* 2011, 30, 2397–2426, doi:10.1111/j.1467-8659.2011.02073.x.
3. Harris, M. "Focusing on everything," *IEEE Spectr.* 2012, 49, 44–50, doi:10.1109/MSPEC.2012.6189575.
4. Nakamura, Y.; Shimano, T.; Tajima, K.; Sao, M.; Hoshizawa, T. "Lensless Light-field Imaging with Fresnel Zone Aperture," *ITE Tech. Rep.* 2016, 40, 7–8.
5. Y. Maruyama et al., "3.2-MP Back-Illuminated Polarization Image Sensor With Four-Directional Air-Gap Wire Grid and 2.5-um Pixels," in *IEEE Transactions on Electron Devices*, vol. 65, no. 6, pp. 2544-2551, June 2018, doi: 10.1109/TED.2018.2829190.
6. Faraday, M. LIV. "Thoughts on ray-vibrations," London, Edinburgh, Dublin *Philos. Mag. J. Sci.* 1846, 28, 345–350, doi:10.1080/14786444608645431.
7. Gershun, A. "The Light Field," *J. Math. Phys.* 1939, 18, 51–151, doi:10.1002/sapm193918151.
8. Pereira, F.; Da Silva, E.A.B. "Efficient plenoptic imaging representation: Why do we need it?," *Proc. - IEEE Int. Conf. Multimed. Expo 2016*, 2016–Augus, doi:10.1109/ICME.2016.7552939.
9. Austin, R.L.; Denning, B.S.; Drews, B.C.; Fedoriouk, V.B.; Calpito, R.C. "Qualified viewing space determination of near-eye and head-up displays," *J. Soc. Inf. Disp.* 2018, 26, 567–575, doi:10.1002/jsid.729.

10. Wilburn, B.S.; Smulski, M.; Lee, H.H.K. and Horowitz, M.A.; “Light field video camera,” In *Media Processors 2002* (Vol. 4674, pp. 29-36). International Society for Optics and Photonics.
11. Levoy, M. “Light fields and computational imaging,” *Computer* (Long Beach, Calif). 2006, 39, 46–55, doi:10.1109/MC.2006.270.
12. Zheng, G., “Angle-sensitive pixel design for wavefront sensing,” arXiv preprint arXiv:1304.7339, 2013.
13. Saha, T.K.; Lu, M.; Ma, Z.; Zhou, W. “Design of an angle detector for laser beams based on grating coupling,” *Micromachines* 2012, 3, 36–44, doi:10.3390/mi3010036.
14. Zakirullin, R. “Creating optical filters with angular-selective light transmission,” *Appl. Opt.* 2015, 54, 6416, doi:10.1364/ao.54.006416.
15. Sivaramakrishnan, S.; Wang, A.; Gill, P.R.; Molnar, A. “Enhanced angle sensitive pixels for light field imaging,” *Tech. Dig. - Int. Electron Devices Meet. IEDM 2011*, 191–194, doi:10.1109/IEDM.2011.6131516.
16. Wang, A.; Gill, P.; Molnar, A. “Light field image sensors based on the Talbot effect,” *Appl. Opt.* 2009, 48, 5897–5905, doi:10.1364/AO.48.005897.
17. Wang, A.; Gill, P.; Molnar, A. “Light field image sensors based on the Talbot effect,” *Appl. Opt.* 2009, 48, 5897–5905, doi:10.1364/AO.48.005897.
18. Wang, A.; Gill, P.R.; Molnar, A. An angle-sensitive CMOS imager for single-sensor 3D photography. *Dig. Tech. Pap. - IEEE Int. Solid-State Circuits Conf.* 2011, 412–413, doi:10.1109/ISSCC.2011.5746375.
19. Wang, A.; Gill, P.; Molnar, A. Angle sensitive pixels in CMOS for lensless 3D imaging. *Proc. Cust. Integr. Circuits Conf.* 2009, 371–374, doi:10.1109/CICC.2009.5280840.
20. Gill, P.R.; Lee, C.; Lee, D.-G.; Wang, A.; Molnar, A. A microscale camera using direct Fourier-domain scene capture. *Opt. Lett.* 2011, 36, 2949, doi:10.1364/ol.36.002949.

21. Jayasuriya, S.; Sivaramakrishnan, S.; Chuang, E.; Guruaribam, D.; Wang, A.; Molnar, A. Dual light field and polarization imaging using CMOS diffractive image sensors. *Opt. Lett.* 2015, 40, 2433, doi:10.1364/ol.40.002433.
22. Xu, Y.; Lam, M.L.; Georgiev, T.; Zheng, K.C.; Curless, B.; Salesin, D.; Nayar, S.; Intwala, C.; Zhu, H.; Wang, Q.; et al. Light field imaging: models, calibrations, reconstructions, and applications. *Stud. Comput. Intell.* 2017, 18, 1236–1249, doi:10.1631/FITEE.1601727.
23. Wang, A.; Hemami, S.S.; Molnar, A. Angle-sensitive pixels: a new paradigm for low-power, low-cost 2D and 3D sensing. *Stereosc. Displays Appl. XXIII 2012*, 8288, 828805, doi:10.1117/12.910240.
24. Sivaramakrishnan, S.; Wang, A.; Gill, P.; Molnar, A. Design and characterization of enhanced angle sensitive pixels. *IEEE Trans. Electron Devices* 2016, 63, 113–119, doi:10.1109/TED.2015.2432715.
25. Wang, A.; Sivaramakrishnan, S.; Molnar, A. A 180nm CMOS image sensor with on-chip optoelectronic image compression. *Proc. Cust. Integr. Circuits Conf.* 2012, 3, doi:10.1109/CICC.2012.6330604.
26. Wang, A.; Gill, P.R.; Molnar, A. Fluorescent imaging and localization with angle sensitive pixel arrays in standard CMOS. *Proc. IEEE Sensors 2010*, 1706–1709, doi:10.1109/ICSENS.2010.5689914.
27. Hirsch, M.; Sivaramakrishnan, S.; Jayasuriya, S.; Wang, A.; Molnar, A.; Raskar, R.; Wetzstein, G. A switchable light field camera architecture with Angle Sensitive Pixels and dictionary-based sparse coding. *2014 IEEE Int. Conf. Comput. Photogr. ICCP 2014 2014*, doi:10.1109/ICCPHOT.2014.6831813.
28. Ren Ng, Marc Levoy, Mathieu Brédif, Gene Duval, Mark Horowitz, et al.. Light Field Photography with a Hand-held Plenoptic Camera. [Research Report] CSTR 2005-02, Stanford university. 2005, Stanford University Computer Science Tech Report.
29. Wilburn, B.; Joshi, N.; Vaish, V.; Talvala, E.V.; Antunez, E.; Barth, A.; Adams, A.; Horowitz, M.; Levoy, M. High performance imaging using large

- camera arrays. *ACM Trans. Graph.* 2005, 24, 765–776, doi:10.1145/1073204.1073259.
30. Levoy, M.; Ng, R.; Adams, A.; Footer, M.; Horowitz, M. Light field microscopy. *ACM SIGGRAPH 2006 Pap. SIGGRAPH '06* 2006, 924–934, doi:10.1145/1179352.1141976.
31. Ng, R. Fourier slice photography. *ACM Trans. Graph.* 2005, 24, 735–744, doi:10.1145/1073204.1073256.
32. Fiss, J.; Curless, B.; Szeliski, R. Refocusing plenoptic images using depth-adaptive splatting. *2014 IEEE Int. Conf. Comput. Photogr. ICCP 2014* 2014, doi:10.1109/ICCPHOT.2014.6831809.
33. Shroff, S.A.; Berkner, K. Image formation analysis and high resolution image reconstruction for plenoptic imaging systems. *Appl. Opt.* 2013, 52, pp.D22-D31, doi:10.1364/AO.52.000.
34. McMillan, L.; Bishop, G. Plenoptic modeling: an image-based rendering system. *Proc. ACM SIGGRAPH Conf. Comput. Graph.* 1995, 95, 39–46.
35. Radwell, N.; Selyem, A.; Mertens, L.; Edgar, M.P.; Padgett, M.J. Hybrid 3D ranging and velocity tracking system combining multi-view cameras and simple LiDAR. *Sci. Rep.* 2019, 9, 1–7, doi:10.1038/s41598-019-41598-z.
36. Ozcan, A.; McLeod, E. Lensless Imaging and Sensing. *Annu. Rev. Biomed. Eng.* 2016, 18, 77–102, doi:10.1146/annurev-bioeng-092515-010849.
37. Cetin, A.E.; Coskun, A.F.; Galarreta, B.C.; Huang, M.; Herman, D.; Ozcan, A.; Altug, H. Handheld high-throughput plasmonic biosensor using computational on-chip imaging. *Light Sci. Appl.* 2014, 3, pp. e122, doi:10.1038/lsa.2014.3.
38. Jayasuriya, S.; Pediredla, A.; Sivaramakrishnan, S.; Molnar, A.; Veeraraghavan, A. Depth Fields: Extending Light Field Techniques to Time-of-Flight Imaging. *Proc. - 2015 Int. Conf. 3D Vision, 3DV 2015* 2015, 1–9, doi:10.1109/3DV.2015.8.

39. Wang, A.; Molnar, A. Phase-based 3D optical flow sensors for motion detection. *Proc. IEEE Sensors* 2011, 14853, 683–686, doi:10.1109/ICSENS.2011.6127290.
40. Johnson, B.; Peace, S.T.; Wang, A.; Cleland, T.A.; Molnar, A. A 768-channel CMOS microelectrode array with angle sensitive pixels for neuronal recording. *IEEE Sens. J.* 2013, 13, 3211–3218, doi:10.1109/JSEN.2013.2266894.
41. Wang, P.; Menon, R. Computational snapshot angular-spectral lensless imaging, arXiv:1707.08104, 2017, 1–20.
42. Stork, D.G.; Gill, P.R. Lensless Ultra-Miniature CMOS Computational Imagers and Sensors. *SENSORCOMM 2013 Seventh Int. Conf. Sens. Technol. Appl.* 2013, 186–190.
43. Antipa, N.; Kuo, G.; Heckel, R.; Mildenhall, B.; Bostan, E.; Ng, R.; Waller, L. DiffuserCam: lensless single-exposure 3D imaging. *Optica* 2018, 5, 1, doi:10.1364/optica.5.000001.
44. Kuo, G.; Antipa, N.; Ng, R.; Waller, L. DiffuserCam: Diffuser-based lensless cameras. *Opt. InfoBase Conf. Pap.* 2017, Part F46-C, 2016–2018, doi:10.1364/COSI.2017.CTu3B.2.
45. Savage, N., A new angle on imaging. *IEEE Spectrum*, 48(12), pp.15-15, 2011.
46. Al-Saidi, A.; Avis, N.J.; Grimstead, I.J.; Rana, O.F. Distributed collaborative visualization using light field rendering. *2009 9th IEEE/ACM Int. Symp. Clust. Comput. Grid, CCGRID 2009* 2009, 609–614, doi:10.1109/CCGRID.2009.79.
47. Isaksen, A.; McMillan, L.; Gortler, S.J. Dynamically reparameterized light fields. *Proc. ACM SIGGRAPH Conf. Comput. Graph.* 2000, 297–306, doi:10.1145/344779.344929.
48. Yang, J.C.; Everett, M.; Buehler, C.; McMillan, L. A real-time distributed light field camera. *Eurographics Work. Render.* 2002, 77–85.

49. Kubota, A.; Aizawa, K.; Chen, T. Reconstructing dense light field from array of multifocus images for novel view synthesis. *IEEE Trans. Image Process.* 2007, 16, 269–279, doi:10.1109/TIP.2006.884938.
50. Cenedese, A.; Cenedese, C.; Furia, F.; Marchetti, M.; Moroni, M.; Shindler, L. 3D particle reconstruction using light field imaging. *16th Int Symp Appl. Laser Tech. to Fluid Mech.* 2012, 9–12.
51. Liao, M.; Zhang, Q.; Wang, H.; Yang, R.; Gong, M. Modeling deformable objects from a single depth camera. *Proc. IEEE Int. Conf. Comput. Vis.* 2009, 167–174, doi:10.1109/ICCV.2009.5459161.
52. Kim, J.; Jung, J.-H.; Jeong, Y.; Hong, K.; Lee, B. Real-time integral imaging system for light field microscopy. *Opt. Express* 2014, 22, 10210, doi:10.1364/oe.22.010210.
53. Heinze, C., Spyropoulos, S., Hussmann, S. and Perwass, C., Automated robust metric calibration algorithm for multifocus plenoptic cameras. *IEEE Transactions on Instrumentation and Measurement*, 65(5), pp.1197-1205, 2016.
54. Adelson, E.H.; Wang, J.Y.A. Single lens stereo with a plenoptic camera. *IEEE Trans. Pattern Anal. Mach. Intell.* 14 no.2, 99–106, 1992.
55. Liang, C.K.; Lin, T.H.; Wong, B.Y.; Liu, C.; Chen, H.H. Programmable aperture photography: Multiplexed light field acquisition. *ACM Trans. Graph.* 2008, pp 1-10, doi:10.1145/1360612.1360654.
56. Fuchs, M.; Kächele, M.; Rusinkiewicz, S. Design and fabrication of faceted mirror arrays for light field capture. *Comput. Graph. Forum* 2013, 32, 246–257, doi:10.1111/cgf.12201.
57. Jones, A.; McDowall, I.; Yamada, H.; Bolas, M.; Debevec, P. Rendering for an interactive 360° light field display. *ACM Trans. Graph.* 2007, 26, 40, doi:10.1145/1239451.1239491.
58. Georgiev, T.; Zheng, K.C.; Curless, B.; Salesin, D.; Nayar, S.; Intwala, C. Spatio-angular resolution tradeoffs in integral photography. *Eurographics Symp. Render.* 2006, 263–272, doi:10.2312/EGWR/EGSR06/263-272.

59. Shimano, T.; Nakamura, Y.; Tajima, K.; Sao, M.; Hoshizawa, T. Lensless light-field imaging with Fresnel zone aperture: quasi-coherent coding. *Appl. Opt.* 2018, 57, 2841, doi:10.1364/ao.57.002841.
60. Papageorgiou, E.P.; Boser, B.E.; Anwar, M. An angle-selective CMOS imager with on-chip micro-collimators for blur reduction in near-field cell imaging. *Proc. IEEE Int. Conf. Micro Electro Mech. Syst.* 2016, doi:10.1109/MEMSYS.2016.7421629.
61. Varghese, V.; Chen, S. Incident light angle detection technique using polarization pixels. *Proc. IEEE Sensors* 2014, 2167–2170, doi:10.1109/ICSENS.2014.6985468.
62. Varghese, V.; Chen, S. Polarization-Based Angle Sensitive Pixels for Light Field Image Sensors With High Spatio-Angular Resolution. *IEEE Sens. J.* 2016, 16, 5183–5194, doi:10.1109/JSEN.2016.2555945.
63. Gill, P.R.; Lee, C.; Sivaramakrishnan, S.; Molnar, A. Robustness of planar Fourier capture arrays to colour changes and lost pixels. *J. Instrum.* 2012, 7 (01), doi:10.1088/1748-0221/7/01/C01061.
64. Yi, S.; Zhou, M.; Yu, Z.; Fan, P.; Behdad, N.; Lin, D.; Wang, K.X.; Fan, S.; Brongersma, M. Subwavelength angle-sensing photodetectors inspired by directional hearing in small animals. *Nat. Nanotechnol.* 2018, 13, 1143–1147, doi:10.1038/s41565-018-0278-9.
65. Okamoto, D.; Fujikata, J.; Nishi, K.; Ohashi, K. Numerical study of near-infrared photodetectors with surface-plasmon antenna for optical communication. *Jpn. J. Appl. Phys.* 2008, 47, 2921–2923, doi:10.1143/JJAP.47.2921.
66. Satoh, H.; Kawakubo, K.; Ono, A.; Inokawa, H. Material dependence of metal grating on SOI photodiode for enhanced quantum efficiency. *IEEE Photonics Technol. Lett.* 2013, 25, 1133–1136, doi:10.1109/LPT.2013.2260138.

67. Tan, C.L.; Lysak, V. V.; Alameh, K.; Lee, Y.T. Absorption enhancement of 980 nm MSM photodetector with a plasmonic grating structure. *Opt. Commun.* 2010, 283, 1763–1767, doi:10.1016/j.optcom.2009.11.044.
68. Pitarke, J.M.; Silkin, V.M.; Chulkov, E. V.; Echenique, P.M. Theory of surface plasmons and surface-plasmon polaritons. *Reports Prog. Phys.* 2007, 70, 1–87, doi:10.1088/0034-4885/70/1/R01.
69. Motogaito, A.; Ito, Y. Excitation Mechanism of Surface Plasmon Polaritons for Surface Plasmon Sensor With 1D Metal Grating Structure for High Refractive Index Medium. *Photonic Sensors* 2019, 9, 11–18, doi:10.1007/s13320-018-0515-8.
70. Ebbesen, T.W.; Lezec, H.J.; Ghaemi, H.F.; Thio, T.; Wolff, P.A. Extraordinary optical transmission through sub-wavelength hole arrays. *Nature* 1998, 391, 667–669, doi:10.1038/35570.
71. Martín-Moreno, L.; García-Vidal, F.J.; Lezec, H.J.; Pellerin, K.M.; Thio, T.; Pendry, J.B.; Ebbesen, T.W. Theory of extraordinary optical transmission through subwavelength hole arrays. *Phys. Rev. Lett.* 2001, 86, 1114–1117, doi:10.1103/PhysRevLett.86.1114.
72. Ghaemi, H.; Thio, T.; Grupp, D.; Ebbesen, T. Surface plasmons enhance optical transmission through subwavelength holes. *Phys. Rev. B - Condens. Matter Mater. Phys.* 1998, 58, 6779–6782, doi:10.1103/PhysRevB.58.6779.
73. Ishi, T.; Fujikata, J.; Marita, K.; Baba, T.; Ohashi, K. Si nano-photodiode with a surface plasmon antenna. *Japanese J. Appl. Physics, Part 2 Lett.* 2005, 44, 8–11, doi:10.1143/JJAP.44.L364.
74. Satoh, H.; Inokawa, H. Surface plasmon antenna with gold line and space grating for enhanced visible light detection by a silicon-on-insulator metal-oxide-semiconductor photodiode. *IEEE Trans. Nanotechnol.* 2012, 11, 346–351, doi:10.1109/TNANO.2011.2171194.

75. Photodiode, T.S.J.; Satoh, H.; Ono, A.; Inokawa, H. Enhanced Visible Light Sensitivity by Gold Line-and-Space Grating Gate Electrode in. 2013, 60, 812–818.
76. Satoh, H.; Kawakubo, K.; Ono, A.; Inokawa, H. Extraordinary Incident Angle Dependence of External Quantum Efficiency in SOI Photodiode with Silver Line-and-Space Grating. 2015, 3, 266–267, doi:10.7567/ssdm.2012.ps-7-261.
77. Nagarajan, A.; Hara, S.; Satoh, H.; Panchanathan, A.P.; Inokawa, H. Directivity of SOI photodiode with gold surface Plasmon antenna. 2019 Silicon Nanoelectron. Work. SNW 2019, 63, 3–4, doi:10.23919/SNW.2019.8782959.
78. H., A.; C-K., M.; P., V. CMOS Photodetectors. Photodiodes - World Act. 2011 2011, doi:10.5772/20194.
79. Koch, C.; Oehm, J.; Emde, J.; Budde, W. Light source position measurement technique applicable in SOI technology. IEEE J. Solid-State Circuits 2008, 43, 1588–1593, doi:10.1109/JSSC.2008.922402.
80. Molnar, A.; Wang, A.; Gill, P. CMOS angle sensitive pixels for 3-D imaging. Imaging Syst. Appl. ISA 2012, pp. JW4A-2, doi:10.1364/aio.2012.jw4a.2.
81. Nagarajan, A.; Hara, S.; Satoh, H.; Panchanathan, A.P.; Inokawa, H. Angular Selectivity of SOI Photodiode with Surface Plasmon Antenna. IEICE Electron. Express 2020, pp.17-20200187, doi:10.1587/elex.17.20200187.
82. Liu, J.M. Photonic devices. Photonic Devices 2005, 9780521551, 1–1052, doi:10.1017/CBO9780511614255.
83. Harris, N.; Ausman, L.K.; McMahon, J.M.; Masiello, D.J.; Schatz, G.C. Computational electrodynamic methods. RSC Theor. Comput. Chem. Ser. 2011, 147–178.